SECONDARY FLUID INJECTION
INTO A SUPERSONIC AIRSTREAM

by

EDWARD J. SZPIRO, B. Eng.

A thesis submitted to the Faculty of Graduate Studies and Research in partial fulfilment of the requirements for the degree of Master of Engineering

Department of Mechanical Engineering,
McGill University,
Montreal.

April, 1965.

SUMMARY

This report presents simplified theoretical models, based on Newtonian flow concepts, for the prediction of the injectant path, and hence the penetration distance for both gaseous (compressible) and liquid (incompressible secondary injection into a supersonic stream.

Experimentation shows that it is possible to achieve significant penetration distances (for spontaneous supersonic combustion) by injecting from a wall orifice. Experiments were performed for water injection into a Mach 3 supersonic airstream, for ranges of initial injection angle (28° upstream to 31° downstream), injector diameters (0.014 in. to 0.035 in.) and injectant total pressures (65 psia to 365 psia). The total number of different runs, from which results were obtained, was 105.

The simplicity of the theory and the accuracy with which it agrees with the experiments, would appear to favour the use of this approach for the theoretical prediction of penetration distances and paths for downstream and small angle upstream injection.

ACKNOWLEDGEMENTS

The author is grateful to his directors of research, Professor S. Molder and Professor J.M. Forde, for their discussions and advice which were of vital importance to the research. The author also wishes to express his gratitude to Mr. J.E. Kelly for his valuable assistance in the period of experimental work.

The financial support of the Defence Research Board of Canada is gratefully acknowledged.

TABLE OF CONTENTS

LIST OF SYMBOLS

a	speed of sound
A	cross-sectional area
A_{exit}	area of nozzle exit
A_t	area at throat of secondary jet (water) flow nozzle
AR	area ratio of nozzle
b	width of two-dimensional jet at wall
B	body force
C_1, C_2, C_3	constants defined in Equations 26, 27 and 28
$C_{dis.}$	discharge coefficient of water flow nozzle
C_p	pressure coefficient
$C_{p_{mod.\ Newt.}}$	modified Newtonian pressure coefficient
$C_{p_{reg.\ Newt.}}$	regular Newtonian pressure coefficient
D	diameter
F	surface pressure force
F_x	force in x-direction
g	gravitational constant = 32.2 ft/sec^2
h	jet penetration distance
K_1	constant defined by Equation (B-2) (Appendix B)
l	distance along jet centreline
m	mass flow = ρAV
M	Mach number
P	static pressure
P_b	pressure at leading edge of secondary jet
q	dynamic pressure = $\frac{1}{2} \rho V^2$
Q	volume flow

R	gas constant
R_{air}	gas constant for air
S	lateral surface area
t	time
T	temperature
V	velocity
x	co-ordinate
$\bar{x}$	non-dimensional co-ordinate (see Sect. 2.4)
y	co-ordinate
$\bar{y}$	non-dimensional co-ordinate (see Sect. 2.4)
z	parameter defined in Equation 25

Greek Symbols

γ	ratio of specific heats of gas
δ	angle of freestream flow deflection
δ_{BL}	boundary layer thickness
$\delta_{1_{BL}}$	boundary layer displacement thickness
$\delta_{2_{BL}}$	boundary layer momentum thickness
Λ	angle secondary jet axis makes with normal to freestream flow
Λ_o	initial angle secondary jet axis makes with normal to freestream flow at wall
ϕ	angle defined in Figures 3 and 7
ρ	density

Subscripts

j	secondary jet conditions
jI	initial secondary jet conditions
tj	secondary jet total conditions
exp	experimental value
max	maximum conditions
th	theoretical value
1	conditions before normal shock
2	conditions after normal shock
℄	centreline conditions
∞	freestream flow conditions
c.s.	control surface
c.v.	control volume

Superscripts

$\rightharpoonup$	vectorial notation
*	conditions at leading edge of jet (real or imaginary leading edge)

Legend for Computer Plots

AMINF	M_∞	freestream Mach number
GINF	γ_∞	ratio of specific heats for freestream flow
GJ	γ_j	ratio of specific heats for secondary jet
PTINF	$P_{t\infty}$	freestream total pressure
PJT	P_{tj}	secondary jet total pressure

RJ	R_j	gas constant for secondary jet
TJT	T_{tj}	secondary jet total temperature
XBAR	$\bar{x}$	non-dimensional co-ordinate
YBAR	$\bar{y}$	non-dimensional co-ordinate
X/DJ	x/D_j	for tube
	x/b	for sheet
Y/DJ	y/D_j	for tube
	y/b	for sheet

1. INTRODUCTION

In recent years the problem of supersonic combustion has achieved importance. One of the main motivations for research on this problem is the attractive theoretical performance of the supersonic combustion ramjet (scramjet). The mode of combustion applicable to the scramjet is the supersonic diffusion flame, which involves a fuel jet diffusing into a supersonic oxidizing stream. Much research is now being carried out on the mixing and reaction aspects of supersonic combustion. However, injection must take place prior to the occurrence of mixing and reaction.

When injecting a fluid into a supersonic flow it is often impractical to inject from a flame holder or other obstruction within the flow, since the resulting shock system causes additional flow losses. This method also introduces material problems due to the high stagnation temperature on the surface of the obstruction. On the other hand, injecting a fluid directly from a wall has the advantage of not incurring the above penalties.

Preliminary investigations (Ref. 1,2) indicate that the mode of injection has an influence on supersonic mixing and combustion. Theoretical calculations (Ref. 3) have shown that best hypersonic ramjet engine performance is obtained by downstream fuel injection. On the other hand, experimental evidence (Ref. 4) shows that fuel mixing is enhanced by cross-stream injection.

An extensive literature survey was made in order to determine what information is available in the field of secondary fluid injection. Comparatively little information is available on secondary injection into supersonic streams (Ref. 5), while considerable work, both experimental and theoretical, has been done on injection into a subsonic flow (Ref. 6,7,8).

Few theories (Ref. 5) exist for the prediction of the pressure distribution along the wall or for the shape of the injectant path, for the case of secondary injection into a supersonic stream. Most of the experimental work on secondary injection into a supersonic stream had as its main purpose the obtaining of a side impulse for thrust vector control (Ref. 9 to 14), and not fuel injection for supersonic combustion. Consequently, these researchers (with the exception of Ref. 5) were interested primarily in the wall pressure distribution, and paid little attention to the injectant path or the penetration distance.

Ferrari (Ref. 5) made an analysis of the interference forces and side forces exerted upon a cylindrical body by a gaseous jet issuing laterally from a circular orifice into a hypersonic flow. This work included the development of a general conceptual model to determine the manner in which the side-jet penetrated the enveloping stream, and also the determination of the shape of the curve marking the central axis of the jet.

References 10 to 12 contain an investigation of the surface pressure distribution caused by secondary injection from a flat plate into a supersonic flow. Attas (Ref. 13) investigated the interaction effects caused by injecting water into the boundary layer of a supersonic stream, while McRee et al (Ref. 14) investigated the effect on the turbulent skin friction of secondary air injection into a Mach 3 airstream. Zukoski and Spaid (Ref. 15) studied the flow field around the injection port for secondary injection of a gas normal to a supersonic stream. They calculated a scale parameter for the prediction of the side forces generated by secondary injection, and also obtained a simplified relation for the penetration distance of the injectant. Dowdy and Newton (Ref. 16) investigated the interaction effects produced when liquid or gaseous nitrogen is injected from a flat plate normal to a supersonic stream.

For compressible (or even incompressible) secondary flow into a primary supersonic flow, the field is very much an open one. Hence a study was undertaken to investigate the problem of fluid injection into a supersonic stream, with special emphasis on the jet flow far from the injection orifice.

The present investigation has a two-fold purpose:

1) To develop a theoretical model which would predict the behaviour of liquid and gaseous jets injected at various angles to high temperature supersonic airflows.

2) To obtain experimental observations of liquid (water) injection into a supersonic airstream.

The present report deals with the effects occurring when a liquid (water) is injected (at various angles) into a supersonic airstream. The effects of freestream and injectant total pressure are examined. In view of the main objective of the overall investigation, i.e. the study of supersonic combustion, the experimental arrangement was such as to approximate the combustion chamber entry of a scramjet.

2. THEORETICAL CONSIDERATIONS

Secondary injection may be defined as the transfer of momentum between one finite stream of fluid and an infinite stream of another fluid. Momentum transfer between the two streams is brought about by both the pressure forces and the viscous shear forces acting on the injectant. This differs from the subsequent mixing, where the mass transfer is caused by diffusion.

A qualitative explanation of the phenomena associated with fluid injection can be given as follows: a jet of fluid, entering at a angle into the main flow is curved, due to the centripetal force caused by the pressure difference between the leading edge and the rear of the jet. The leading edge pressure is increased by the retarding effect of the jet on the primary flow, while the rarefaction which occurs at the rear causes a decrease in pressure.

Secondary injection from a flat plate into a supersonic stream results in a complex flow structure (Fig. 1). The boundary layer on the flat plate may be either laminar or turbulent, resulting in different degrees of separation and a separation shock which attaches itself to the bow shock in front of the jet. For the single circular injectant port, the bow shock forms a shock envelope that partially surrounds the jet. A two-dimensional injectant sheet induces a much larger separation region than injection from a single circular port. In reality, the jet will start to diffuse almost immediately upon entering the freestream flow. The most general case is a very complex flow, determined by mixed subsonic, transonic and supersonic flows and their interactions with transport phenomena.

Abramovich (Ref. 8) discusses the work of Shandorov (Ref. 17), who investigated secondary subsonic injection. Acknowledging the existence of a similarity between injection into a subsonic or into a supersonic freestream flow, a description of the supersonic case, which is a slight modification of the subsonic case, is presented. This modification allows primarily for the existence of a bow shock in front of the jet.

Figure 2a shows what is thought to be the velocity and pressure fields in the plane of symmetry of a jet deflected by a supersonic lateral flow. A rapid change in the total pressure across the jet is noticeable, with this effect decreasing at the edges of the jet. As in the subsonic case, the line of maximum total pressures is located closer to the forward edge of the jet than the line of maximum velocity, which may be explained by the character of the static pressure variation in the cross-section of a curved jet.

Figure 2b shows what is thought to be the cross-section of the jet at various distances from the first section. It can be seen that as the jet (axisymmetric in the first section) moves away from the port, it will acquire the shape of a horseshoe. This deformation of the jet's section is due to the pressure field surrounding the jet and may be partially explained by the character of the interaction of the jet with the flow. Due to the intensive intermixing of the jet emerging from the port, with the freestream flow, a turbulent layer develops at once. The peripheral particles of the jet have less velocity than the particles of the core, and hence are more forcefully bent by the freestream flow away from the initial direction. Thus the peripheral particles are moved along more curved trajectories, which leads to the development of the horseshoe shape.

In the intermediate and later stages of the jet, the forward edge of the horseshoe may be approximated by a two-dimensional jet. Hence an analysis is made of both the two-dimensional sheet and the three-dimensional circular cross-section jet.

2.1 Mathematical Models

Fluid injection is mathematically very complex. It is basically an interaction of inertia and viscous effects. The fluid injection path is dependent primarily on the pressure and viscous shear forces and secondarily on the heat and mass transfer.

In attempting to provide a simplified theoretical basis for the observed secondary fluid injection path, two basic mathematical models have been postulated -- one for gaseous and the other for liquid injection.

The first model deals with the case where the secondary injectant is a compressible fluid (i.e. a gaseous fluid). This case is analysed for both two-dimensional and circular cross sections of the secondary injectant, using the regular Newtonian pressure coefficient.

The second model deals with an incompressible secondary injectant (i.e. a liquid). This case is analysed for both two-dimensional and circular secondary injectant cross sections, using both the regular Newtonian and the modified Newtonian pressure coefficients.

2.2 General Assumptions

In order to develop a theoretical explanation for the path followed by a secondary fluid when injected into a supersonic stream, some of the assumptions made in the following analysis are restrictive but necessary in order to develop simplified models. The most important ones are, therefore, listed and discussed below.

1. Isentropic flow exists within the secondary jet.
2. A specific pressure coefficient, such as the regular Newtonian or modified Newtonian, may be used to calculate the pressure force on the secondary jet.
3. The shock in front of the secondary jet is the same shape as the jet. This assumption restricts the validity of the injectant path to the region where the injectant axis does

not deviate excessively from the normal to the freestream direction. It should be noted that this assumption is inherent in the postulated existence of Newtonian flow.

4. a) For an incompressible secondary jet, both the cross-sectional size and shape of the jet do not change.
   b) For a compressible secondary jet, the cross-sectional size changes (isentropically), while retaining the same shape.

5. All secondary jet flow properties are uniform across any cross-section and may vary only along the secondary jet axis. For the compressible case, the secondary jet static pressure is taken as the mean of the freestream static pressure (i.e. at rear of jet) and the total pressure after the shock (i.e. in front of jet).

6. The ratio of specific heats of the secondary jet (for gaseous injection) is constant. This is reasonable where the cooling or heating effect is not large. (See assumption 8a.)

7. The secondary jet is sonic at the point of injection (i.e. $M_{JI} = 1$) for the compressible (gaseous) jet.

8. The effects of the following transport phenomena are neglected:
   a) heat transfer from freestream to secondary jet, or vice versa;
   b) diffusion or mixing;

c) viscous shear forces on the surface of the secondary jet. This assumption is restrictive, being valid only in the region where the injectant axis does not deviate excessively from the normal to the freestream direction;

d) viscous shear effects in the wall boundary layer. This is valid if it is considered that injection commences at a "corrected" distance from the wall (such as the boundary layer, momentum or displacement thickness).

9. No chemical reactions occur between the secondary jet and the freestream flow.

2.3 Compressible Injectant Flow

The general momentum equation for a control volume may be written as follows:

$$\vec{F} + \iiint_{c.v.} \vec{B}\, d(\text{Mass}) = \iint_{c.s.} \vec{V}\, (\rho\, \vec{V} \cdot d\, \vec{A}) + \frac{\partial}{\partial t} \iiint_{c.v.} \vec{V}\, d(\text{Mass}) \ldots (1)$$

For no body forces ($\vec{B} = 0$), Equation 1 can be reduced (with the aid of the Gauss theorem) to:

$$d\, \vec{F} = \frac{D}{Dt}\, (\text{Mass} \cdot \vec{V}) \qquad \ldots\ldots\ldots\ldots\ldots (2)$$

The mathematical models for both a single circular port and a two-dimensional port are illustrated in Figures 3 and 4 respectively. For both cases Lagrangian co-ordinates are chosen with the assumption that all properties within the element are uniform throughout the element (Assumption 5).

Considering Equation 2 along the x-direction results in the following equations:

General: $$dF_x = \frac{d}{dt}\,(\text{Mass } V_x) \qquad \ldots\ldots\ldots\ldots(3)$$

For single circular port:

$$2\int_{\phi=0}^{\phi=\pi/2} C_p\, q_\infty \cos\Lambda \cos\phi\, dS = \frac{d}{dt}\,(\rho_j\, A_j\, dl\, V_j \sin\Lambda) \quad \ldots(4)$$

For two-dimensional sheet:

$$C_p\, q_\infty\, dS \cos\Lambda = \frac{d}{dt}\,(\rho_j\, A_j\, dl\, V_j \sin\Lambda) \qquad \ldots\ldots\ldots(5)$$

For a regular Newtonian pressure coefficient:

$$C_p = C_{p_{\text{reg.Newt.}}} = 2\sin^2\delta \qquad \ldots\ldots\ldots\ldots(6)$$

Assumption 5 gives a plausible relationship for the jet elemental pressure.

$$P_j = \frac{P_b + P_\infty}{2} \qquad \ldots\ldots\ldots\ldots(7)$$

From Figures 3 and 4, the following geometrical relationships are evident:

General: $$dx = dl\,\sin\Lambda \qquad \ldots\ldots\ldots\ldots(8)$$

$$dy = dl\,\cos\Lambda \qquad \ldots\ldots\ldots\ldots(9)$$

For single circular port:

$$dS = \frac{D_j}{2}\,dl\,d\phi \qquad \ldots\ldots\ldots\ldots(10)$$

$$\sin\delta = \cos\Lambda\,\cos\phi \qquad \ldots\ldots\ldots\ldots(11)$$

$$A_j = \pi/4\; D_j^2 \qquad \ldots\ldots\ldots\ldots(12)$$

For two-dimensional sheet:

$$dS = dl \text{ (assuming unit width)} \quad \ldots\ldots(13)$$

$$\sin\delta = \cos\Lambda \qquad \ldots\ldots\ldots\ldots(14)$$

The following isentropic and general flow relationships (Ref. 18,19) are also required:

Mach number $M_j = V_j/a_j$ ....(15)

Speed of sound $a_j = \sqrt{\gamma_j R_j T_j g}$ ....(16)

Pressure coefficient $C_p = \dfrac{P_b - P_\infty}{q_\infty}$ ....(17)

Ideal gas equation $P = \rho R T$ ....(18)

Static temperature (Adiabatic) $T_j = T_{tj} \left(1 + \dfrac{\gamma_j - 1}{2} M_j^2\right)^{-1}$ ....(19)

Static pressure (Isentropic) $P_j = P_{tj} \left(1 + \dfrac{\gamma_j - 1}{2} M_j^2\right)^{-\frac{\gamma_j}{\gamma_j - 1}}$ .....(20)

Static density (Isentropic) $\rho_j = \rho_{tj} \left(1 + \dfrac{\gamma_j - 1}{2} M_j^2\right)^{-\frac{1}{\gamma_j - 1}}$ .....(21)

Area ratio of stream tube (Isentropic)

$$\frac{A_j}{A_{jI}} = \frac{1}{M_j}\left[\frac{2}{\gamma_j + 1} + \frac{\gamma_j - 1}{\gamma_j + 1} M_j^2\right]^{\frac{\gamma_j + 1}{2(\gamma_j - 1)}} \quad \text{.........(22)}$$

Combining Equations 6 - 9 and 15 - 22 along with the appropriate single circular port equations (Eq. 4,10-12) or the appropriate two-dimensional case equations (Eq. 5,13,14) yields the following relationships for the jet injectant path:

For single circular port (See Appendix A1 for derivation):

$$\frac{dl}{D_{jI}} = \frac{1 + C_1 z^{-\frac{1}{\gamma_j}} \left(1 - z^{\frac{\gamma_j - 1}{\gamma_j}}\right) \sin^2\Lambda}{C_3 \cos^2\Lambda \quad z^{-\frac{\gamma_j - 1}{\gamma_j}}} \, d\Lambda \quad \text{.......(23)}$$

For two-dimensional sheet (See Appendix A2 for derivation):

$$\frac{dl}{b} = \frac{\left(1 - z^{\frac{\gamma_j - 1}{\gamma_j}}\right)^{\frac{1}{2}} + C_1 z^{-\frac{1}{\gamma_j}} \left(1 - z^{\frac{\gamma_j - 1}{\gamma_j}}\right)^{-\frac{1}{2}} \sin^2\Lambda}{C_2 \cos^2\Lambda} \, d\Lambda \quad \text{...(24)}$$

Equations 23 and 24 define the length (from the injection port) of the jet centreline in terms of the angle the jet centreline makes with the normal to the freestream flow.

The following equations are applicable to both the circular single port and the two-dimensional sheet:

$$z = z(\Lambda) = \frac{q_{\infty}}{P_{tj}} \cos^2\Lambda + \frac{P_{\infty}}{P_{tj}} \qquad \text{.........(25)}$$

$$C_{\Upsilon} = \left(\frac{\gamma_j - 1}{\gamma_j}\right)^{1/2} \frac{q_{\infty}}{P_{tj}} \qquad \text{.........(26)}$$

$$C_2 = \left(\frac{\gamma_j - 1}{\gamma_j}\right)^{\frac{1}{2}} \frac{2\, q_{\infty}\, g}{(m_j/A_{jI})\,(\gamma_j\, R_j\, T_{tj}\, g)^{1/2}} \qquad \text{.........(27)}$$

$$C_3 = \frac{8}{3\pi} \cdot \left(\frac{\gamma_j - 1}{2}\right)^{\frac{1}{4}} \cdot \left(\frac{\gamma_j + 1}{2}\right)^{\frac{\gamma_j + 1}{4(\gamma_j - 1)}} \cdot C_2 \qquad \text{.......(28)}$$

where (as derived in Appendix A3),

$$\frac{m_j}{A_{jI}} = \left(\frac{\gamma_j\, g}{R_j}\right)^{1/2} \left(\frac{2}{\gamma_j + 1}\right)^{\frac{\gamma_j + 1}{2(\gamma_j - 1)}} \frac{P_{tj}}{\sqrt{T_{tj}}} \qquad \text{.......(29)}$$

For the freestream flow, the following relationships exist:

$$q_{\infty} = \frac{\gamma_{\infty}}{2} P_{\infty} M_{\infty}^2 \qquad \text{......... (30)}$$

$$P_{\infty} = P_{t\infty} \left(1 + \frac{\gamma_{\infty} - 1}{2} M_{\infty}^2\right)^{-\frac{\gamma_{\infty}}{\gamma_{\infty} - 1}} \qquad \text{....(31)}$$

Substituting Equations 8 and 9 into Equation 23 or 24 will, upon numerical integration, give the x and y co-ordinates of the centreline of the injectant path. Careful examination of the equations show that the centreline path can be completely defined by the following parameters:

Geometry	Jet	Primary Flow
Λ_o	γ_j	γ_∞
b or D_{jI}	R_j	$P_{t\infty}$
	P_{tj}	M_∞
	T_{tj}	

A digital computer program has been written for the solution to both the single circular port and two-dimensional cases. Figures 5 and 6 are computer plots of samples of the above cases for normal injection. These plots also include the isentropic injectant expansion, as calculated from Equation 22.

Zukoski and Spaid (Ref. 15) obtained the following simplified theoretical relation for the penetration distance of a gaseous secondary jet, when injected normally into a supersonic primary flow:

$$\frac{h}{D_{jI}C_{dis}^{1/2}} = \frac{1}{M_\infty}\left[\frac{P_{tj}}{P_\infty}\,\frac{\gamma_j}{\gamma_\infty}\,\frac{2}{C_{p*}}\right]^{1/2}\left\{\left(\frac{2}{\gamma_j-1}\right)\left(\frac{2}{\gamma_j+1}\right)^{\frac{\gamma_j+1}{\gamma_j-1}}\left[1-\left(\frac{P_\infty}{P_{tj}}\right)^{\frac{\gamma_j-1}{\gamma_j}}\right]\right\}^{\frac{1}{4}} \quad \ldots(32)$$

The penetration distance obtained by Equation 32 is considerably less than that obtained using the equations developed in this report (Figure 5). This may be partially accounted for by the fact that the authors of Ref. 15 used the assumption that:

> "…. the interface between the injectant and primary flows is a quarter sphere followed by an axisymmetric half body,..."

Comparing Figures 5 and 6, it is seen that the expansion of the jet cross-sectional area is much greater for the two-dimensional case than for the single circular port case. The reason for this lies in the fact that for the two-dimensional case the isentropic area change is assumed to occur in only one dimension, while for the single circular port case the area expansion occurs uniformly in all directions of the cross-sectional area.

Calculating and plotting a large number of different situations leads to the conclusion (for both cases) that (P_{t_j}/P_{t_∞}) and not P_{t_j} is the dominant parameter. As expected, it can also be concluded that the penetration into the freestream increases with an increase in (P_{t_j}/P_{t_∞}).

2.4 Incompressible Injectant Flow

The mathematical models for the incompressible jet tube and the incompressible jet sheet are illustrated in Figures 7 and 8 respectively. For both cases Lagrangian coordinates are chosen. Since the injectant flow is both incompressible and of constant cross-section, it can easily be deduced that all flow properties throughout the jet are constant and uniform.

The compressible momentum equations (Eq. 4 and 5) also hold true for the incompressible jet tube and sheet respectively.

Jet tube:

$$2\int_{\phi=0}^{\phi=\frac{\pi}{2}} C_p\, q_\infty \cos\Lambda \cos\phi\, dS = \frac{d}{dt}\left(\rho_j A_j dl\, V_j \sin\Lambda\right) \quad ..(4)$$

Jet sheet:

$$C_p\, q_\infty \cos\Lambda\, dS = \frac{d}{dt}\left(\rho_j\, A_j\, dl\, V_j \sin\Lambda\right) \quad ......(5)$$

For the incompressible injectant flow, both the regular (Eq. 6) and the modified Newtonian pressure coefficients are used.

$$C_{p_{\text{reg. Newt.}}} = 2\sin^2\delta \quad ....(6)$$

$$C_{p_{\text{mod. Newt.}}} = \left(\frac{C_{p*}}{\sin^2\delta*}\right)\sin^2\delta \quad ......(33)$$

The equations describing the geometrical relationships for the incompressible model are identical to those obtained for the compressible model.

General: $dx = dl \sin\Lambda$ .....(8)

$dy = dl \cos\Lambda$ .....(9)

Jet tube: $dS = \frac{D_j}{2}\, dl\, d\phi$ .....(10)

$\sin\delta = \cos\Lambda \cos\phi$ .....(11)

$A_j = \pi/4 \cdot D_j^2$ .....(12)

Jet sheet: $dS = dl$ (assuming unit width) ....(13)

$A_j = b$ " " "

$\sin\delta = \cos\Lambda$ ....(14)

Combining each of the momentum equations (Eq. 4 or 5) along with its appropriate geometrical relationship and with each of the two pressure coefficients (Eq. 6 or 33) will yield the following relationships (which are derived in Appendix B) in terms of non-dimensional co-ordinates $\bar{x}$ and $\bar{y}$.

Jet Tube -- Regular Newtonian C_p (Appendix B1):

$$\bar{x} = \frac{x}{(D_j/2)}\,\frac{q_\infty}{q_j} = \frac{3}{4}\,\pi\left[\frac{1}{\cos\Lambda} - \frac{1}{\cos\Lambda_o}\right] \quad \ldots\ldots(34)$$

$$\bar{y} = \frac{y}{(D_j/2)}\,\frac{q_\infty}{q_j} = \frac{3}{8}\,\pi\,\ln\left[\frac{1+\sin\Lambda}{1-\sin\Lambda}\cdot\frac{1-\sin\Lambda_o}{1+\sin\Lambda_o}\right] \quad \ldots\ldots(35)$$

Jet Sheet -- Regular Newtonian C_p (Appendix B2):

$$\bar{x} = \frac{x}{(b/2)}\,\frac{q_\infty}{q_j} = 2\left[\frac{1}{\cos\Lambda} - \frac{1}{\cos\Lambda_o}\right] \quad \ldots\ldots(36)$$

$$\bar{y} = \frac{y}{(b/2)}\,\frac{q_\infty}{q_j} = \ln\left[\frac{1+\sin\Lambda}{1-\sin\Lambda}\;\frac{1-\sin\Lambda_o}{1+\sin\Lambda_o}\right] \quad \ldots\ldots(37)$$

Jet Tube -- Modified Newtonian C_p (Appendix B1):

$$\bar{x} = \frac{x}{(D_j/2)}\,\frac{q_\infty}{q_j} = \left(\frac{2}{C_{p*}/\sin^2\delta^*}\right)\frac{3\pi}{4}\left[\frac{1}{\cos\Lambda} - \frac{1}{\cos\Lambda_o}\right] \quad \ldots\ldots(38)$$

$$\bar{y} = \frac{y}{(D_j/2)}\,\frac{q_\infty}{q_j} = \left(\frac{2}{C_{p*}/\sin^2\delta^*}\right)\frac{3\pi}{8}\,\ln\left[\frac{1+\sin\Lambda}{1-\sin\Lambda}\;\frac{1-\sin\Lambda_o}{1+\sin\Lambda_o}\right] \quad \ldots\ldots(39)$$

Jet Sheet -- Modified Newtonian C_p (Appendix B2):

$$\bar{x} = \frac{x}{(b/2)}\,\frac{q_\infty}{q_j} = \left(\frac{2}{C_{p*}/\sin^2\delta^*}\right) 2\left[\frac{1}{\cos\Lambda} - \frac{1}{\cos\Lambda_o}\right] \quad \ldots\ldots(40)$$

$$\bar{y} = \frac{y}{(b/2)}\,\frac{q_\infty}{q_j} = \left(\frac{2}{C_{p*}/\sin^2\delta^*}\right)\ln\left[\frac{1+\sin\Lambda}{1-\sin\Lambda}\;\frac{1-\sin\Lambda_o}{1+\sin\Lambda_o}\right] \quad \ldots\ldots(41)$$

where (Ref. 19),

$$\frac{C_{p*}}{\sin^2\delta^*} = \frac{2}{\gamma_\infty M_\infty^2}\left[\left(\frac{\gamma_\infty+1}{2\gamma_\infty M_\infty^2-(\gamma_\infty-1)}\right)^{\frac{1}{\gamma_\infty-1}}\left(\frac{(\gamma_\infty+1)M_\infty^2}{2}\right)^{\frac{\gamma_\infty}{\gamma_\infty-1}} -1\right] \ldots(42)$$

Examination of the preceding equations shows that for all four cases the centreline path differs only by a constant factor in the $\bar{x}$ and $\bar{y}$ co-ordinates. For the cases employing the modified Newtonian pressure coefficient this factor is a function of the freestream Mach number and the ratio of specific heats. Thus the $\bar{x}$ and $\bar{y}$ co-ordinates are dependent only on the constant factor and on the initial angle of injection.

A digital computer program has been written for the solution of the four different cases. Figures 9 to 12 are computer plots of the secondary injectant centreline for various initial injection angles. Figure 13 shows computer plots comparing the four different cases (jet tube and sheet - for both the regular and the modified Newtonian pressure coefficients) for upstream, normal and downstream injection.

Ferrari (Ref.5) made a general analysis, based on an affinely similar jet, whose cross-sectional shape remains indeterminate. In the case of the circular jet considerable simplification can be achieved by considering the angle Λ as the parametric variable that determines the shape of the jet, instead of the jet axis co-ordinates as has been done by Ferrari. Ferrari's Equation (25) shows some similarity to Equation 38 and 39 of this report. By modifying the values (in Ferrari's notation) of C_f', C_f'' and $\mathcal{A}_2$, as defined in Reference 5, it is possible to obtain relations of the same form as the ones obtained in the present report.

3. EXPERIMENTAL INVESTIGATION

The experimental investigation was designed to check the liquid (water) injectant path as predicted by the incompressible mathematical models (Sect. 2.4).

3.1 Apparatus

3.1.1 Wind Tunnel

Experiments were conducted in the McGill hypersonic hot tunnel, HT-1 (Fig. 14,15,16), details of which can be found in Ref. 20. This unit is designed for operation at the following maximum conditions:

Total pressure	130 psia
Total temperature (air)	2000°K
with H_2-O_2 superheater	3000°K
Pressure ratio	500 : 1
Mass flow (air)	0.15 lb/sec.

3.1.2 Nozzle

To produce the supersonic flow, the following axi-symmetric stainless steel nozzle (Fig. 17) designed by the method of Ref. 21 (Fig. 18) was used:

Exit Mach number (nominal)	3.0
Exit diameter	1.078 in.
Throat diameter	0.480 in.

To calculate the theoretical exit conditions of the nozzle used to produce the supersonic air flow, the following conditions must be known:

1) Nozzle geometry -- area ratio (AR)
-- exit area (A_{exit})
2) Air properties -- gas constant (R_{air})
-- ratio of specific heats (γ)
3) Conditions at nozzle entrance
-- total pressure (P_t)
-- total temperature (T_t)

Using an iterative procedure on a digital computer, the Mach number (M) is calculated from the Fliegner area ratio equation (Ref. 18),

$$AR = \frac{1}{M}\left[\frac{2}{\gamma+1} + \frac{\gamma-1}{\gamma+1} M^2\right]^{\frac{\gamma+1}{2(\gamma-1)}} \qquad \text{......} \; (43)$$

The static pressure (P), the temperature (T) and the density (ρ) are calculated from the isentropic equations:

$$\frac{T_t}{T} = 1 + \frac{\gamma-1}{2} M^2 \qquad \text{........} \; (44)$$

$$\frac{P_t}{P} = \left(1 + \frac{\gamma-1}{2} M^2\right)^{\frac{\gamma}{\gamma-1}} \qquad \text{........} \; (45)$$

$$\frac{\rho_t}{\rho} = \left(1 + \frac{\gamma-1}{2} M^2\right)^{\frac{1}{\gamma-1}} \qquad \text{........} \; (46)$$

It should be noted that the total density is obtained using the ideal gas law,

$$P = \rho R_{air} T \qquad \text{.........} (47)$$

The speed of sound (a) and the freestream (air) velocity (V) are calculated from:

$$a = \sqrt{\gamma R_{air} T \, g} \qquad \text{...........(48)}$$

$$V = a \, M \qquad \text{...........(49)}$$

The mass flow (m) is given by

$$m = \rho \, A_{exit} \, V \qquad \text{...........(50)}$$

The above calculations are checked experimentally by measuring the pitot total pressure with a traversing pitot probe. This assumes a normal shock in front of the probe, and necessitates knowing only the value of the ratio of specific heats (γ) for air. Using the Rayleigh Pitot Formula (Ref. 19),

$$\frac{P_{t2}}{P_1} = \left[\frac{(\gamma+1)M_1^2}{2}\right]^{\frac{\gamma}{\gamma-1}} \left[\frac{\gamma+1}{2\gamma M_1^2 - (\gamma-1)}\right]^{\frac{1}{\gamma-1}} \qquad \text{...(51)}$$

and the Isentropic Pressure Formula,

$$\frac{P_{t1}}{P_1} = \left(1 + \frac{\gamma-1}{2} M_1^2\right)^{\frac{\gamma}{\gamma-1}} \qquad \text{..............(52)}$$

a digital computer program was set up to calculate the Mach number (M) and the static pressure (P_1).

Figure 19 shows a sample nozzle calibration for the Mach 3 nozzle. The theoretical and experimental results correlate quite well.

3.1.3 Test Section and Injectors

For secondary injection studies, two 1/4" stainless steel tubes fitted with injectors were held in place at the sides of the Mach 3 nozzle by a set of clamps. Thus the angle of injection could easily be changed. The injectors (Fig. 20) are machine screws that have been drilled the appropriate size and formed into standard flow nozzles. The stainless steel tubes were tapped so that the injectors could be screwed onto the tubes. The experimentation was facilitated by using two injectors, whose installation is shown in Figures 20 and 21.

3.1.4 Water Mass Flow Calculation

Reference 22 gives the volume flow (Q) in a flow nozzle as:

$$Q = A_t \, C_{dis.} \sqrt{\frac{2g}{\rho} \Delta P} \quad \ldots\ldots\ldots\ldots\ldots(53)$$

Equation 53 can be written for the mass flow (m) as follows:

$$m = Q\rho = A_t \, C_{dis.} \sqrt{2g\rho\Delta P} \quad \ldots\ldots\ldots\ldots\ldots(54)$$

Now, $C_{dis.}$ =discharge coefficient
=1.0 for a perfect nozzle

ΔP =pressure difference across flow nozzle
$= P_{tj} - P_{test\ section} \doteq P_{tj}$

A_t = throat area $= \frac{\pi}{4} D_{jI}^2$

ρ = water density = 62.4 lb./ft.^{3}

Assuming the flow nozzle is perfect, and making the above substitutions for A_t, ΔP and ρ along with the appropriate conversion factors for units:

$$\underset{\text{lb/sec}}{m} = 8.299 \times \underset{\text{in}^2}{D_{jI}^2} \times \underset{(\text{psi})^{1/2}}{\sqrt{P_{tj}}} \quad \ldots\ldots\ldots\ldots\ldots(55)$$

Figure 22 shows the calculated mass flows for the various water flow nozzle sizes and for the pressure range used.

To ensure continuous flow of the injected water, the following set-up (Fig. 23) was used. A cylinder of compressed nitrogen pressurized a large tank of water, which was connected to the injector through a manifold and appropriate valves. This permitted proper pressure control.

3.1.5 Instrumentation

The instrumentation of the McGill hypersonic hot tunnel is fully discussed in Ref. 20.

A Honeywell Brown Heiland Direct Recording Visicorder was used to record pressures. Pressures were measured by Statham strain gauge pressure transducers connected to the Visicorder through calibrated bridge circuits (Fig. 16). A traversing pitot pressure probe with a position indicator was used to calibrate the Mach 3 nozzle (Fig. 19). Static pressure probes were used to measure the test section pressures and the nozzle exit pressure.

A 35 mm "Robot" camera, that could take up to 12 pictures without rewinding, was installed behind one of the windows of the hot tunnel test section. Indirect lighting was obtained from the facing window by placing a flood light behind a ground glass screen.

3.2 Experimental Procedure

In all experiments, two injectors were installed, one at each side of the Mach 3 nozzle. The injectors were operated alternately. The basic procedure followed for all the experiments was:

1. Two different injectors were clamped at required angles to the air flow.
2. The zirconia pebble bed of the tunnel was preheated until equilibrium was obtained at the required rating of the pebble bed.
3. The vacuum system was turned on.
4. The test section exhaust was opened, while simultaneously turning on the high pressure air.
5. The H_2-O_2 superheater was turned on.
6. A traverse was made with the pitot pressure probe which was recorded by the Visicorder.
7. Water injection was performed separately for each of the injectors for a series of pressures. A photograph was taken for each injection at each pressure.
8. After each such series of tests, the system was open to atmosphere and a Visicorder calibration was made.

3.3 Range of Investigation

The investigation was limited to secondary water injection from a single injector, into an unbounded axisymmetric airstream. These tests were performed without a duct so as to permit visual observations.

The air total pressure was 62 psia and the air total temperature was of the order of 2600 - 3000°K for all the tests. The ranges of injector diameter, injector total pressure and angle of injection are shown in Table 1. The water was injected at room temperature (i.e. approximately 75°F).

D_{jI} / P_{tj}	0.014"	0.018"	0.025"	0.030"	0.035"
65 psia	Λ_o = 0° +14° +25°	-28° - 5°	-25° 0° +20° +31°	-25° 0° +13° +28°	——
90 psia	0° +14° +25°	-28° - 5°	-25° -13° 0° +20° +31°	-25° -13° 0° +13° +28°	——
115 psia	-25° 0° +14° +25°	-28° - 3°	-25° -13° 0° +20° +31°	-25° -13° +13° +28°	0°
165 psia	-25° +14° +28°	-28° - 5°	-25° -13° 0° +20° +31°	-25° -13° 0° +13° +28°	0°
215 psia	-25° +14° +25°	-28° - 5°	-25° -13° 0° +20° +31°	-25° -13° 0° +13° +28°	0°
265 psia (*270 psia)	-25° +14° +25°	-28° - 5°	-25° -13° +20° +31°	-25° -13° 0°* +13° +28°	0°
315 psia	-25° +14° +25°	-28° - 5°	-25° +20° +31°	-25° -13° +13° +28°	0°
365 psia	-25°	——	——	——	——

TABLE 1   RANGE OF EXPERIMENTAL INVESTIGATION
Injection Angles for Various Injectant Total Pressures and Injector Diameters

4. DISCUSSION

4.1 Visual Observations

In all the tests, the injectant was clearly visible. Some expansion was observed in the latter part of the water jet. It is uncertain whether the jet expansion is due to the break-up of the jet and droplet mixing, or to the formation of steam on the external surface of the jet. The latter case would seem more probable, in view of the high temperature of the primary airstream.

A slight backward bend in the overall jet shape was observed visually during some tests and is confirmed by the photographs. This bend is quite likely caused by a weak stable shock system existing in the primary airstream. This shock system may be due to a slight underexpansion of the air flow from the supersonic nozzle, which results from an increase in the test section pressure following the large water mass addition from some of the injectors (Fig. 22).

Sample photographs of water injection are shown in Figures 24 to 26. These figures are arranged so as to provide a correlation between the injectant shape, centreline path and penetration and the three variable parameters, namely P_{tj}, Λ_o and D_{jI}.

4.2 Experimental Results

Figure 27 shows three plots (for upstream, normal and downstream injection) of the maximum injectant (water) penetration, h_{max}, versus the injectant total pressure for a range of injection nozzle diameters. The maximum penetration is taken as the largest distance the water jet reaches from the inside of the air nozzle, less the theoretical boundary layer thickness (Ref. 24).

Figure 28 consists of two plots of the maximum penetration versus the injectant total pressure for a range of initial angles of injection. Both Figures 27 and 28 clearly show that the maximum water penetration increases rapidly with an increase in the injectant total pressure. The general trend of Figure 27 indicates that greater maximum penetration is obtained with larger injector diameters. Figure 28 shows that the greatest penetration is obtained from upstream injection, while normal injection results in slightly less penetration, on the average, than downstream injection.

Figure 29 is a graph of the relative penetration (with respect to the injector diameter), h_{max}/D_{jI}, versus the injectant total pressure. The solid lines are an attempt to define a corridor which would provide a direct relationship between the relative penetration and the injectant total pressure for a particular initial angle of injection. It can be observed that the corridor is reasonably narrow and approximately linear. One explanation for the amount of scatter, other than experimental error, is that the viscous effects vary for the different injector orifice sizes.

Figures 30, 31 and 32 are plots of the centreline path for secondary water injection. The centreline paths were obtained by projecting the negatives and taking the mean line of the brightest part of the injectant as the required paths. Samples of this centreline path were compared with the path obtained with the aid of a microphotometer, resulting in good agreement. In all cases it is clearly seen that higher injectant total pressures lead to larger injection penetration distances.

4.3 Comparison of Experiments with Theoretical Model

Figure 13 shows a comparison of the four cases for the incompressible model. It is clear that the case for the jet tube using the regular Newtonian pressure coefficient is a good average of the four different cases, which are all reasonably similar to one another. In view of this, the experimental results will be compared with the theoretical results of the jet tube using the regular Newtonian pressure coefficient.

Figure 33 shows plots of the maximum experimental penetration distance, $h_{max_{exp}}$, versus the maximum theoretical penetration distance, $h_{max_{th}}$. The latter is taken as the y co-ordinate at the outside edge of the jet tube, where the non-dimensional x co-ordinate, $\overline{x}$, equals the value of 10 (Fig. 13). This arbitrary choice is a good one, since the theoretical jet tube has almost turned to the freestream direction. It is seen that in practically all the cases shown in Figure 33, the experimental values are greater than the theoretical values for the penetration distance. Decreasing the maximum experimental penetration distance, in all cases, by approximately 0.08 in. would result in a reasonably good comparison between $h_{max_{exp}}$ and $h_{max_{th}}$.

From Figures 24 to 26 it can be seen that the water jet expands as it penetrates the freestream. This expansion may be due to vaporization and/or mixing of the water. Since this expansion is not taken into account in the theoretical calculations, it would be expected that $h_{max_{exp}}$ be larger than $h_{max_{th}}$.

Figure 34 shows plots of the centreline experimental penetration distance, $h_{℄_{exp}}$ (obtained from Fig. 30 to 32), versus the centreline theoretical penetration distance, $h_{℄_{th}}$, which is taken at $\overline{x} = 10$.*This graph illustrates that the experimental values compare favourably with the theoretical prediction, and hence the theoretical models may be used to predict the penetration distance for water injection within the ranges of this investigation.

Figures 35a and b are sample experimental and theoretical centreline paths for a range of initial injection angles. Agreement is quite good, except in the case of large upstream initial injection angles. An interesting feature of these graphs is that slight downstream injection gives better

---

* This corresponds to $\Lambda = 80°$ (approx.) for all values of Λ_o.

penetration than normal injection. This holds true for practically all the results obtained.

Figures 36a, b and c are sample experimental and theoretical centreline paths for a range of injectant total pressures. As previously, comparison yields reasonably good agreement except in the case of large upstream initial injection angles.

Figure 37 a, b and c are sample experimental and theoretical centreline paths for a range of initial injectant diameters. A complete examination of the experimental results seem to indicate that the initial injectant diameters do not influence the water jet centreline path significantly, although Figure 26 seems to show that larger diameters induce greater penetration into the freestream. The reason for this is that Figure 26 is a plot of maximum penetration distance, which experimentally includes the jet expansion. It is basically this expansion wich is larger for bigger diameters, primarily because of the larger mass flows.

4.4 Recommendations

It is apparent from the foregoing that the mathematical models postulated for incompressible fluids agree quite well with the experimental data obtained for water injection. It is suggested that experimental work be performed for non-reactive compressible (gaseous) injection, and a comparison be made with the theoretical models postulated in Section 2.3.

Future work should include an extension to the incompressible and compressible theoretical models to account for the viscous effects. The models could then be extended to allow the jets to deform.*

Keeping in mind the main objective of the overall investigation, work should be done to combine the injection model (with any future extensions) to the mixing and reaction aspects of supersonic combustion. An investigation should be performed on various injectant configurations, such as multiple injectors.

The favourable results obtained for water injection warrant a continuation of the study presented in this report.

---

*The basic theory for affinely similar deformable jets is treated in Reference 5.

5. CONCLUSIONS

This report presents simplified theoretical models, based on Newtonian flow concepts, for the prediction of the injectant path, and hence the penetration distance for both gaseous (compressible) and liquid (incompressible) secondary injection into a supersonic stream.

Experimentation shows that it is possible to achieve significant penetration distances (for spontaneous supersonic combustion) by injecting from a wall orifice. Experiments were performed for water injection into a Mach 3 supersonic airstream, for ranges of initial injection angle (28° upstream to 31° downstream), injector diameters (0.014 in. to 0.035 in.) and injectant total pressures (65 psia to 365 psia). The total number of different runs, from which results were obtained, was 105.

Good correlation between the theoretical model and the experimental results for liquid (water) injection into a Mach 3 airstream was obtained for normal and downstream injection. Large upstream injection resulted in poor correlation for the jet centreline paths, but good correlation for the penetration distances, since the jet reached its penetration distance much faster than that predicted by the theoretical model. Medium size orifices (.018 in. to .030 in. diameters) and high pressures gave good correlation, while very small and very large diameters, along with low pressures (less than 165 psia) tended to give penetration distances which were less than those predicted by the theoretical model.

The maximum penetration (at outer edge of jet) is dependent on the initial angle of injection, the injectant total pressure and the injectant orifice diameter. The maximum penetration increases with the latter two, while upstream injection gives much greater penetration than either normal or downstream injection. Centreline penetration results are similar, with the exception of the independence of the injectant orifice diameter.

The simplicity of the theory and the accuracy with which it agrees with the experiments, would appear to favour the use of this approach for the theoretical prediction of penetration distances and paths for downstream and small angle upstream injection.

REFERENCES

1. Forde, J.M.
An Experimental Investigation of the Mixing of Supersonic Turbulent Streams of Non-Similar Fluids
Mechanical Engineering Research Laboratories, McGill University, Report 63-3, April 1963.

2. Billig, F.S.
A Study of Combustion in Supersonic Streams
Applied Physics Laboratory, Johns Hopkins University, Bumblebee Report No.321, July 1964.

3. Molder, S.
Unpublished Data
Mechanical Engineering Research Laboratories, McGill University, 1963.

4. Morgenthaler, J.H.
Supersonic Mixing of Hydrogen and Air
Applied Physics Laboratory, Johns Hopkins University, 1964.

5. Ferrari, C.
Interference Between a Jet Issuing Laterally from a Body and the Enveloping Supersonic Stream
Applied Physics Laboratory, Johns Hopkins University, Bumblebee Report No.286, April 1959.

6. Keffer, J.F. and Baines, W.D.
The Round Turbulent Jet in a Crosswind
J. Fluid Mech. 15, 481-496, 1963.

7. Clark, B.J.
Breakup of a Liquid Jet in a Transverse Flow of Gas
NASA TN D-2424, August 1964.

8. Abramovich, G.N.
The Theory of Turbulent Jets
M.I.T. Press, 1963.

9. Green, C.J. and McCullough, F.Jr.
Liquid Injection Thrust Vector Control
AIAA J. 1, 573-578, 1963.

10. Cubbison, R.W., Anderson, B.H. and Ward, J.J.
Surface Pressure Distributions with a Sonic Jet Normal to Adjacent Flat Surfaces at Mach 2.92 to 6.4
NASA TN D-580, February 1961.

11. Lefko, W.
Loads Induced on a Flat Plate at Mach Number of 4.5 with a Sonic or Supersonic Jet Exhausting Normal to the Surface
NASA TN D-1935, July 1963.

12. Janos, J.J.
Loads Induced on a Flat-Plate Wing by an Air Jet Exhausting Perpendicularly through the Plate and Normal to a Freestream Flow of Mach Number 2.0
NASA TN D-649, March 1961.

13. Attas, J.E.
Interaction Effects Produced by a Vapourizing Liquid Injected into a High Energy Supersonic Gas Stream
Mechanical Engineering Research Laboratories, McGill University, Report 63-2, April 1963.

14. McRee, D.I., Peterson, J.B.Jr. and Braslow, A.L.
Effect of Air Injection through a Porous Surface and through Slots on Turbulent Skin Friction at Mach 3
NASA TN D-2427, August 1964.

15. Zukoski, E.E. and Spaid, F.W.
Secondary Injection of Gases into a Supersonic Flow
AIAA Journal, Vol.2, No.10, pps.1689 - 1696, Oct. 1964.

16. Dowdy, M.W. and Newton, J.F.
Investigation of Liquid and Gaseous Secondary Injection Phenomena on a Flat Plate with M = 2.01 to M = 4.54
Jet Propulsion Laboratory, California Institute of Technology, Tech. Report No.32-542, December 1963.

17. Shandorov, G.S.
Flow from a Channel into Stationary and Moving Media
Zh. Tekhn. Fiz., 1, 1957.

18. Shapiro, A.H.
The Dynamics and Thermodynamics of Compressible Fluid Flow
Ronald Press, 1953.

19. Ames Research Staff
Equations, Tables and Charts for Compressible Flow
NACA Report 1135, 1953.

20. Forde, J.M., Ahmed, A.M. and Szpiro, E.J.
The McGill University High Enthalpy Supersonic Wind Tunnel
Mechanical Engineering Research Laboratories, McGill University, Tech. Note 64-9, December 1964.

21. Valenti, A.M.
A Digital Computer Program for the Calculation of Supersonic Wind Tunnel Nozzle Coordinates
Mechanical Engineering Research Laboratories, McGill University, Memo. 62-2, November 1961.

22. Hunsaker, J.C. and Rightmire, B.G.
Engineering Applications of Fluid Mechanics
McGraw Hill Book Co., Inc., 1947.

23. Valenti, A.M.
Spontaneous Combustion of Hydrogen in Hot Air at an Initial Mach Number of 3.86
Mechanical Engineering Research Laboratories, McGill University, Report 62-7, October 1962.

24. Molder, S.
A Fortran Program for the Calculation of Laminar and Turbulent Boundary Layers
Unpublished
Mechanical Engineering Research Laboratories, McGill University, 1964.

APPENDIX A

DERIVATION OF COMPRESSIBLE JET FLOW EQUATIONS

Appendix A1 Derivation of Single Circular Port Equation (23)

The sum of the pressure forces on an element is:

$$dF_x = 2 \int_{\phi=0}^{\phi=\pi/2} C_p\, q_\infty \cos\Lambda \cos\phi \, dS \qquad \ldots.(A-1)$$

where from geometry (Fig. 3)

$$d\,S = \frac{D_j}{2}\, dl\, d\phi$$

$$\sin\delta = \cos\Lambda \cos\phi \qquad \ldots.(A-2)$$

$$A_j = \frac{\pi}{4} D_j^{\,2}$$

Also for a regular Newtonian pressure coefficient

$$C_p = C_{p_{reg.Newt.}} = 2\sin^2\delta \qquad \ldots.(A-3)$$

substituting Equations (A-2) and (A-3) into Equation (A-1) and integrating, gives:

$$dF_x = 2\int_{\phi=0}^{\phi=\frac{\pi}{2}} q_\infty\; 2\cos^2\Lambda \cos^2\phi \cos\Lambda \cos\phi \,\frac{D_j}{2}\, dl\, d\phi$$

$$= 2\, q_\infty D_j \cos^3\Lambda \; dl \int_0^{\pi/2} \cos^3\phi \, d\phi$$

$$= \frac{4}{3} D_j\, q_\infty \cos^3\Lambda \;\; dl \qquad \ldots.(A-4)$$

Now, the rate of change of momentum in the x-direction of the element is:

$$\frac{d}{dt}\,(\text{Mass}\cdot V_x) = \frac{d}{dt}\,(\rho_j\, A_j\, dl\, V_j \sin\Lambda)$$

$$= \frac{d}{dt}(\rho_j A_j \; V_j \; dl \; \sin\Lambda)$$

$$= m_j \frac{d}{dt} (\; dl \; \sin\Lambda)$$

$$= m_j \; \sin\Lambda \frac{d(dl)}{dt} + m_j \; dl \; \cos\Lambda \; \frac{d\Lambda}{dl} \; \frac{dl}{dt}$$

$$= m_j \; \sin\Lambda \; dV_j + m_j V_j \; \cos\Lambda dl \qquad \ldots .(A\text{-}5)$$

Equating Equations (A-4) and (A-5) with a factor for units gives:

$$\frac{4}{3} D_j \; q_\infty \; \cos^3\Lambda \; dl = \frac{m_j}{g} \sin\Lambda \, dV_j + \frac{m_j}{g} V_j \; \cos\Lambda \, d\Lambda$$

and

$$\frac{4}{3} \frac{g}{m_j} q_\infty D_j \; \left(\frac{\cos^3\Lambda}{\sin\Lambda} \right) = V_j \left(\frac{\cos\Lambda}{\sin\Lambda} \right) \frac{d\Lambda}{dl} + \frac{dV_j}{dl} \qquad \ldots .(A\text{-}6)$$

Now, by definition

$$M_j = \frac{V_j}{a_j} = \frac{V_j}{\sqrt{\gamma_j R_j T_j g}} \qquad \ldots .(A\text{-}7)$$

Also for isentropic flow

$$T_j = T_{tj} \; \left(1 + \frac{\gamma_j - 1}{2} M_j^2 \right)^{-1} \qquad \ldots .(A\text{-}8)$$

Combining Equations (A-7) and (A-8) gives:

$$V_j = \sqrt{\gamma_j \; R_j \; T_{tj} \; g} \; \frac{M_j}{\left(1 + \frac{\gamma_j - 1}{2} M_j^2\right)^{1/2}} \qquad \ldots .(A\text{-}9)$$

Also by definition,

$$C_p = C_{p_{\text{reg. Newt.}}} = \frac{P_b - P_\infty}{q_\infty} = 2 \; \cos^2\Lambda \qquad \ldots .(A\text{-}10)$$

and by Assumption 5,

$$P_j = \frac{P_b + P_\infty}{2} \qquad \ldots .(A\text{-}11)$$

Combining Equations (A-10) and (A-11) gives:

$$P_j = q_\infty \cos^2\Lambda + P_\infty \qquad \text{....(A-12)}$$

Combining Equation (A-12) with the isentropic pressure relation

$$P_j = P_{tj} \left(1 + \frac{\gamma_j - 1}{2} M_j^2 \right)^{\frac{-\gamma_j}{\gamma_j - 1}} \qquad \text{....(A-13)}$$

gives:

$$M_j = \left(\frac{2}{\gamma_j - 1} \right)^{\frac{1}{2}} \left[\left(\frac{q_\infty}{P_{tj}} \cos^2\Lambda + \frac{P_\infty}{P_{tj}} \right)^{-\frac{\gamma_j - 1}{\gamma_j}} - 1 \right]^{\frac{1}{2}}$$

$$= \left(\frac{2}{\gamma_j - 1} \right)^{\frac{1}{2}} \left[z^{-\frac{\gamma_j - 1}{\gamma_j}} - 1 \right]^{\frac{1}{2}} \qquad \text{....(A-14)}$$

where by definition

$$z = z(\Lambda) = \frac{q_\infty}{P_{tj}} \cos^2\Lambda + \frac{P_\infty}{P_{tj}} \qquad \text{....(A-15)}$$

Substituting Equation (A-14) into (A-9) and differentiating w.r.t. l, will give:

$$\frac{dV_j}{dl} = \sqrt{\gamma_j R_j T_{tj} g} \, \frac{d}{dl} \left[\frac{M_j}{\left(1 + \frac{\gamma_j - 1}{2} M_j^2\right)^{1/2}} \right]$$

$$= \sqrt{\gamma_j R_j T_{tj} g} \left(\frac{2}{\gamma_j - 1} \right)^{\frac{1}{2}} \left[1 - z^{\frac{\gamma_j - 1}{\gamma_j}} \right]^{\frac{1}{2}} \qquad \text{....(A-16)}$$

Substituting Equations (A-9), (A-14) and (A-16) into Equation (A-6) will give, upon simplification

$$\frac{dl}{D_{jI}} = \frac{1 + C_1 z^{-1/\gamma_j} \left(1 - z^{\frac{\gamma_j - 1}{\gamma_j}}\right)^{-1} \sin^2\Lambda}{C_3 \cos^2\Lambda \, z^{-\frac{\gamma_j - 1}{\gamma_j}}} \, d\Lambda \qquad \text{....(A-17)}$$

where,

$$C_1 = \left(\frac{\gamma_j - 1}{\gamma_j} \right) \frac{q_\infty}{P_{tj}} \qquad \text{....(A-18)}$$

$$C_3 = \frac{16}{3\pi} \left(\frac{\gamma_j - 1}{2}\right)^{\frac{3}{4}} \cdot \left(\frac{\gamma_j + 1}{2}\right)^{\frac{\gamma_j + 1}{4(\gamma_j - 1)}} \frac{q_\infty \; g}{\left(\frac{m_j}{A_{jI}}\right) \sqrt{\gamma_j R_j T_{jt} \, g}} \qquad \text{....(A-19)}$$

which are Equations (23), (25) and (28) respectively.

Appendix A2 Derivation of Two-Dimensional Case Equation (24)

Similarly to the derivation in Appendix A1, for the two-dimensional case

$$dF_x = C_p \, q_\infty \cos\Lambda \; d\,S \qquad \text{....(A-20)}$$

where from geometry (Fig. 4),

$$dS = dl$$
$$\sin\delta = \cos\Lambda \qquad \text{....(A-21)}$$
$$A_j = b$$

Substituting Equations (A-3) and (A-21) into Equation (A-20) gives:

$$dF_x = 2 \, q_\infty \; \cos^3\Lambda \; dl \qquad \text{....(A-22)}$$

Also, the rate of change of momentum in the x-direction will give the same result as Equation (A-5), namely:

$$\frac{d}{dt} \left(\text{Mass } V_x\right) = m_j \sin\Lambda \, dV_j + m_j \, V_j \cos\Lambda \, d\Lambda \qquad \text{....(A-23)}$$

Equating Equations (A-22) and (A-23) gives:

$$\frac{2g \; q_\infty}{m_j} \left(\frac{\cos^3\Lambda}{\sin\Lambda}\right) = V_j \; \left(\frac{\cos\Lambda}{\sin\Lambda}\right) \frac{d\Lambda}{dl} + \frac{dV_j}{dl} \qquad \text{....(A-24)}$$

Using the same method as Appendix A1, substituting Equations (A-9), (A-14) and (A-16) into Equation (A-24), will yield upon simplification:

$$\frac{dl}{b} = \frac{(1 - z^{\frac{\gamma_j - 1}{\gamma_j}})^{\frac{1}{2}} + C_1 z^{-1/\gamma_j} (1 - z^{\frac{\gamma_j - 1}{\gamma_j}})^{-\frac{1}{2}} \sin^2\Lambda}{C_2 \cos^2\Lambda} d\Lambda \quad \text{....(A-25)}$$

where,

$$C_2 = \left(\frac{\gamma_j - 1}{j} \right)^{\frac{1}{2}} \frac{2 q_\infty g}{(\frac{m_j}{b}) \sqrt{\gamma_j R_j T_{tj} g}} \quad \text{....(A-26)}$$

which are Equations (24) and (27) respectively.

Appendix A3 Derivation of Equation (29)

From Assumption 7,

$$M_{jI} = 1 \quad \text{....(A-27)}$$

Now by definition

$$\begin{aligned} m_j &= \rho_{jI} A_{jI} V_{jI} \\ &= \rho_{jI} A_{jI} M_{jI} \sqrt{\gamma_j R_j T_{jI} g} \\ &= \rho_{jI} A_{jI} \sqrt{\gamma_j R_j T_{jI} g} \quad \text{....(A-28)} \end{aligned}$$

Also from the isentropic density relation

$$\frac{\rho_{jI}}{\rho_{tj}} = \left(1 + \frac{\gamma_j - 1}{2} M_{jI}^2 \right)^{-\frac{1}{\gamma_j - 1}}$$

and

$$\rho_{jI} = \rho_{tj} \left(1 + \frac{\gamma_j - 1}{2} \right)^{-\frac{1}{\gamma_j - 1}} \quad \text{....(A-29)}$$

Also

$$\begin{aligned} T_{jI} &= T_{tj} \left(1 + \frac{\gamma_j - 1}{2} M_{jI}^2\right)^{-1} \\ &= T_{tj} \left(1 + \frac{\gamma_j - 1}{2} \right)^{-1} \quad \text{....(A-30)} \end{aligned}$$

Substituting Equations (A-29) and (A-30) into Equation (A-28) and simplifying gives:

$$\frac{m_j}{A_{jI}} = \left(\frac{\gamma_j+1}{2} \right)^{\frac{\gamma_j+1}{2(\gamma_j-1)}} \cdot \rho_{jt} \sqrt{\gamma_j R_j T_{tj} g} \qquad \text{....(A-31)}$$

Now from the Ideal Gas Law

$$P_{tj} = \rho_{tj} R_j T_{tj} \qquad \text{....(A-32)}$$

Substituting Equation (A-32) into Equation (A-31) gives:

$$\frac{m_j}{A_{jI}} = \left(\frac{\gamma_j+1}{2} \right)^{\frac{\gamma_j+1}{2(\gamma_j-1)}} \cdot \left(\frac{\gamma_j g}{R_j} \right)^{1/2} \frac{P_{tj}}{\sqrt{T_{tj}}} \qquad \text{....(A-33)}$$

which is Equation (29).

APPENDIX B

DERIVATION OF INCOMPRESSIBLE JET FLOW EQUATIONS

As shown in Sect. 2.3, the momentum equation can be reduced to Equation 3.

$$dF_x = \frac{d}{dt}\left(\text{Mass} \cdot V_x\right) \qquad \text{.....(B-1)}$$

The pressure coefficient can be written as follows:

$$C_p = K_1 \sin^2\delta \qquad \text{....(B-2)}$$

where $K_1 = 2$ for regular Newtonian C_p

$= \dfrac{C_{p*}}{\sin^2\delta*}$ for modified Newtonian C_p

where $\dfrac{C_{p*}}{\sin^2\delta*} = C_{p*}$ since $\delta* = \pi/2$

$$= \frac{P_b - P_\infty}{q_\infty} = \frac{(P_b/P_\infty - 1)\, P_\infty}{\frac{1}{2}\gamma_\infty P_\infty M_\infty^2}$$

$$= \frac{2}{\gamma_\infty M_\infty^2}\left\{\left[\frac{\gamma_\infty + 1}{2\gamma_\infty M_\infty^2 - (\gamma_\infty - 1)}\right]^{\frac{1}{\gamma_\infty+1}}\left[\frac{(\gamma_\infty + 1)M_\infty^2}{2}\right]^{\frac{\gamma_\infty}{\gamma_\infty-1}} - 1\right\} \qquad \text{....(B-3)}$$

which is equation (42)

Appendix B1 Derivation of Jet Tube Equations (34), (35), (38) and (39)

The pressure force in the x-direction on an element of the jet tube is:

$$dF_x = 2\int_{\phi=0}^{\pi/2} C_p\, q_\infty \cos\Lambda \cos\phi\, dS \qquad \text{.....(B-4)}$$

From geometry (Fig. 7)

$$dS = \frac{D_j}{2}\, dl\, d\phi$$

$$\sin \delta = \cos\Lambda \cos \phi \qquad \text{....(B-5)}$$

$$A_j = \frac{\pi}{4} D_j^2$$

Substituting Equations (B-2) and (B-5) into (B-4), rearranging and integrating gives:

$$dF_x = 2q_\infty \cos\Lambda \int_{\phi=0}^{\pi/2} K_1 \cos^2\Lambda \cos^2 \phi \frac{D_j}{2}\, dl\, d\phi$$

$$= K_1 D_j q_\infty \cos^3\Lambda\, dl \int_0^{\pi/2} \cos^3 \phi\, d\phi$$

$$= \frac{2}{3} K_1 D_j q_\infty \cos^3\Lambda\, dl \qquad \text{....(B-6)}$$

Now, the rate of momentum change in the x-direction for an element of the jet tube is:

$$\frac{d}{dt}(\text{Mass}\cdot V_x) = \frac{d}{dt} (\rho_j A_j\, dl\, V_j \sin\Lambda)$$

$$= \rho_j \frac{\pi}{4} D_j^2\, dl\, V_j \frac{d(\sin\Lambda)}{d\Lambda} \frac{dl}{dt} \frac{d\Lambda}{dl}$$

$$= \frac{\pi}{4} \rho_j D^2_j V_j\, dl \cos\Lambda\, V_j \frac{d\Lambda}{dl}$$

$$= \frac{\pi}{2} (\tfrac{1}{2} \rho_j V_j^2) D_j^2 \cos\Lambda\, d\Lambda$$

$$= \frac{\pi}{2} q_j D_j^2 \cos\Lambda\, d\Lambda \qquad \text{....(B-7)}$$

Equating Equations (B-6) and (B-7), as specified by equation (B-1) gives:

$$\frac{2}{3} K_1 D_j q_\infty \cos^3\Lambda\, dl = \frac{\pi}{2} q_j D_j^2 \cos\Lambda\, d\Lambda$$

which can be rearranged to,

$$dl = \frac{3\pi}{2K_1}\left(\frac{D_j}{2}\,\frac{q_j}{q_\infty}\right)\frac{d\Lambda}{\cos^2\Lambda} \qquad \ldots.(B\text{-}8)$$

Also from geometry (Fig. 7)

$$\begin{aligned} dx &= dl\ \sin\Lambda \\ dy &= dl\ \cos\Lambda \end{aligned} \qquad \ldots.(B\text{-}9)$$

Substituting Equations (B-9) into (B-8) and integrating gives relations for x and y.

$$\begin{aligned} x &= \frac{3\pi}{2K_1}\left(\frac{D_j}{2}\,\frac{q_j}{q_\infty}\right)\int_{\Lambda_o}^{\Lambda}\frac{\sin\Lambda\ d\Lambda}{\cos^2\Lambda} \\ &= \frac{3\pi}{2K_1}\left(\frac{D_j}{2}\,\frac{q_j}{q_\infty}\right)\left[\frac{1}{\cos\Lambda}-\frac{1}{\cos\Lambda_o}\right] \end{aligned} \qquad \ldots.(B\text{-}10)$$

and

$$\begin{aligned} y &= \frac{3\pi}{2K_1}\left(\frac{D_j}{2}\,\frac{q_j}{q_\infty}\right)\int_{\Lambda_o}^{\Lambda}\frac{d\Lambda}{\cos\Lambda} \\ &= \frac{3\pi}{2K_1}\left(\frac{D_j}{2}\,\frac{q_j}{q_\infty}\right)\frac{1}{2}\ln\left[\frac{1+\sin\Lambda}{1-\sin\Lambda}\cdot\frac{1-\sin\Lambda_o}{1+\sin\Lambda_o}\right] \end{aligned} \qquad ..(B\text{-}11)$$

Non-dimensionalizing x and y in Equations (B-10) and (B-11), and substituting the appropriate value of K_1 will yield the required equations as follows:

Regular Newtonian C_p:

$$\bar{x} = \left(\frac{x}{D_j/2}\,\frac{q_\infty}{q_j}\right) = \frac{3}{4}\pi\left[\frac{1}{\cos\Lambda}-\frac{1}{\cos\Lambda_o}\right] \qquad \ldots.(B\text{-}12)$$

$$\bar{y} = \left(\frac{y}{D_j/2}\,\frac{q_\infty}{q_j}\right) = \frac{3}{8}\pi\ \ln\left[\frac{1+\sin\Lambda}{1-\sin\Lambda}\cdot\frac{1-\sin\Lambda_o}{1+\sin\Lambda_o}\right] \qquad \ldots(B\text{-}13)$$

which are Equations (34) and (35).

Modified Newtonian C_p:

$$\bar{x} = \left(\frac{x}{D_j/2}\,\frac{q_\infty}{q_j}\right) = \left(\frac{2}{C_{p*}/\sin^2\delta*}\right)\frac{3\pi}{4}\left[\frac{1}{\cos\Lambda} - \frac{1}{\cos\Lambda_o}\right] \quad ..(B\text{-}14)$$

$$\bar{y} = \left(\frac{y}{D_j/2}\,\frac{q_\infty}{q_j}\right) = \left(\frac{2}{C_{p*}/\sin^2\delta*}\right)\frac{3\pi}{8}\ \ln\left[\frac{1+\sin\Lambda}{1-\sin\Lambda}\,\frac{1-\sin\Lambda_o}{1+\sin\Lambda_o}\right] \quad ..(B\text{-}15)$$

which are Equations (38) and (39), and where $(C_{p*}/\sin^2\delta*)$ is defined in Equation (B-3).

Appendix B2 Derivation of Jet Sheet Equations (36), (37), (40) and (41)

The pressure force in the x-direction on an element of the jet sheet is:

$$dF_x = C_p\ q_\infty\ \cos\Lambda\ dS \quad ....(B\text{-}16)$$

From geometry (Fig. 8)

$$dS = dl$$

$$\sin\delta = \cos\Lambda \quad ....(B\text{-}17)$$

$$A_j = b$$

Substituting Equations (B-17) into (B-16) gives,

$$dF_x = K_1\ q_\infty\ \cos^3\Lambda\ dl \quad ....(B\text{-}18)$$

Similarly to the jet tube, the rate of momentum change in the x-direction for an element of the jet sheet is:

$$\frac{d}{dt}\,(\text{Mass}\cdot V_x) = \frac{d}{dt}\,(\ \rho_j\ A_j\ dl\ V_j\ \sin\Lambda\ )$$

$$= 2b\ q_j\ \cos\Lambda\ d\Lambda \quad ....(B\text{-}19)$$

Equating (B-18) and (B-19),

$$K_1 \, q_\infty \, \cos^3\Lambda \, dl = 2 \, b \, q_j \, \cos\Lambda \, d\Lambda$$

and

$$dl = \frac{4}{K_1} \left(\frac{b}{2} \frac{q_j}{q_\infty} \right) \frac{d\Lambda}{\cos^2\Lambda} \qquad \text{..........(B-20)}$$

Substituting Equations (B-9) and (B-2) into (B-20), non-dimensionalizing and integrating will yield:

Regular Newtonian C_p:

$$\bar{x} = \frac{x}{(b/2)} \frac{q_\infty}{q_j} = 2 \quad \frac{1}{\cos\Lambda} - \frac{1}{\cos\Lambda_o} \qquad \text{...... (B-21)}$$

$$\bar{y} = \frac{y}{(b/2)} \frac{q_\infty}{q_j} = \ln \quad \frac{1 + \sin\Lambda}{1 - \sin\Lambda} \; \frac{1 - \sin\Lambda_o}{1 + \sin\Lambda_o} \qquad \text{.....(B-22)}$$

which are Equations (36) and (37).

Modified Newtonian C_p:

$$\bar{x} = \frac{x}{(b/2)} \frac{q_\infty}{q_j} = \left(\frac{2}{C_{p*}/\sin^2\delta^*}\right) 2\left[\frac{1}{\cos\Lambda} - \frac{1}{\cos\Lambda_o}\right] \qquad \text{....(B-23)}$$

$$\bar{y} = \frac{y}{(b/2)} \frac{q_\infty}{q_j} = \left(\frac{2}{C_{p*}/\sin^2\delta^*}\right) \ln\left[\frac{1+\sin\Lambda}{1-\sin\Lambda} \; \frac{1-\sin\Lambda_o}{1+\sin\Lambda_o}\right] \qquad \text{....(B-24)}$$

which are Equations (40) and (41), and where $(C_{p*}/\sin^2\delta^*)$ is defined in Equation (B-3).

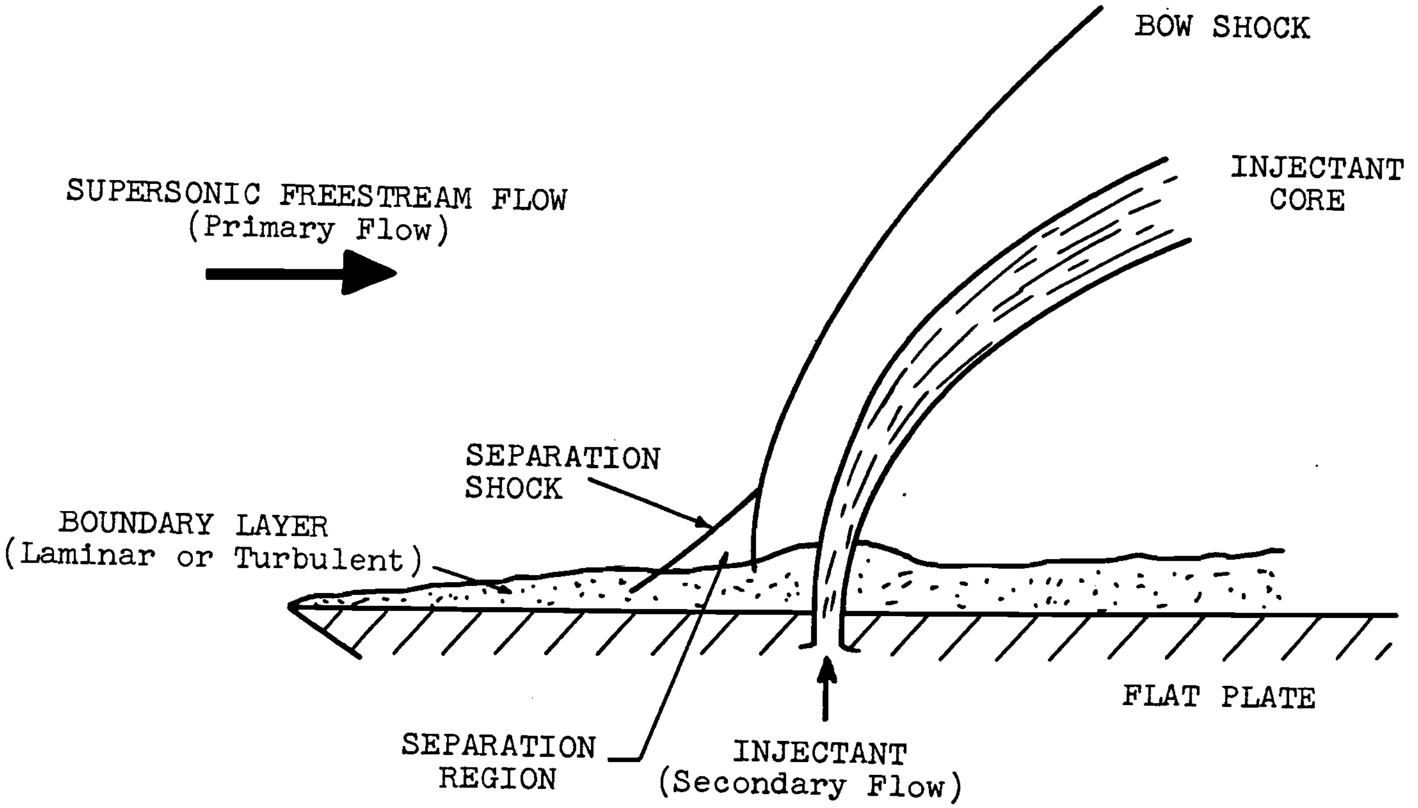

FIGURE 1 SKETCH OF INJECTANT FLOW FIELD

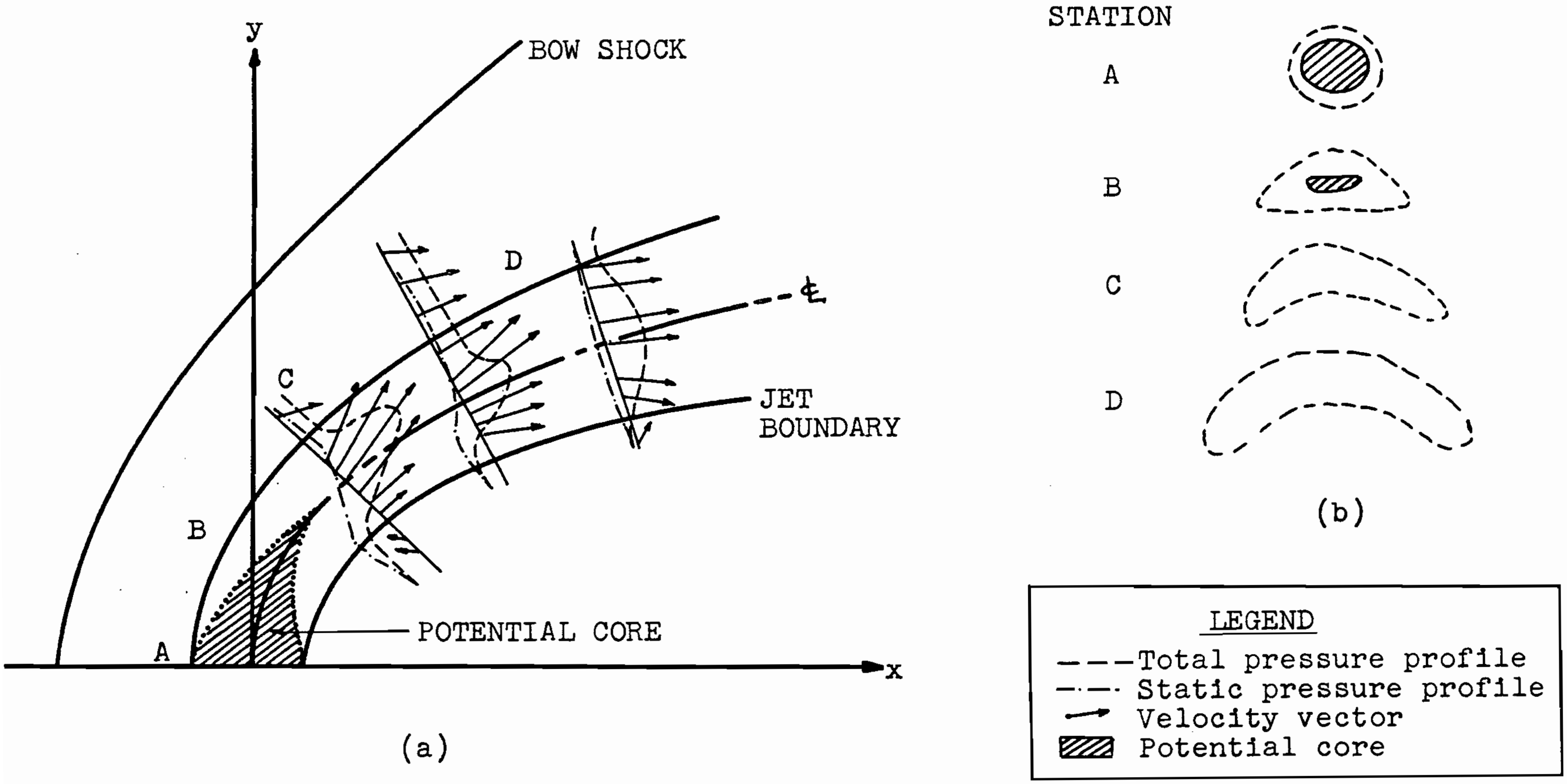

FIGURE 2 SKETCH OF A SECONDARY JET IN A LATERAL SUPERSONIC FLOW

Figure (a) shows velocity and pressure fields in the plane of symmetry of the jet. Figure (b) shows cross-sectional configurations at various distances from the first section. (Adapted from Reference 8.)

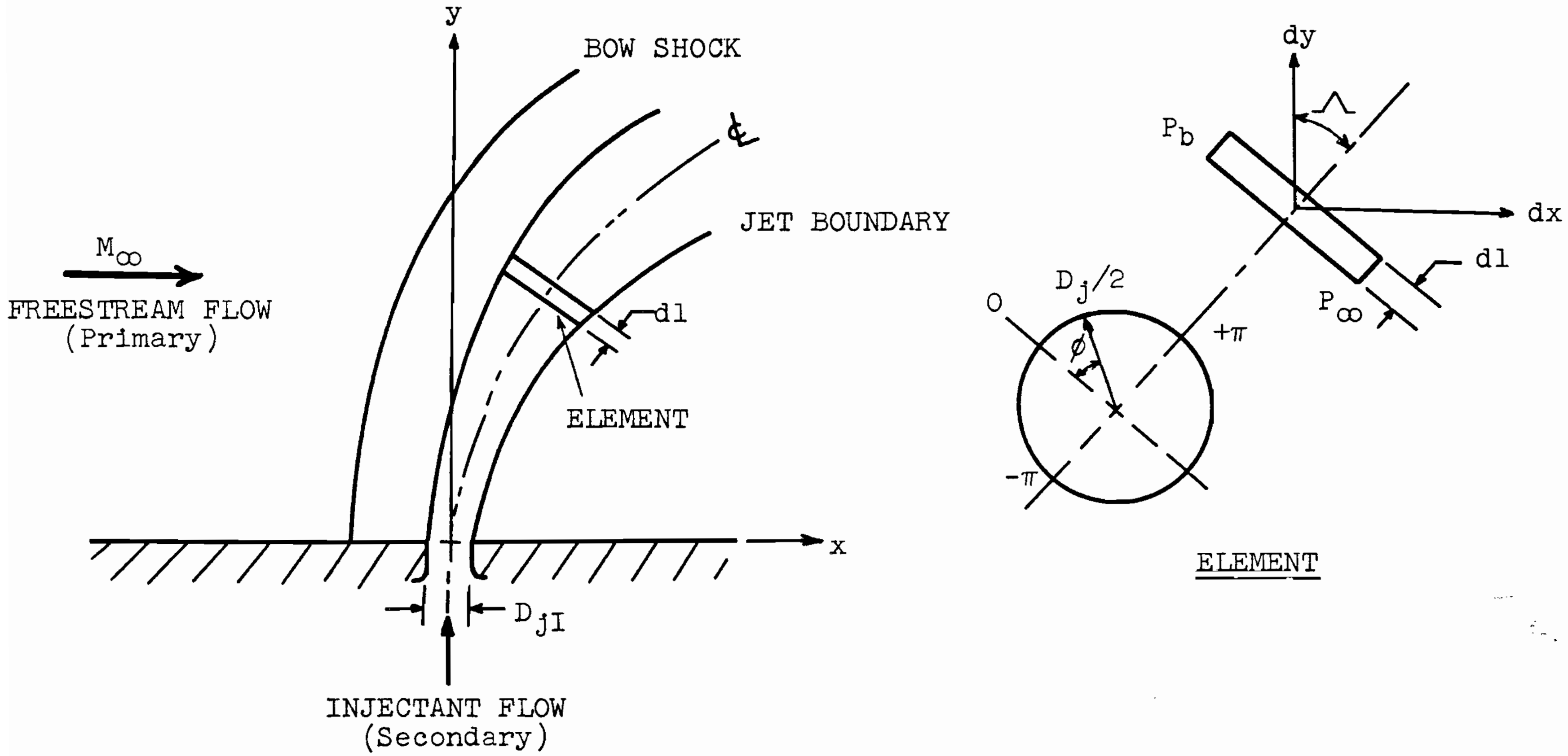

ELEMENT

FIGURE 3 MODEL OF THE THREE-DIMENSIONAL CIRCULAR COMPRESSIBLE INJECTANT FLOW CASE

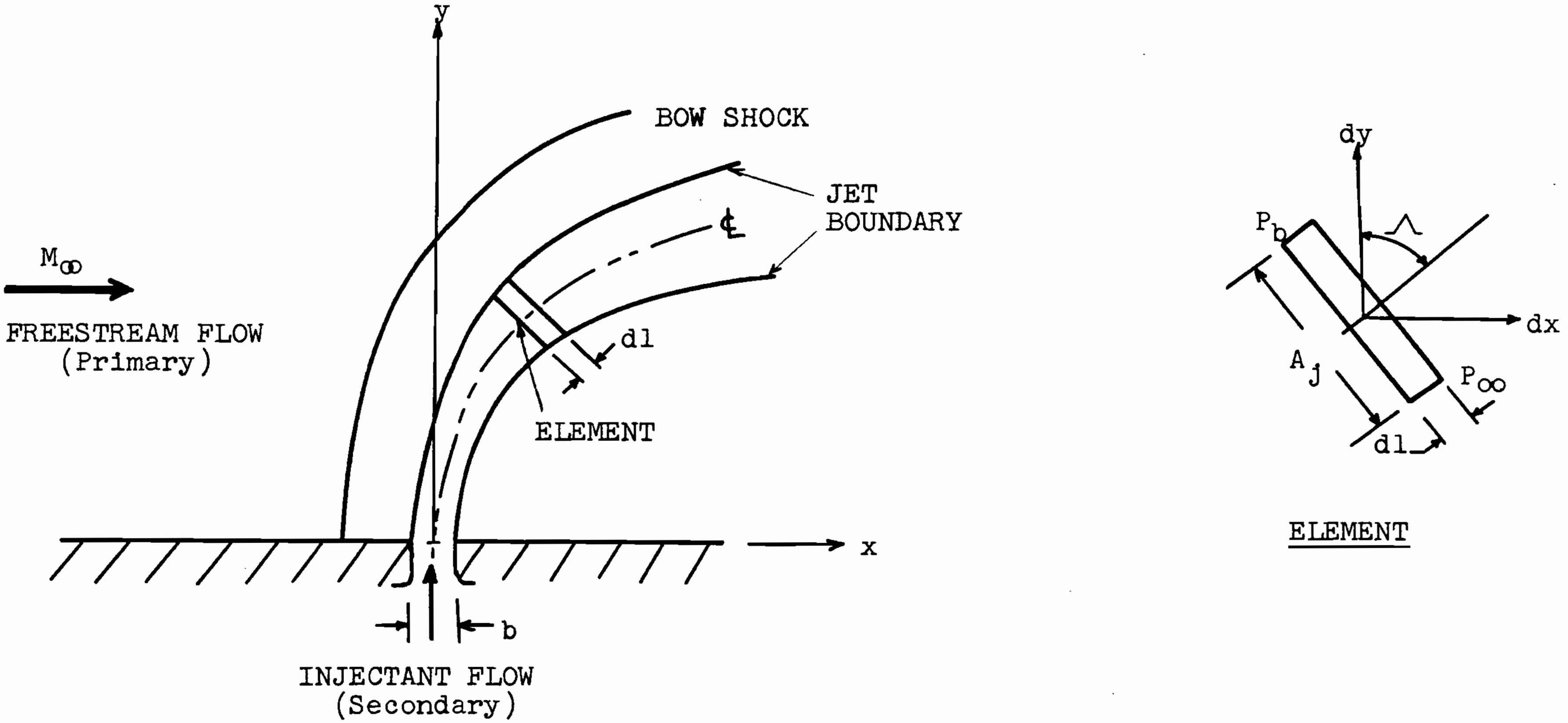

ELEMENT

FIGURE 4 MODEL OF THE TWO-DIMENSIONAL SHEET COMPRESSIBLE INJECTANT FLOW CASE

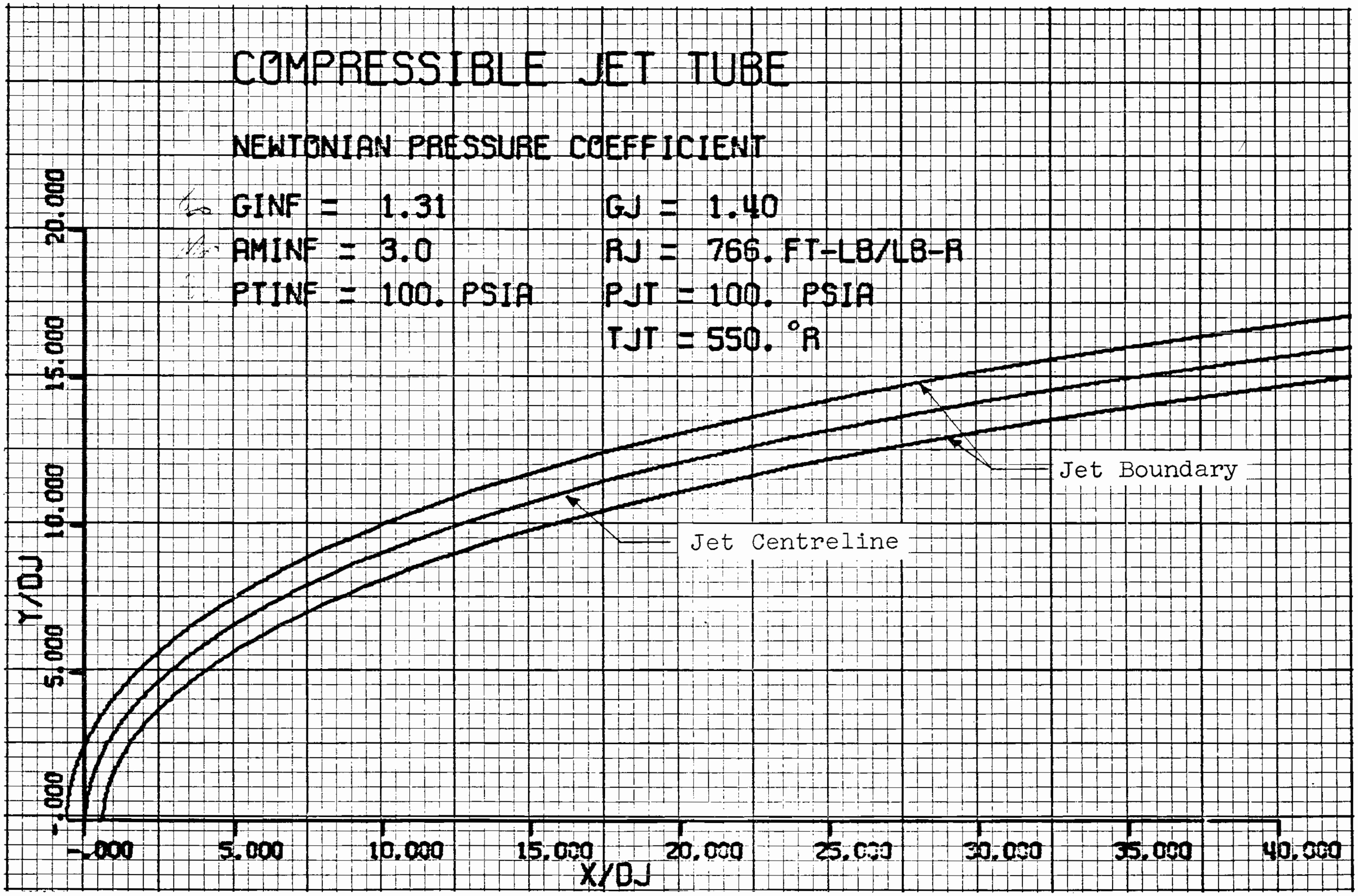

FIGURE 5 COMPUTER PLOT OF COMPRESSIBLE INJECTANT PATH FOR NORMAL INJECTION

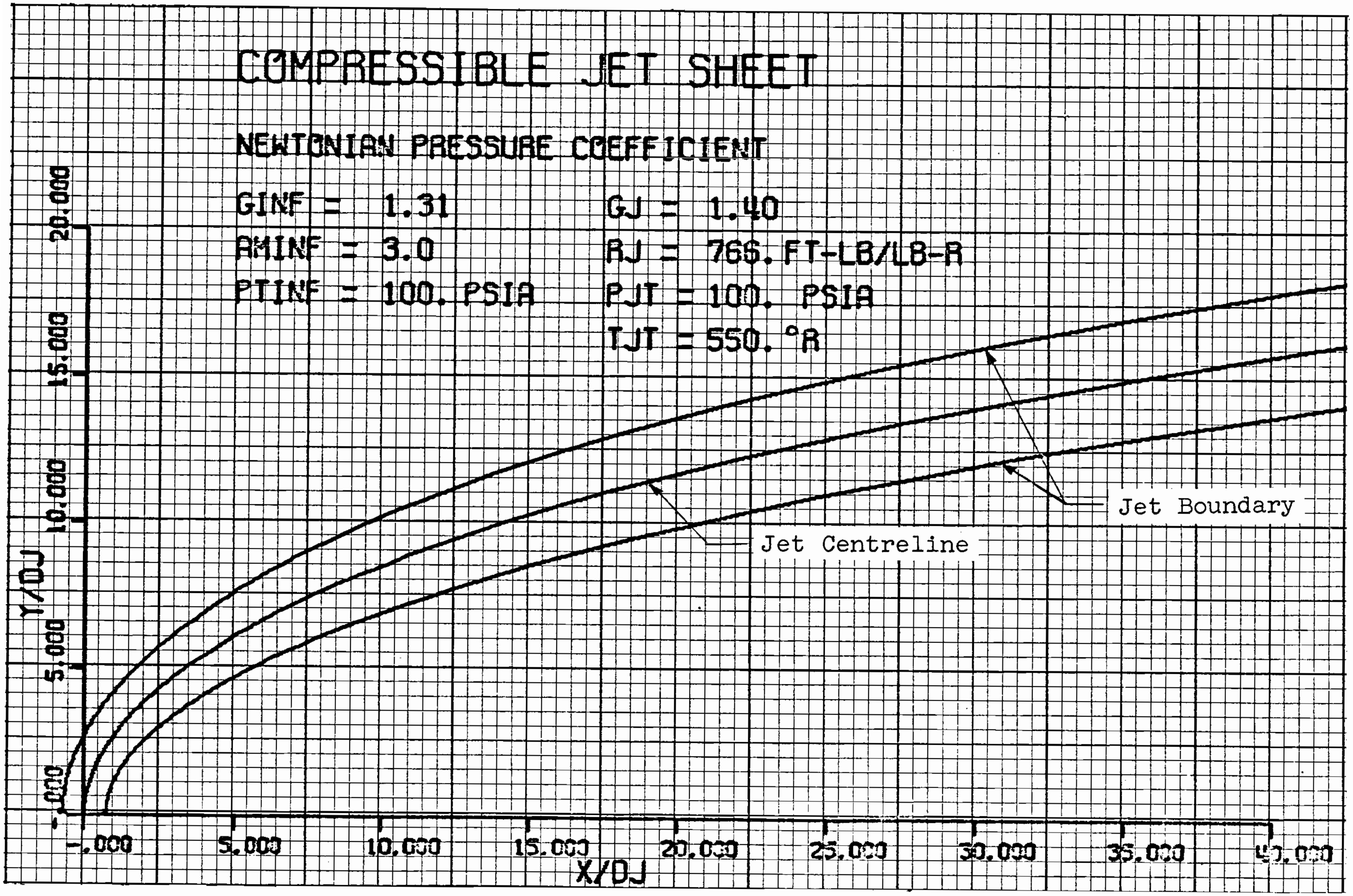

FIGURE 6 COMPUTER PLOT OF COMPRESSIBLE INJECTANT PATH FOR NORMAL INJECTION

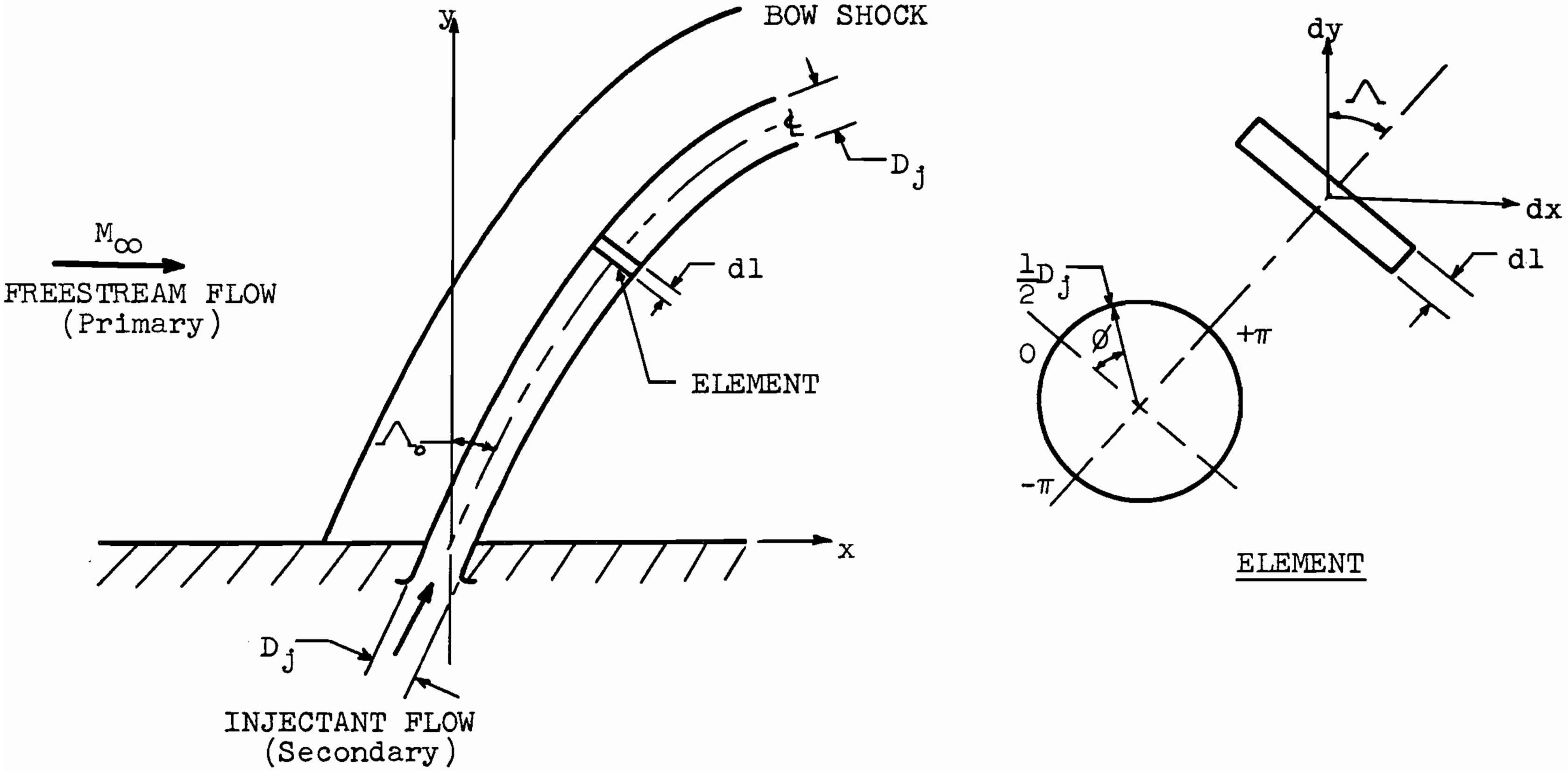

FIGURE 7 MODEL OF THE THREE-DIMENSIONAL INJECTANT JET TUBE CASE FOR INCOMPRESSIBLE SECONDARY FLOW

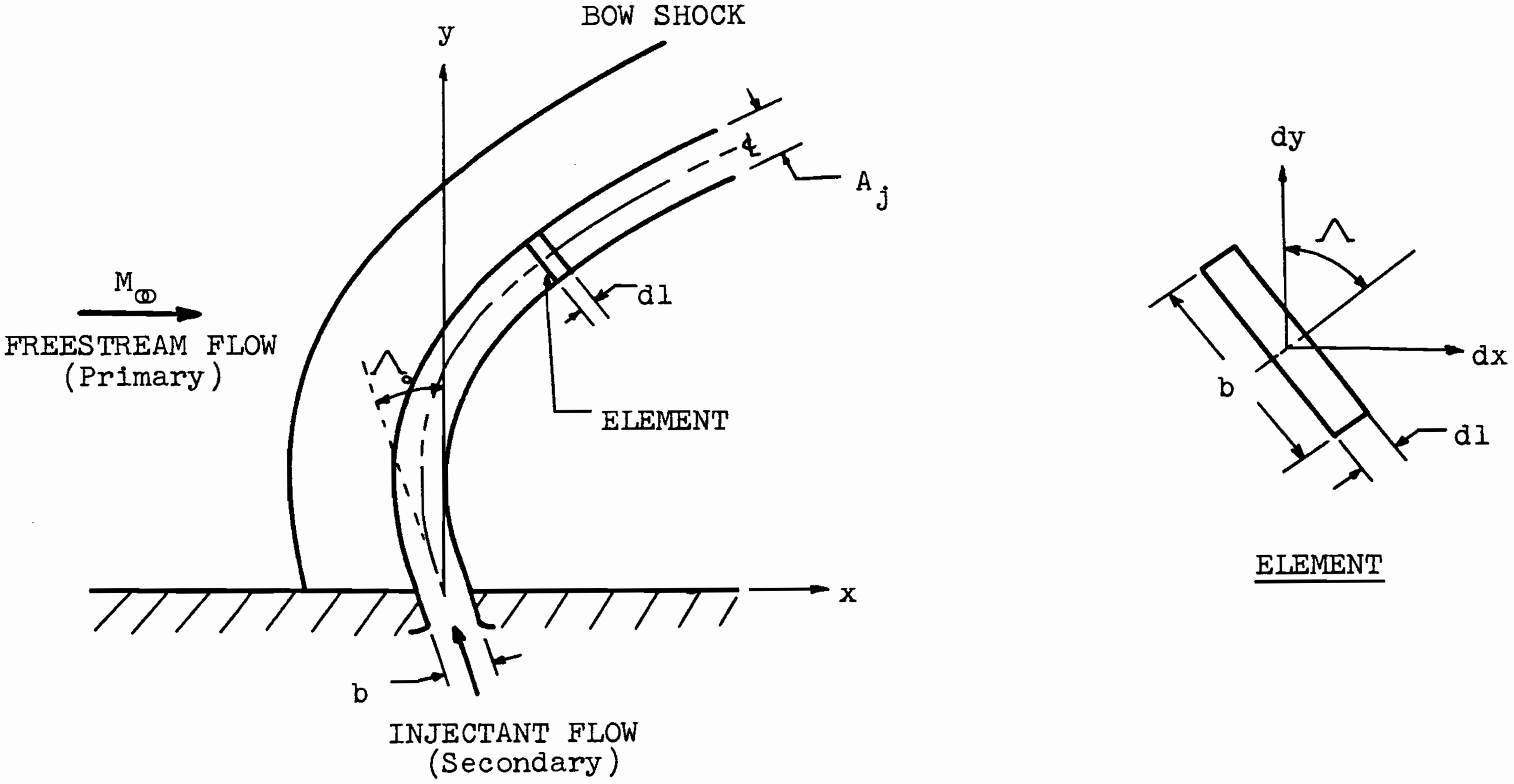

ELEMENT

FIGURE 8 MODEL OF THE TWO-DIMENSIONAL INJECTANT JET SHEET CASE FOR INCOMPRESSIBLE SECONDARY FLOW

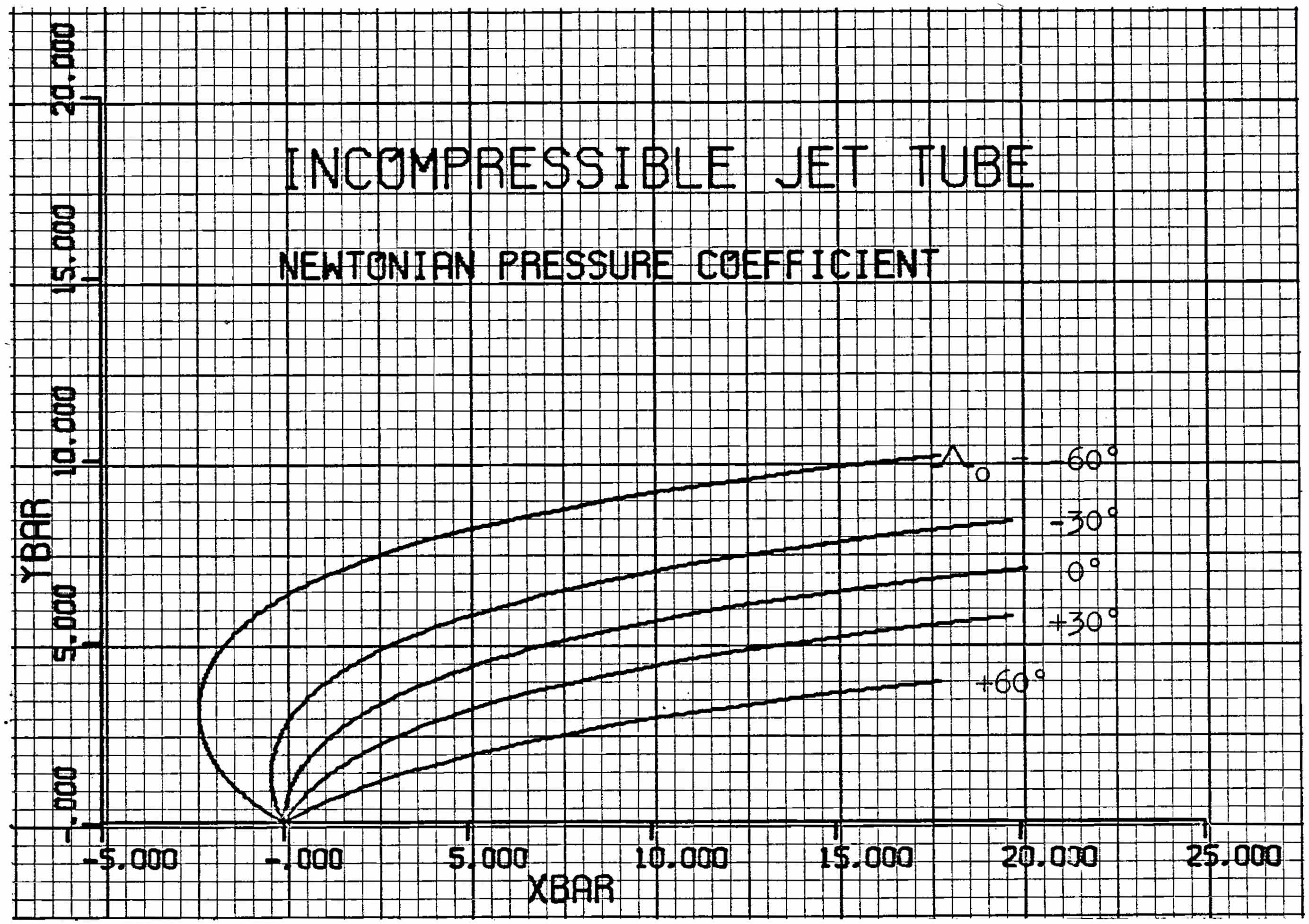

FIGURE 9 COMPUTER PLOT OF INCOMPRESSIBLE JET CENTRELINES FOR VARIOUS ANGLES OF INJECTION

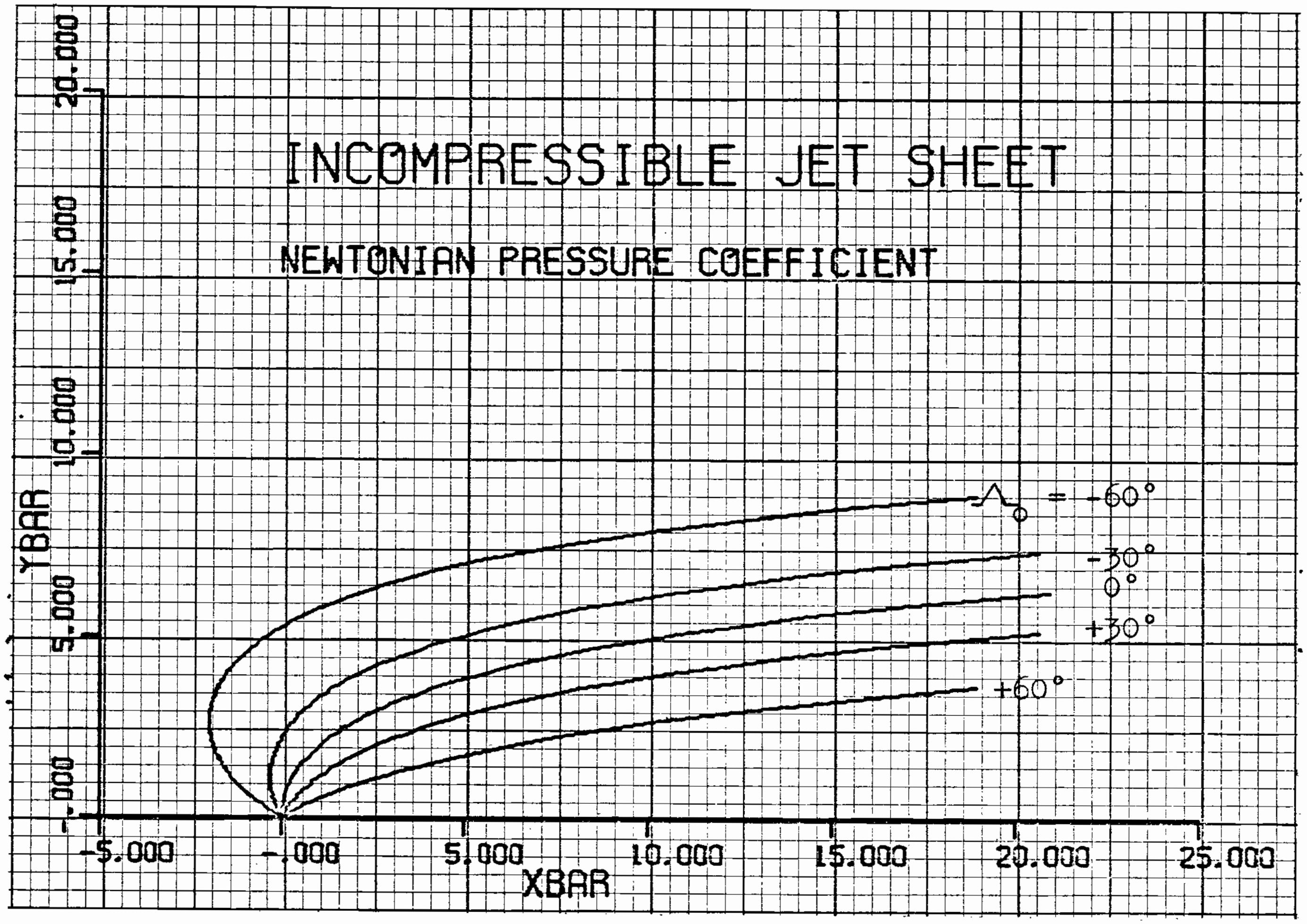

FIGURE 10 COMPUTER PLOT OF INCOMPRESSIBLE JET CENTRELINES FOR VARIOUS ANGLES OF INJECTION

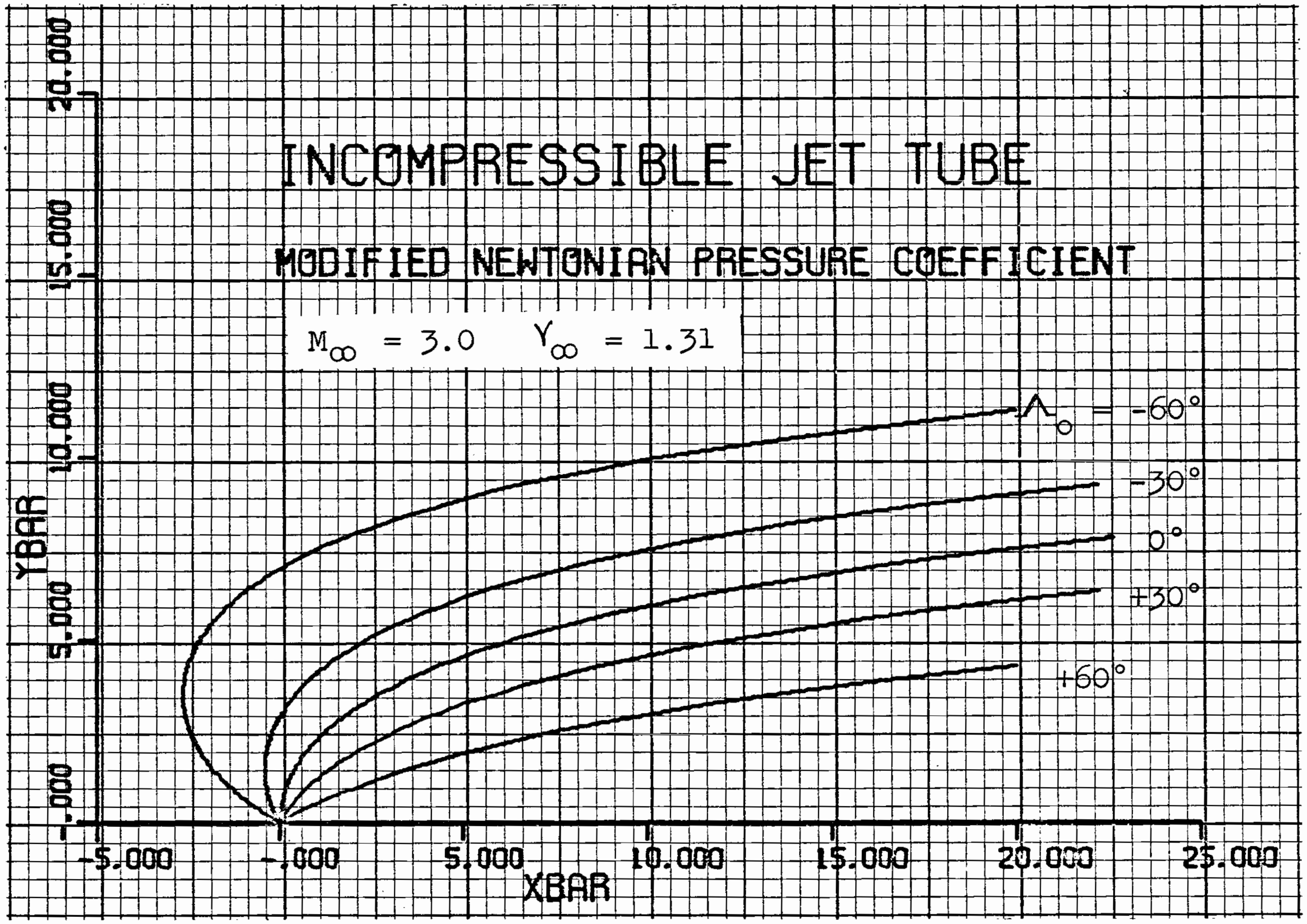

FIGURE 11 COMPUTER PLOT OF INCOMPRESSIBLE JET CENTRELINES FOR VARIOUS ANGLES OF INJECTION

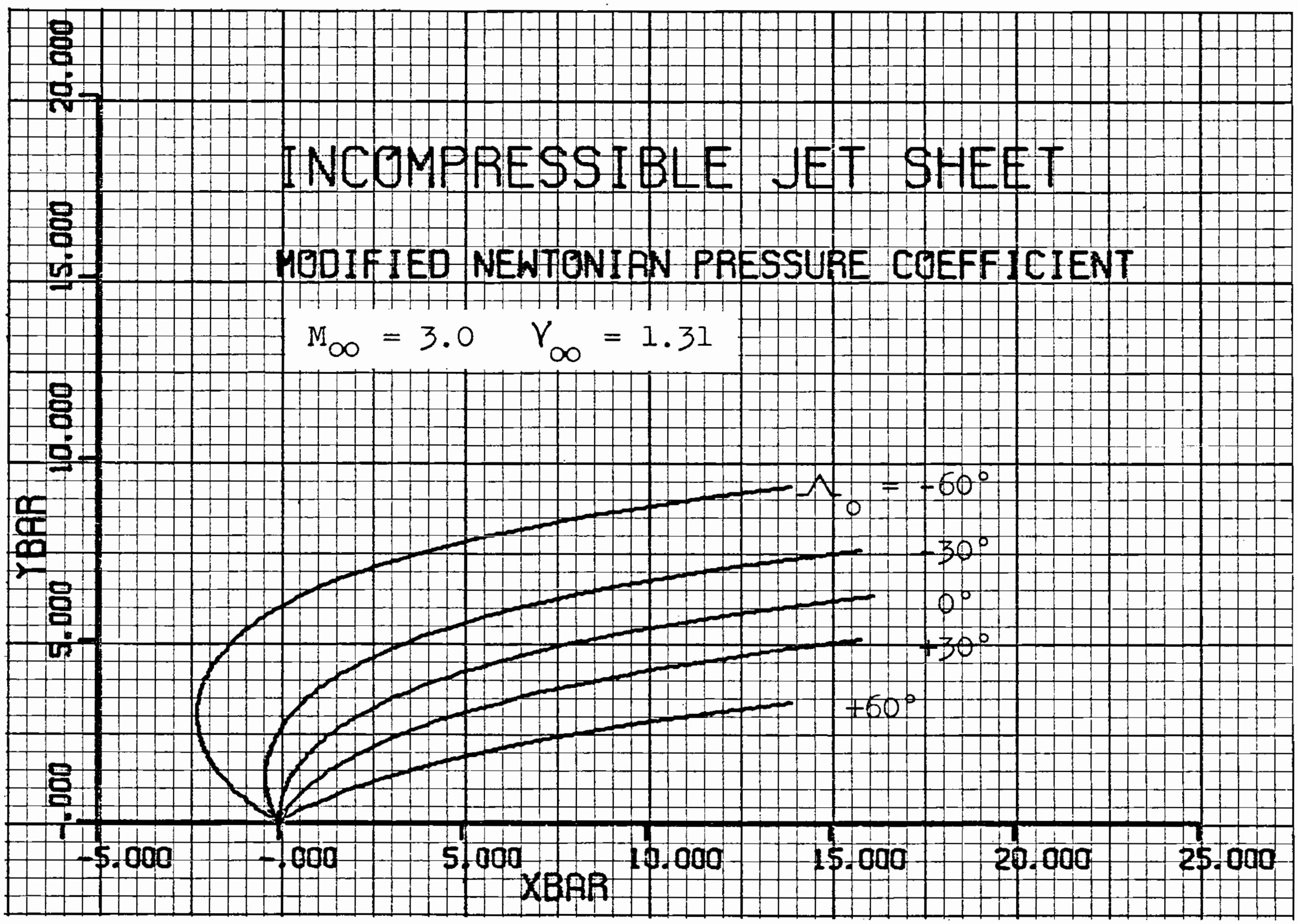

FIGURE 12 COMPUTER PLOT OF INCOMPRESSIBLE JET CENTRELINES FOR VARIOUS ANGLES OF INJECTION

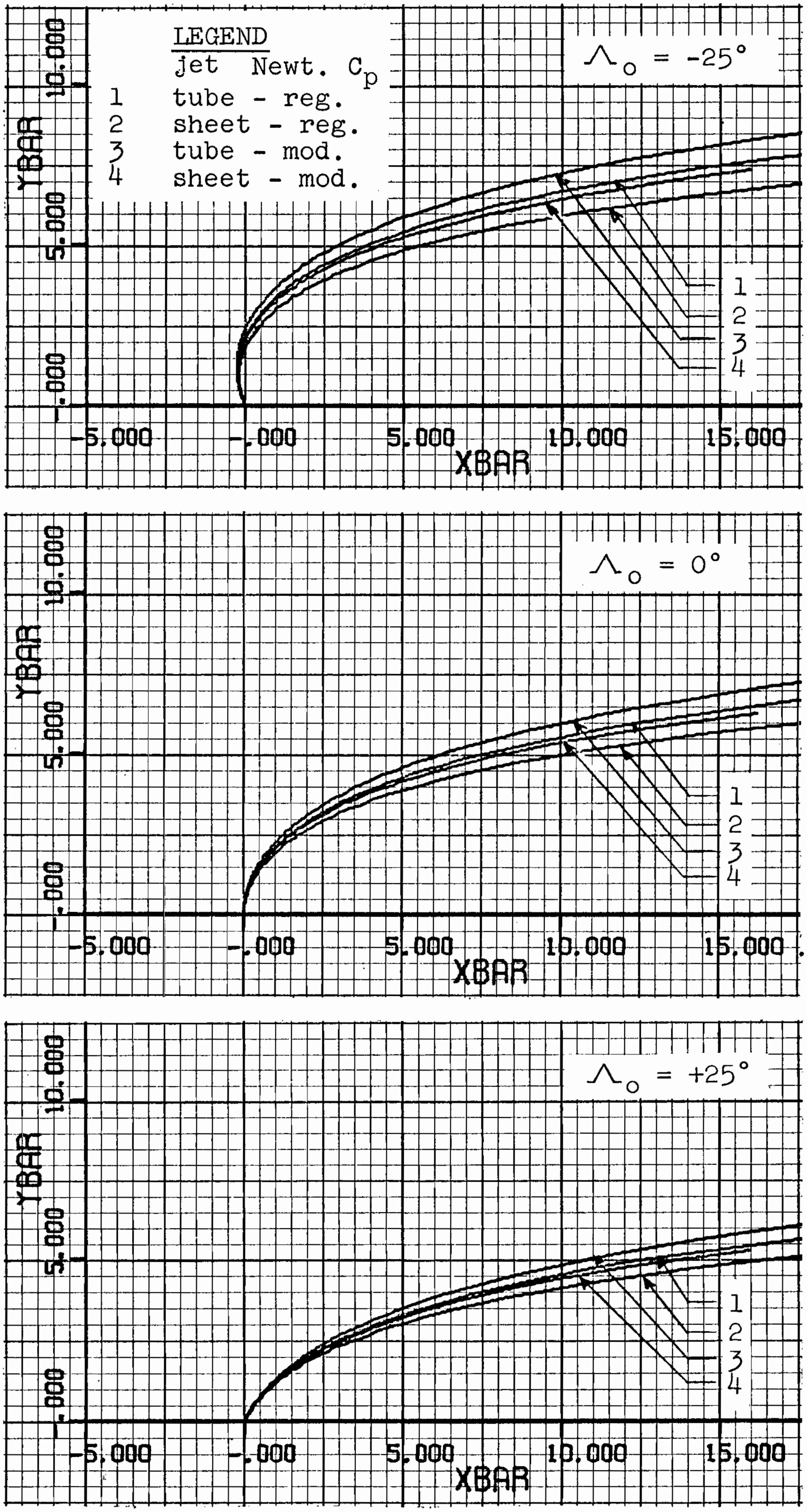

FIGURE 13 COMPUTER PLOT SHOWING COMPARISONS OF THE FOUR DIFFERENT INCOMPRESSIBLE JET CASES

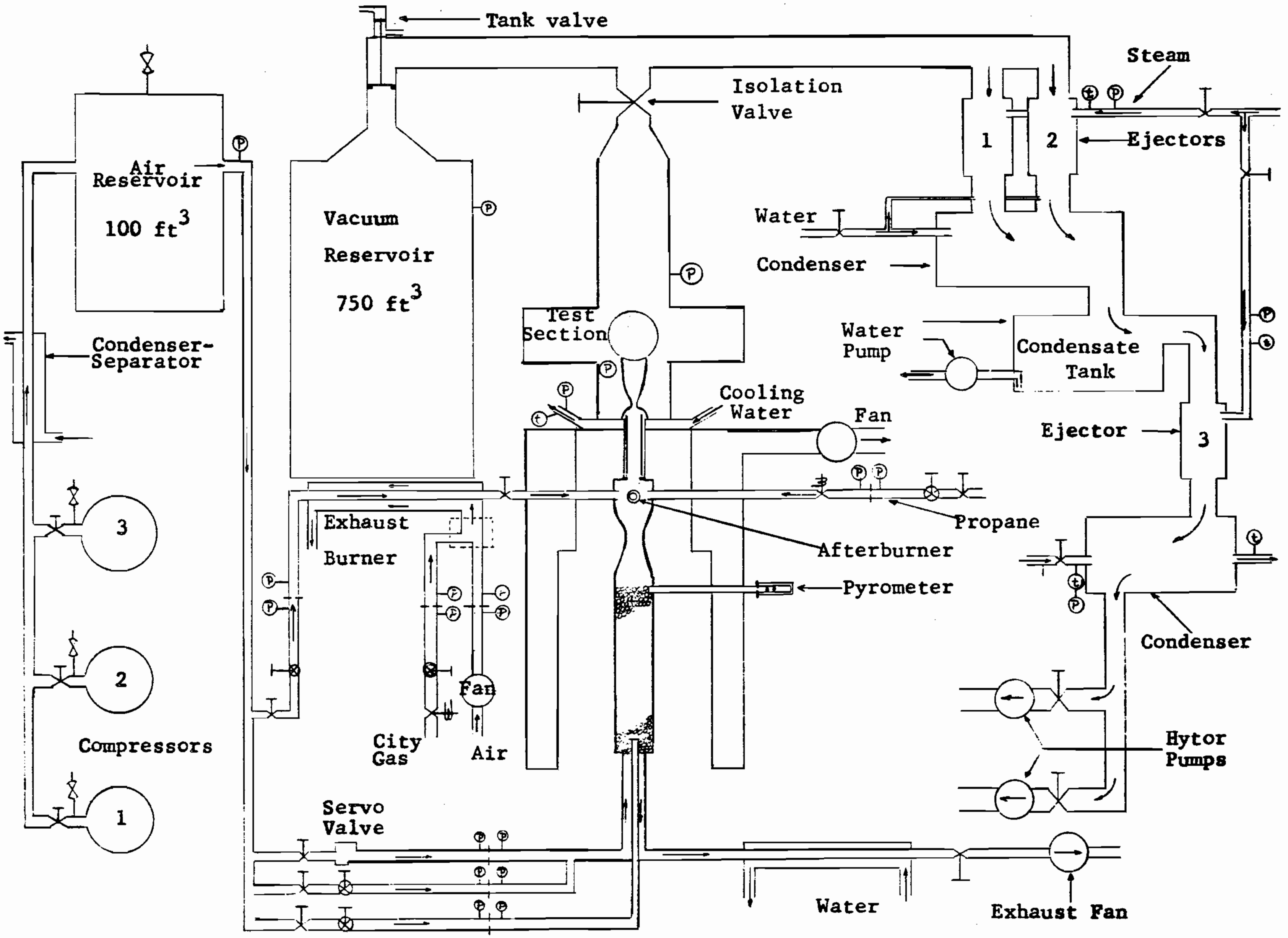

FIGURE 14 Schematic Diagram of Pebble Bed Heated Wind Tunnel and Vacuum System.

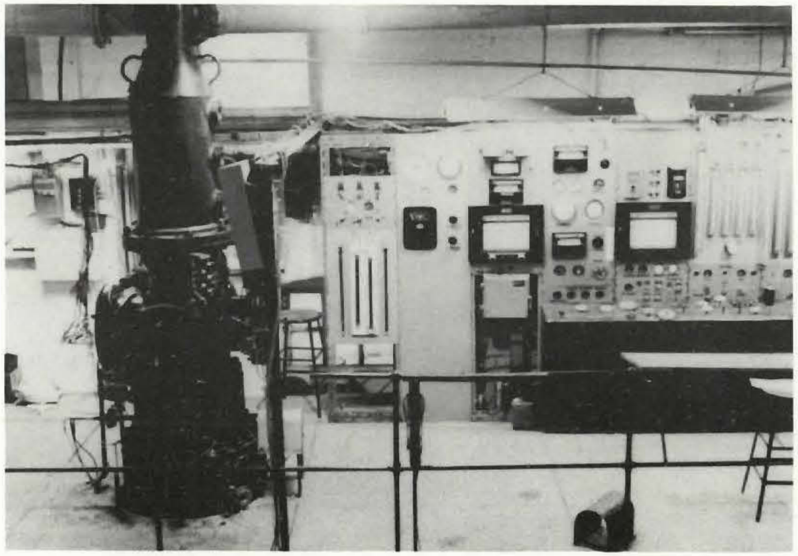

FIGURE 15 OVERALL VIEW OF TEST FACILITY

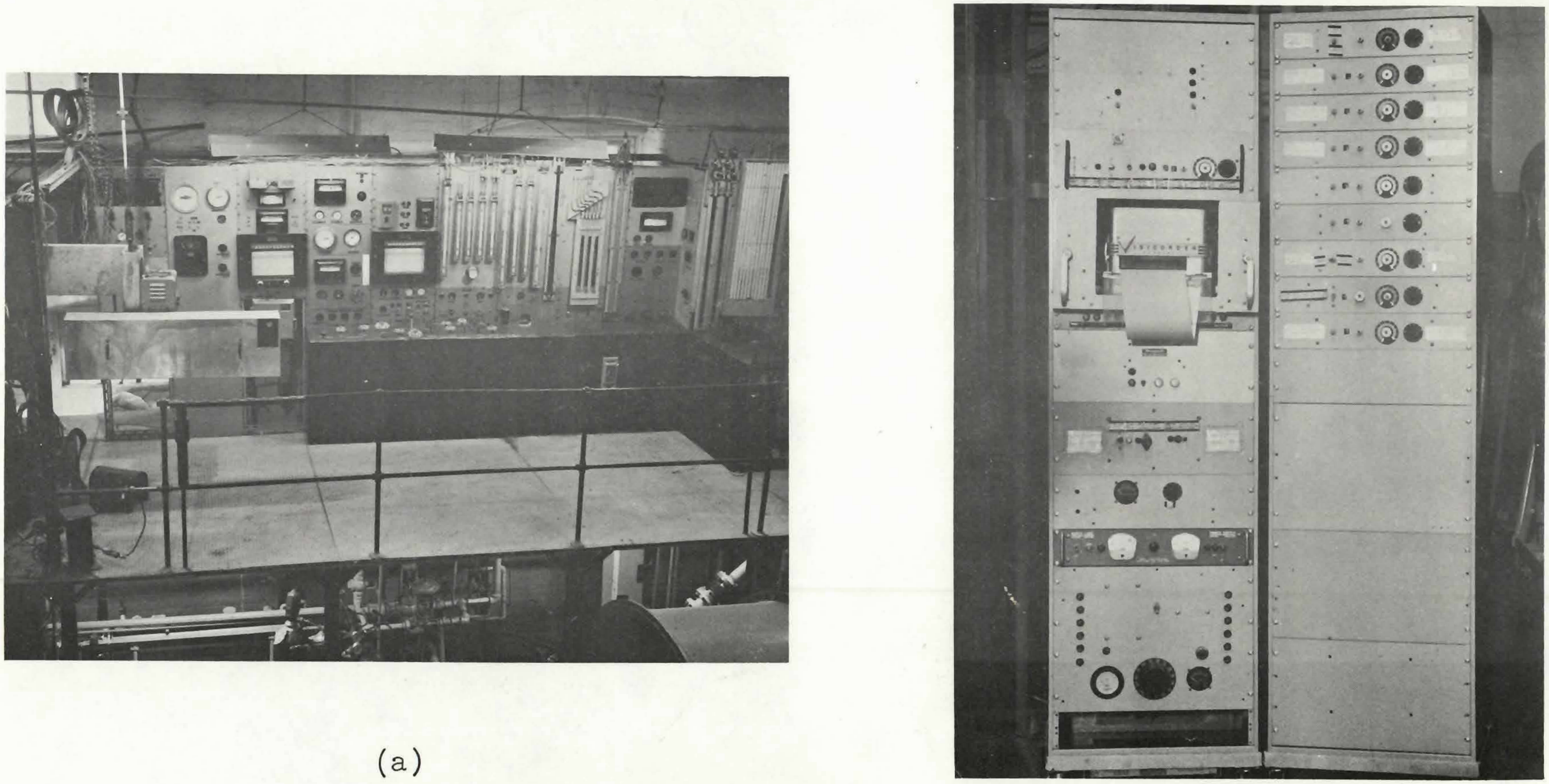

(a)

(b)

FIGURE 16 INSTRUMENTATION OF HOT TUNNEL

View (a) shows the instrumentation and controls required for running the tunnel. View (b) shows the test result recording instruments (Visicorder).

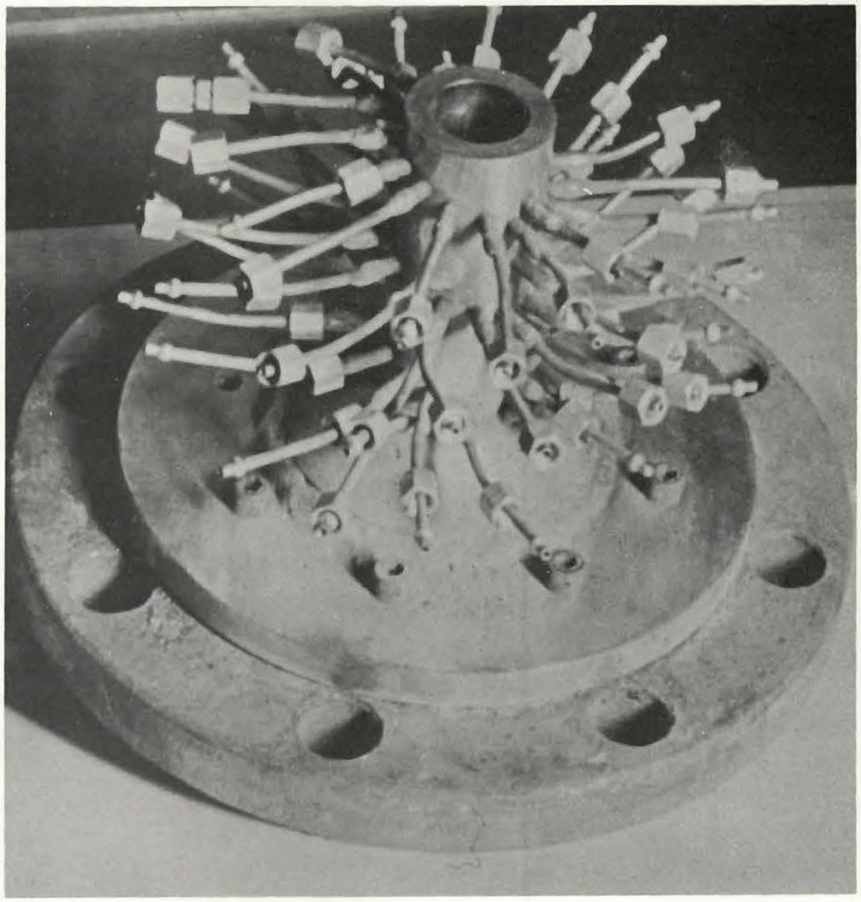

FIGURE 17 MACH 3 STAINLESS STEEL AXISYMMETRIC NOZZLE
(shown mounted on a flange)

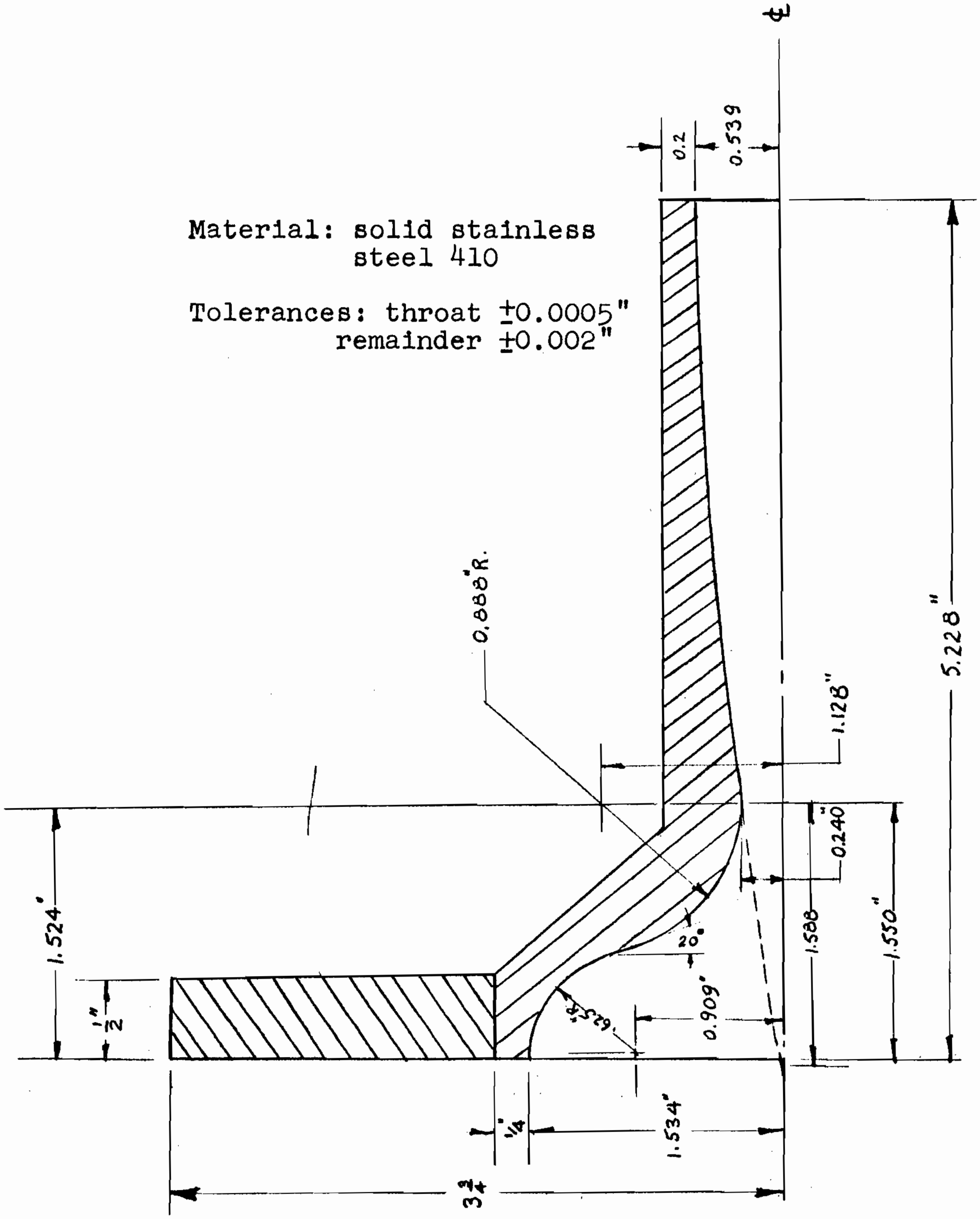

Material: solid stainless
steel 410

Tolerances: throat ±0.0005"
remainder ±0.002"

FIGURE 18 MACH 3 AXISYMMETRIC NOZZLE

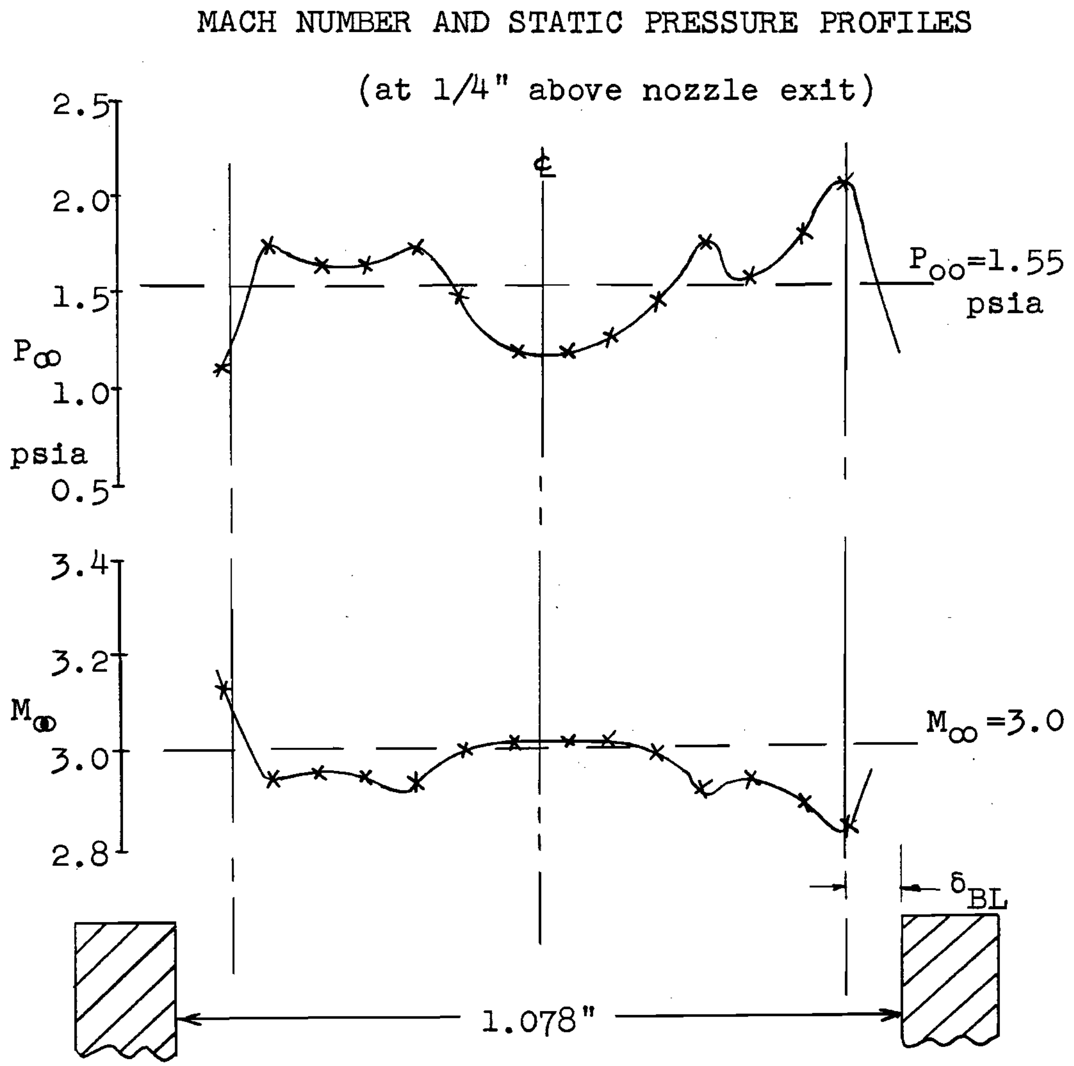
MACH NUMBER AND STATIC PRESSURE PROFILES

(at 1/4" above nozzle exit)

Nozzle: MACH 3 AXISYMMETRIC
Area Ratio = 5.04

$P_{t\infty}$ = 62 psia

with H_2-O_2 afterburner:

γ_∞ = 1.31 (Ref. 23)

$2600 < T_{t\infty} < 3000$°K

THEORETICAL CALCULATIONS

at nozzle exit: (Ref. 24)

δ_{BL} = 0.071 in.
$\delta_{1_{BL}}$ = 0.066 in.
$\delta_{2_{BL}}$ = 0.00058 in.

for M_∞ = 3.0 , γ_∞ = 1.31 ,

$P_{t\infty}$ = 62 psia , and $T_{t\infty}$ = 3000°K

P_∞ = 1.55 psia
T_∞ = 1250°K
m_∞ = 0.08 lb./sec.
V_∞ = 6750 ft./sec.
ρ_∞ = 0.00185 lb./ft.^{3}

FIGURE 19 SAMPLE NOZZLE CALIBRATION

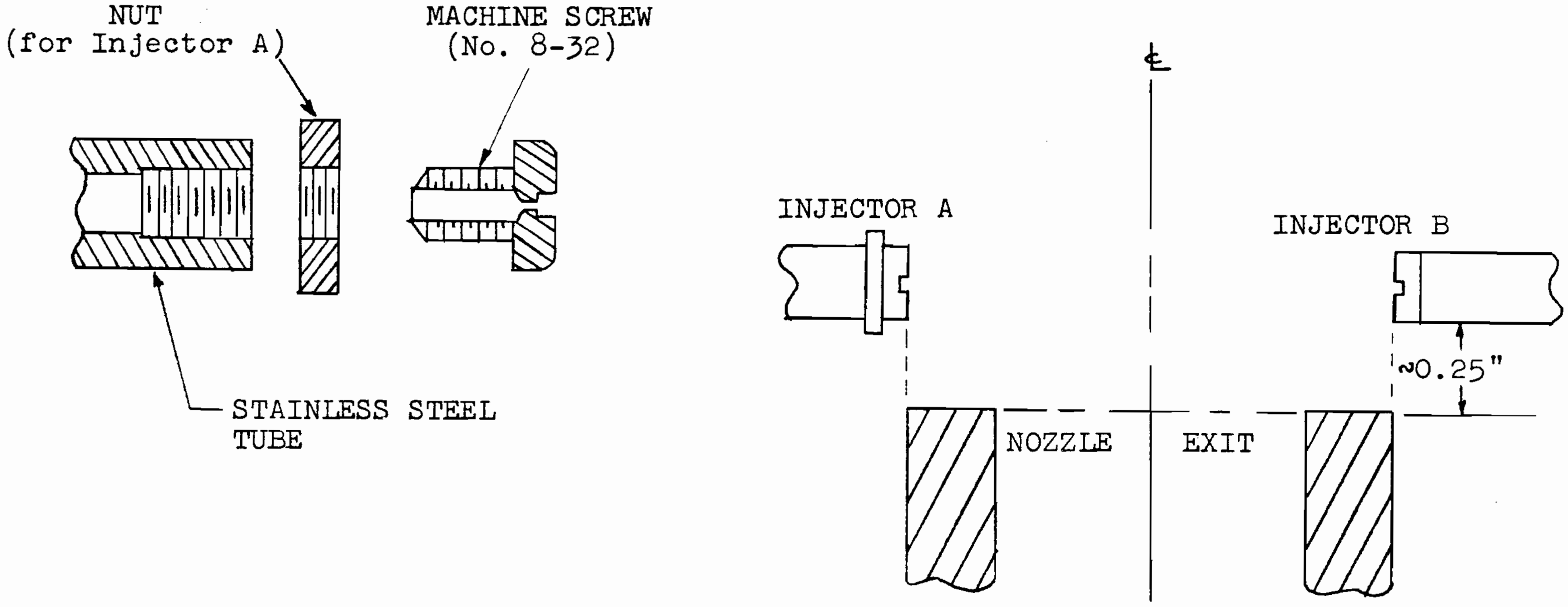

FIGURE 20 SKETCH OF INJECTORS AND INJECTOR SET-UP

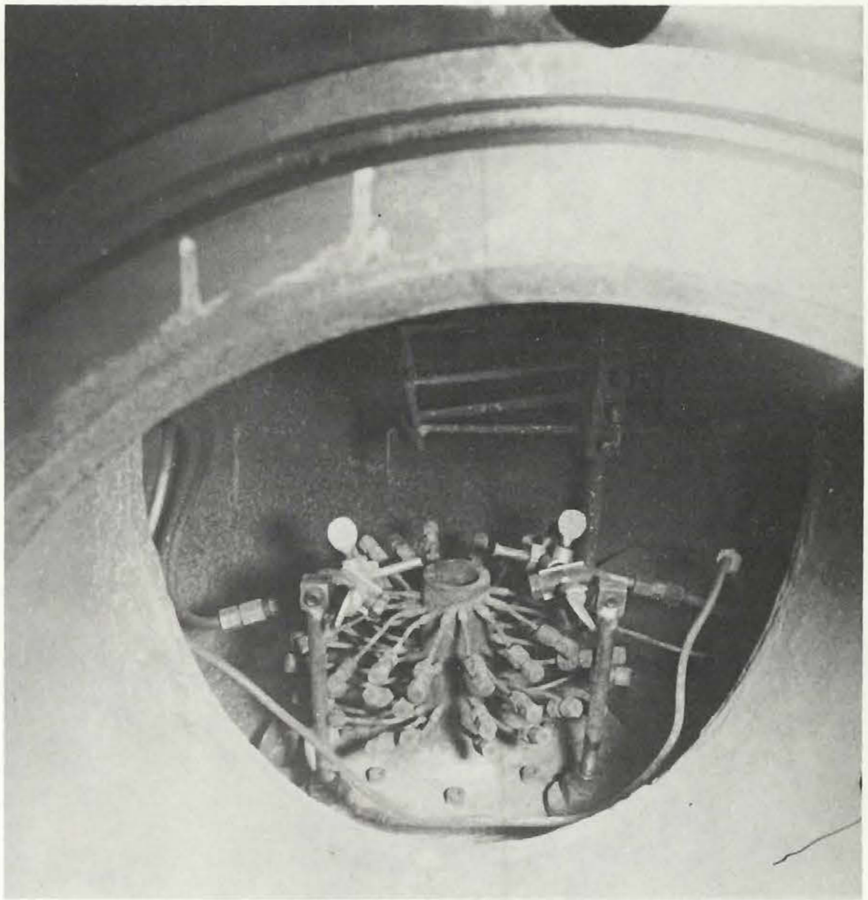

FIGURE 21 SET-UP IN HOT TUNNEL

Two water injectors are shown clamped at the sides of a three-dimensional, Mach 3 nozzle.

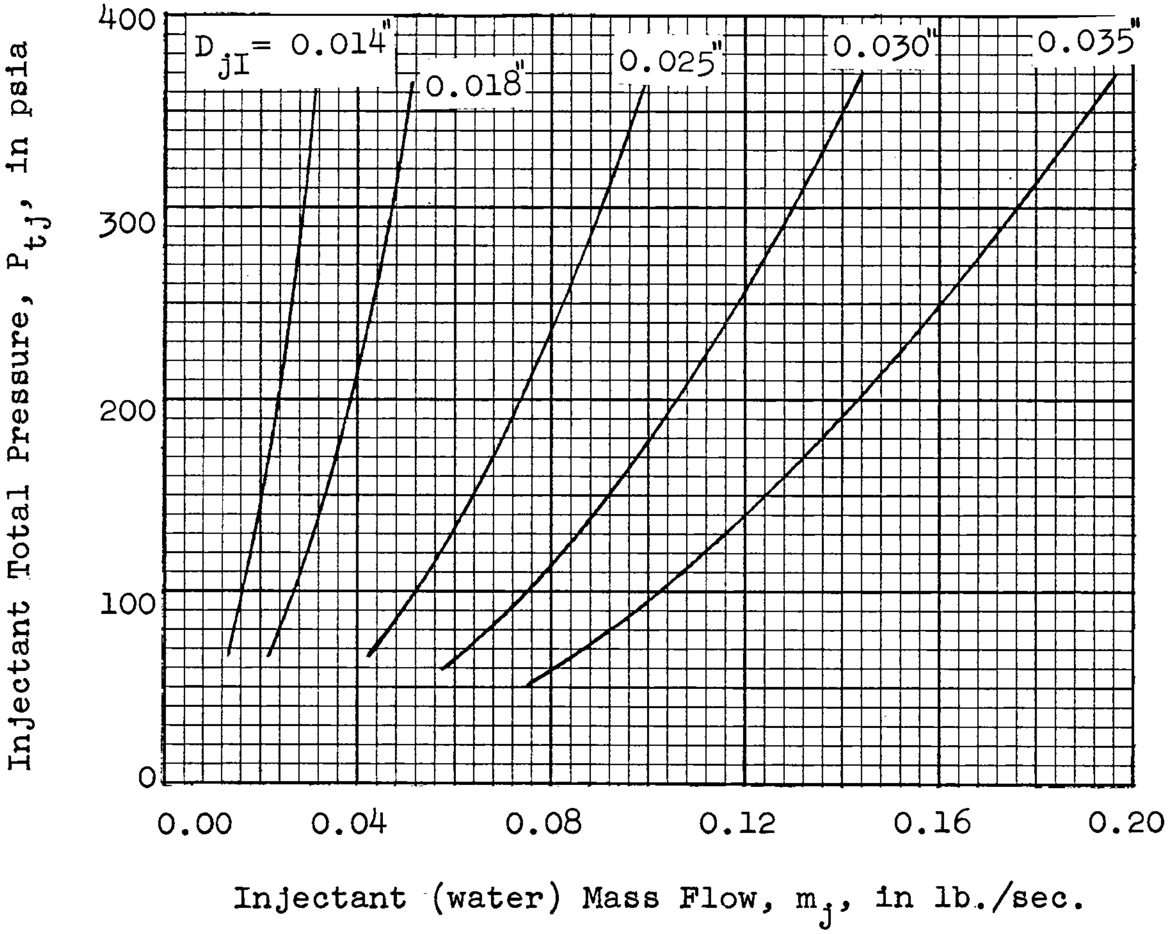

FIGURE 22 INJECTANT (WATER) MASS FLOW VERSUS P_{tj} FOR VARIOUS D_{jI}

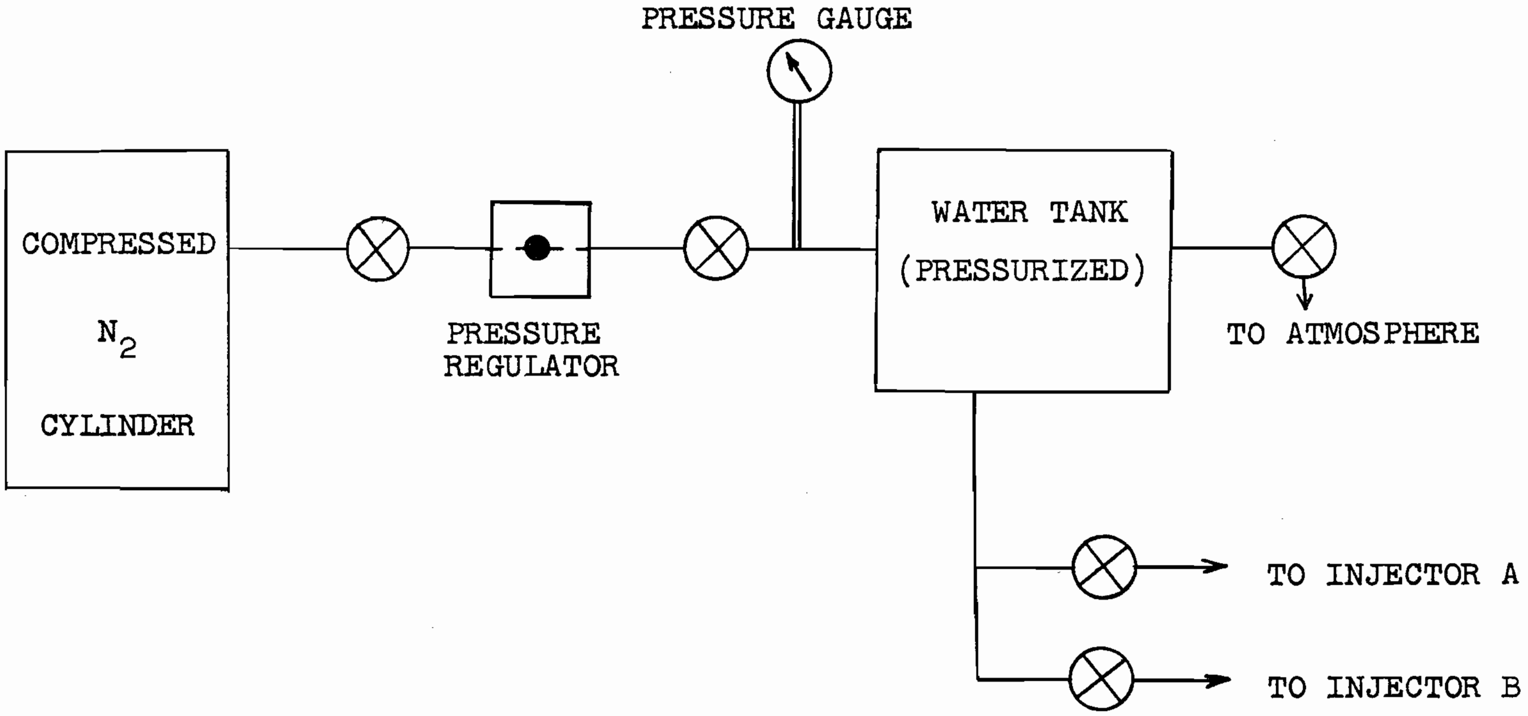

FIGURE 23 SCHEMATIC OF WATER FLOW METERING SET-UP

$D_{jI} = 0.018$ in. $\Lambda_o = -28°$

$D_{jI} = 0.030$ in. $\Lambda_o = 0°$

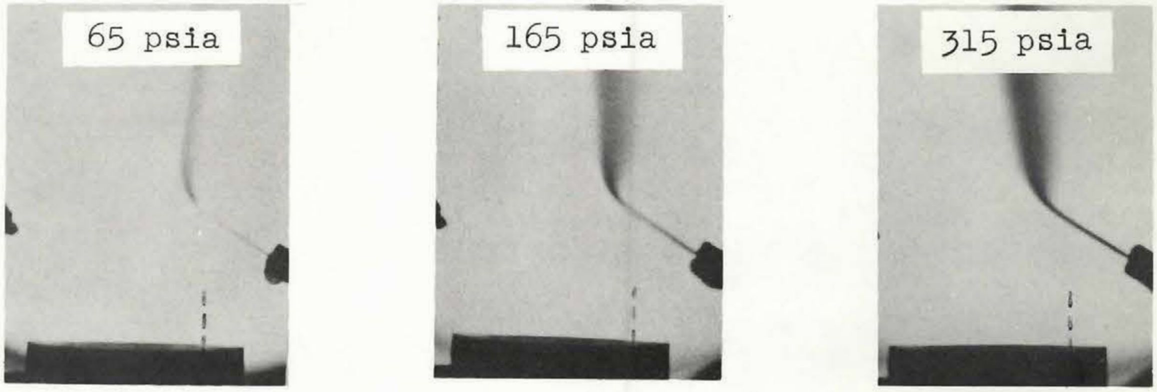

$D_{jI} = 0.025$ in. $\Lambda_o = +31°$

FIGURE 24 WATER INJECTION PHOTOGRAPHS FOR P_{tj} VARIATION

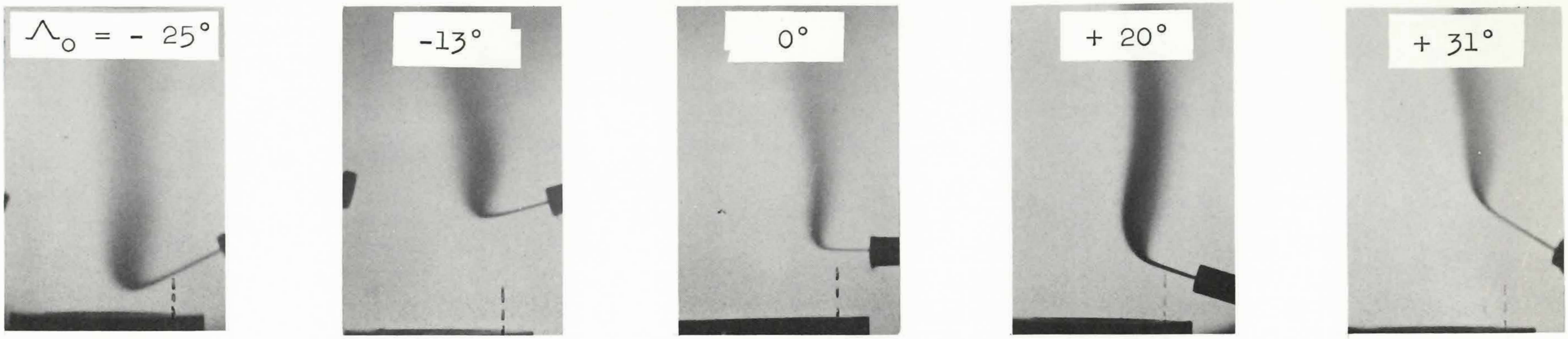

P_{tj} = 215 psia D_{jI} = 0.025 in.

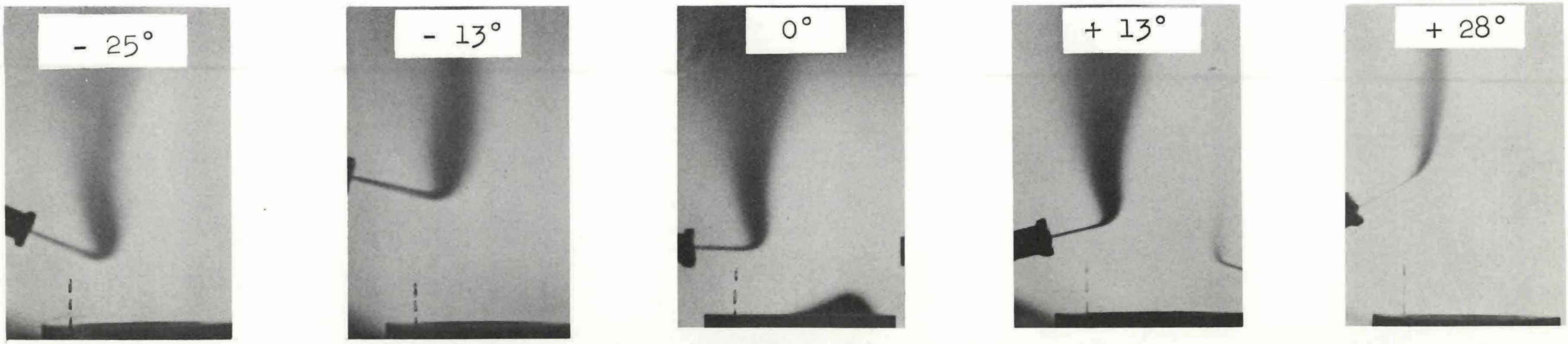

P_{tj} = 90 psia D_{jI} = 0.025 in.

FIGURE 25 WATER INJECTION PHOTOGRAPHS FOR Λ_o VARIATION

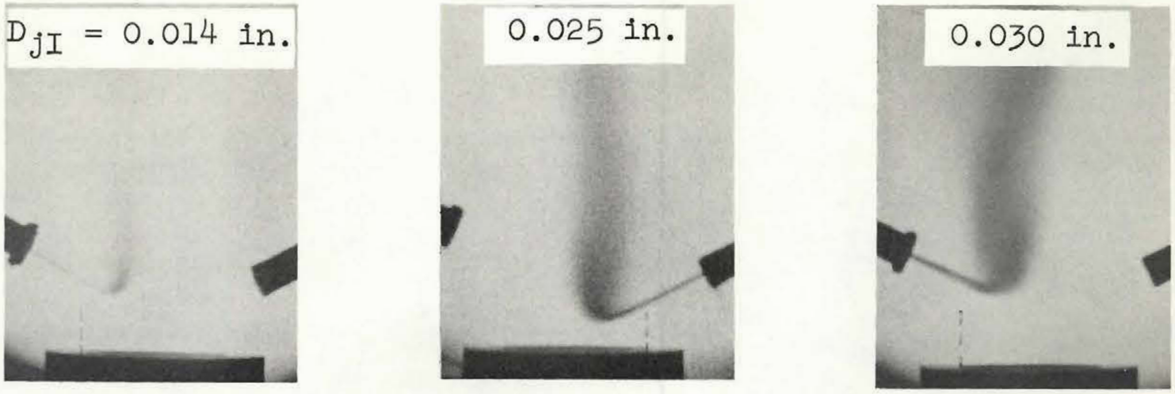

P_{tj} = 215 psia Λ_o = -25°

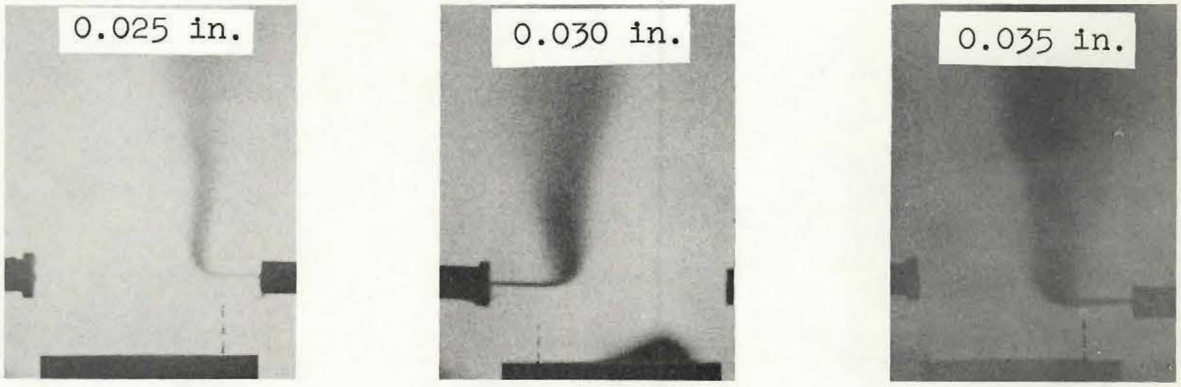

P_{tj} = 165 psia Λ_o = 0°

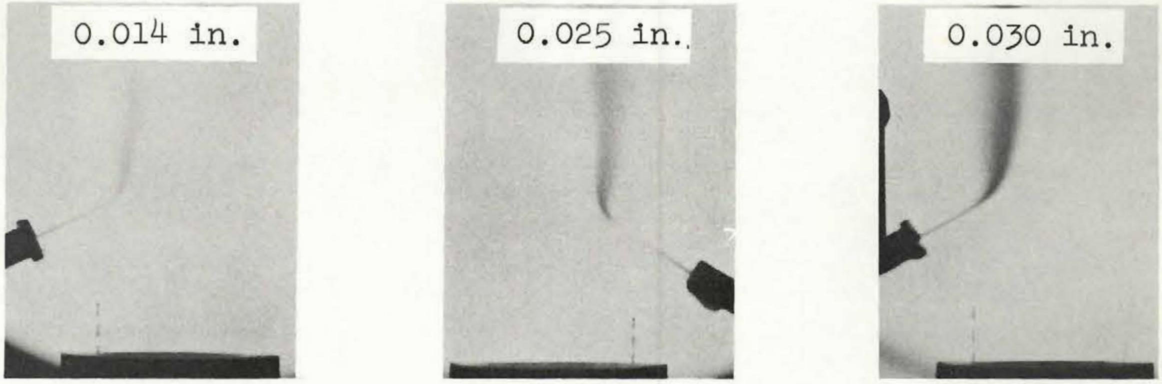

P_{tj} = 115 psia Λ_o = + 28°

FIGURE 26 WATER INJECTION PHOTOGRAPHS FOR D_{jI} VARIATION

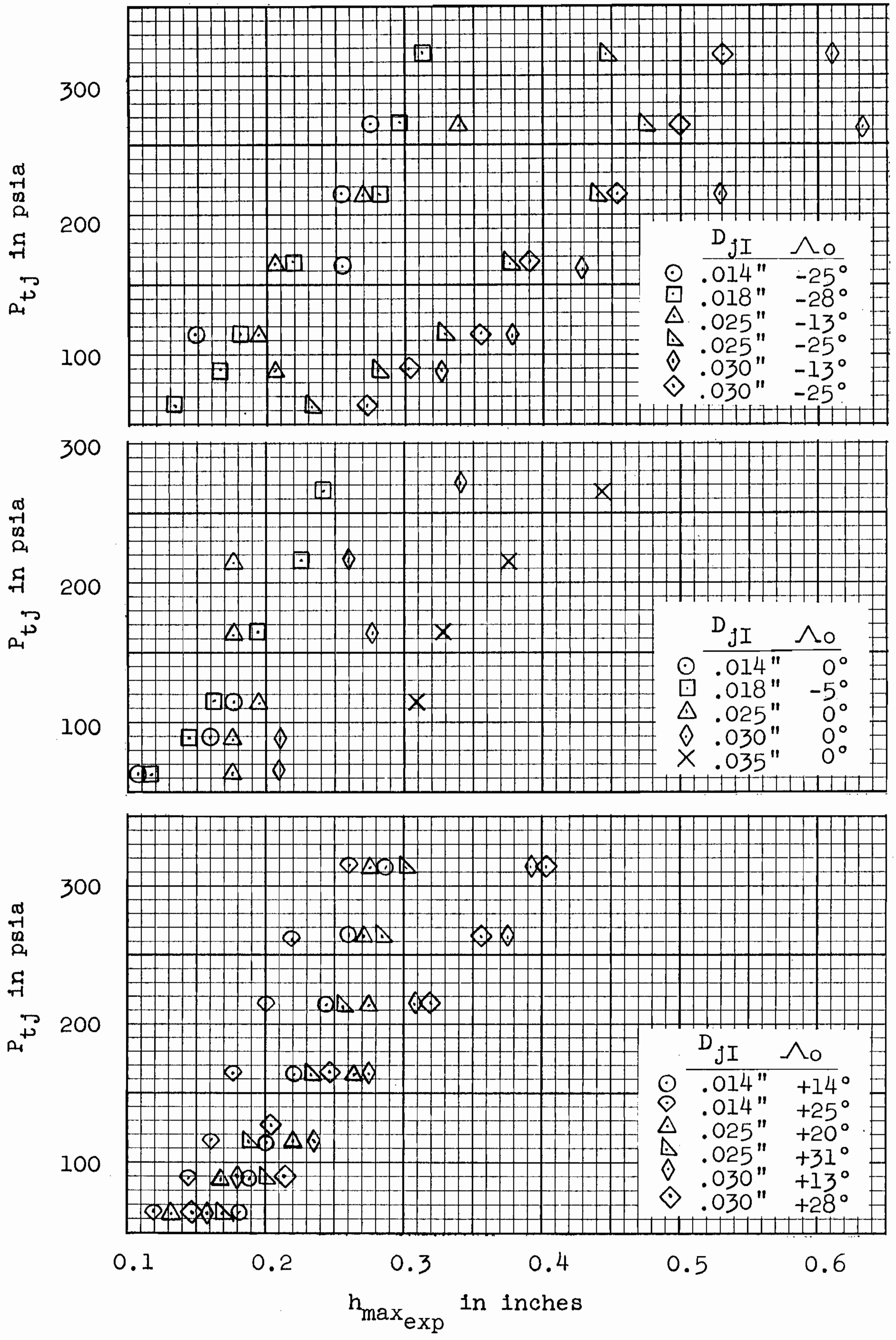

FIGURE 27 MAXIMUM PENETRATION VERSUS P_{tj} FOR VARIOUS D_{jI}'S AND Λ_o'S

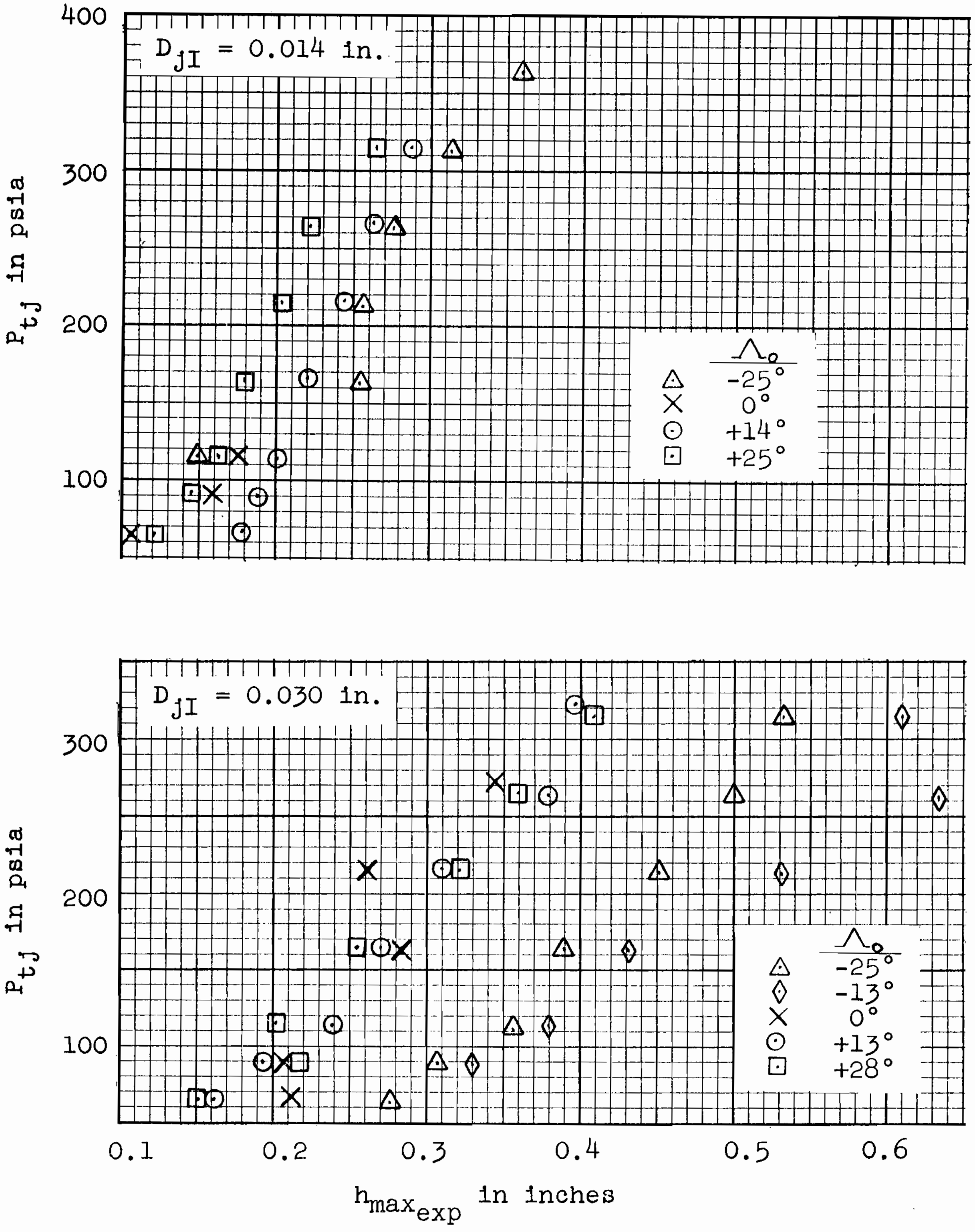

FIGURE 28 MAXIMUM PENETRATION VERSUS P_{tj} FOR A RANGE OF Λ_o'S

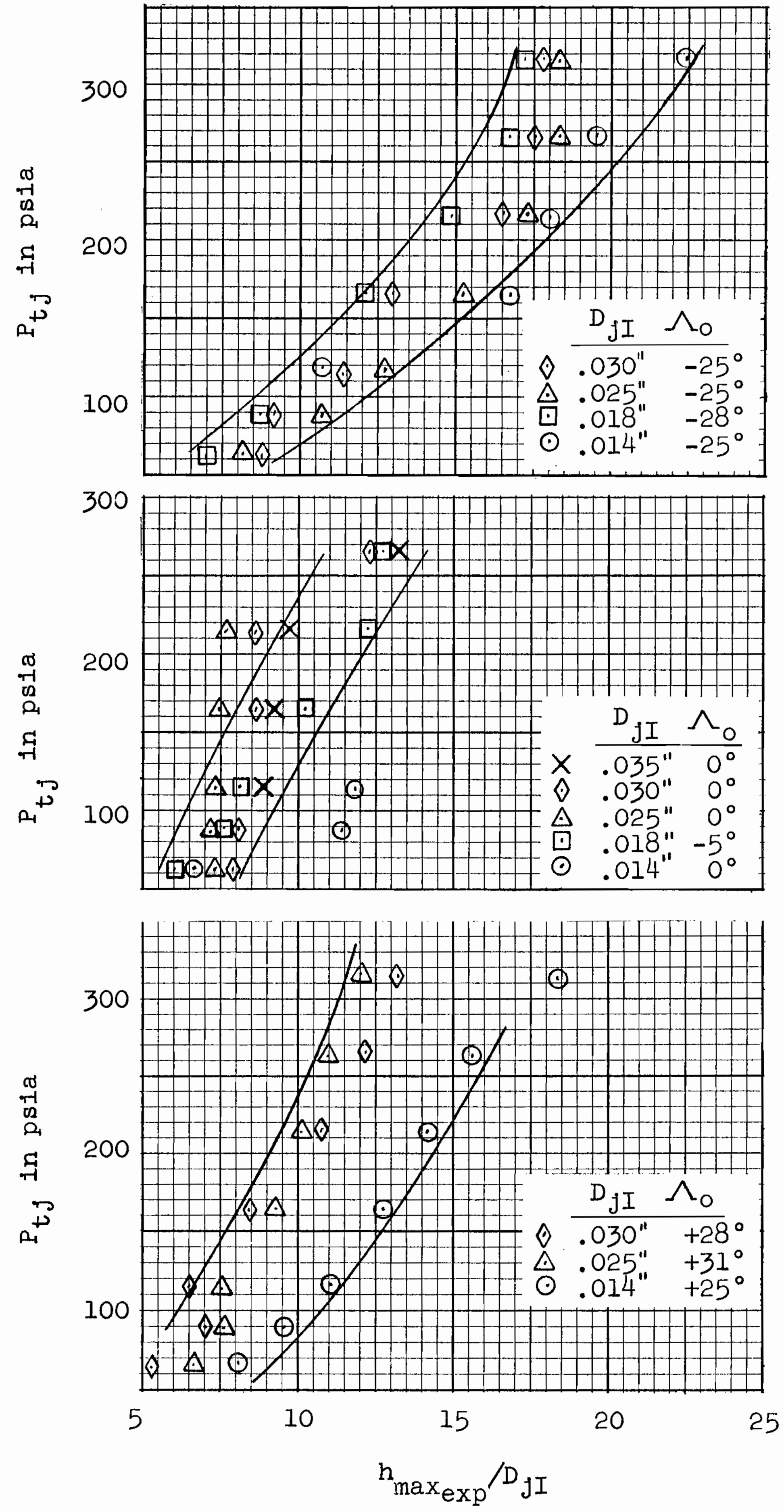

FIGURE 29 RELATIVE MAXIMUM PENETRATION VERSUS P_{tj}

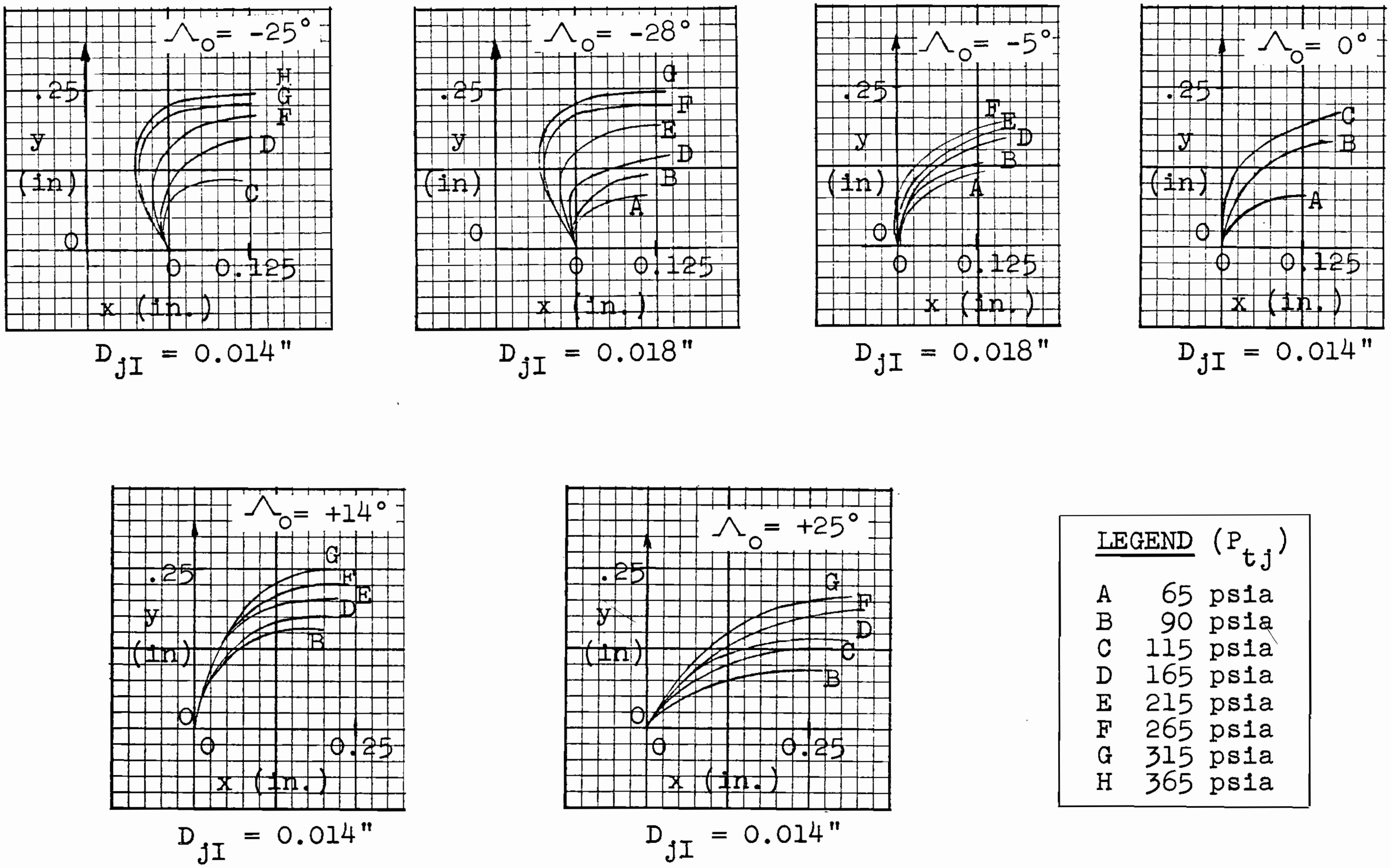

D_{jI} = 0.014" D_{jI} = 0.018" D_{jI} = 0.018" D_{jI} = 0.014"

D_{jI} = 0.014" D_{jI} = 0.014"

LEGEND (P_{tj})

A	65 psia
B	90 psia
C	115 psia
D	165 psia
E	215 psia
F	265 psia
G	315 psia
H	365 psia

FIGURE 30 EXPERIMENTAL WATER INJECTANT CENTRELINE PATHS

(For D_{jI} = 0.014 in. and 0.018 in.)

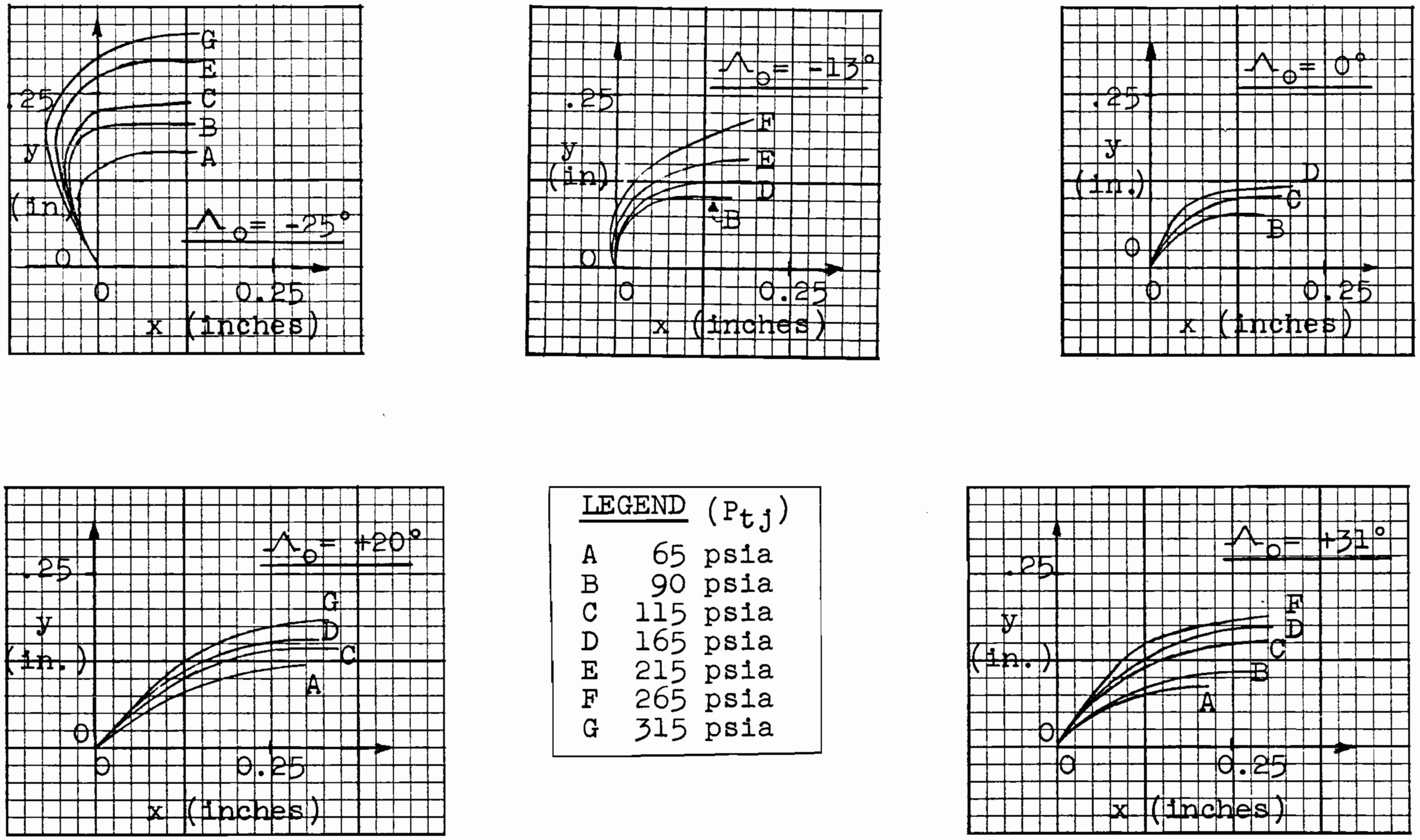

LEGEND (P_{tj})

A	65 psia
B	90 psia
C	115 psia
D	165 psia
E	215 psia
F	265 psia
G	315 psia

FIGURE 31 EXPERIMENTAL WATER INJECTANT CENTRELINE PATHS
(For D_{jI} = 0.025 in.)

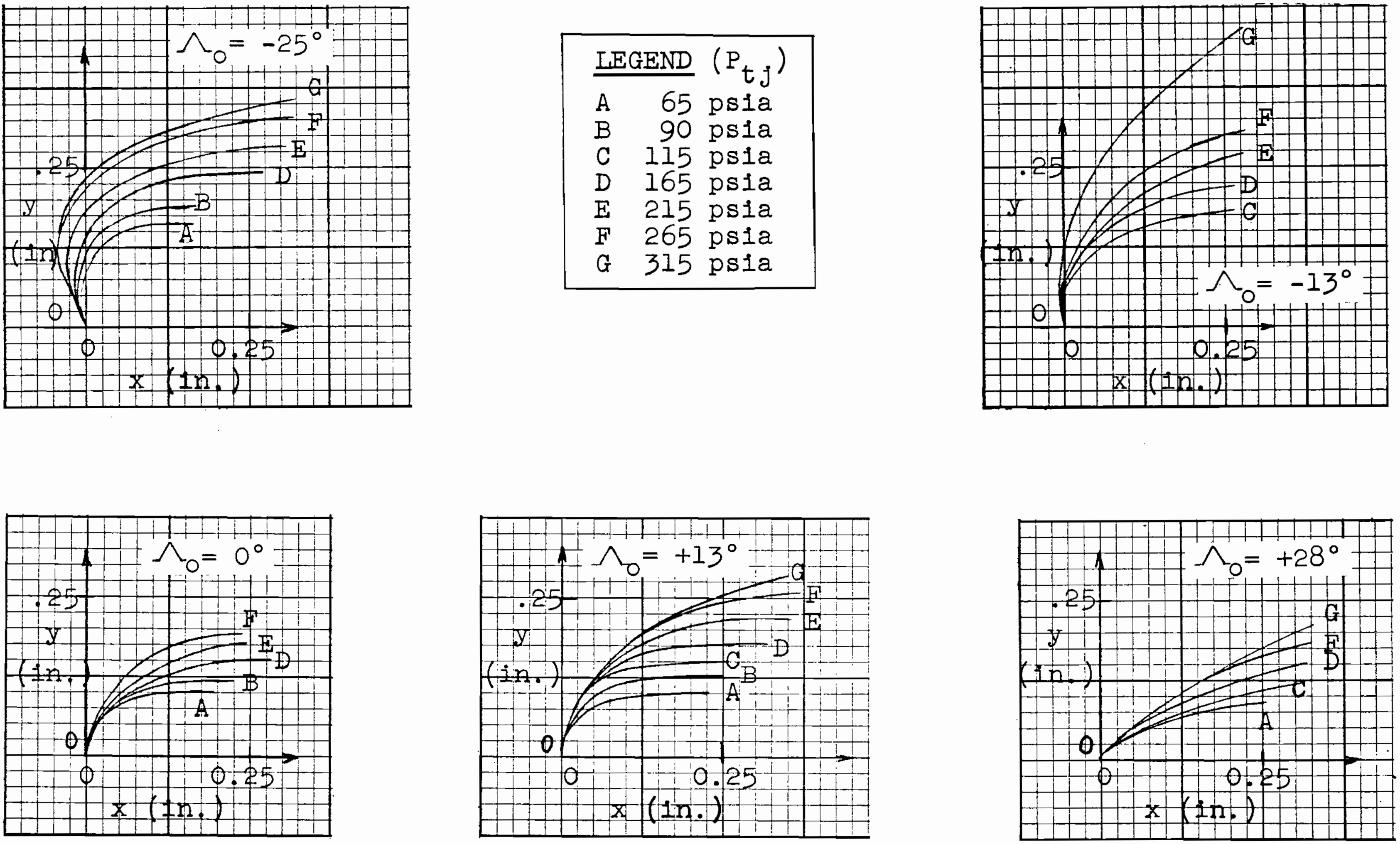

FIGURE 32 EXPERIMENTAL WATER INJECTANT CENTRELINE PATHS

(For D_{jI} = 0.030 in.)

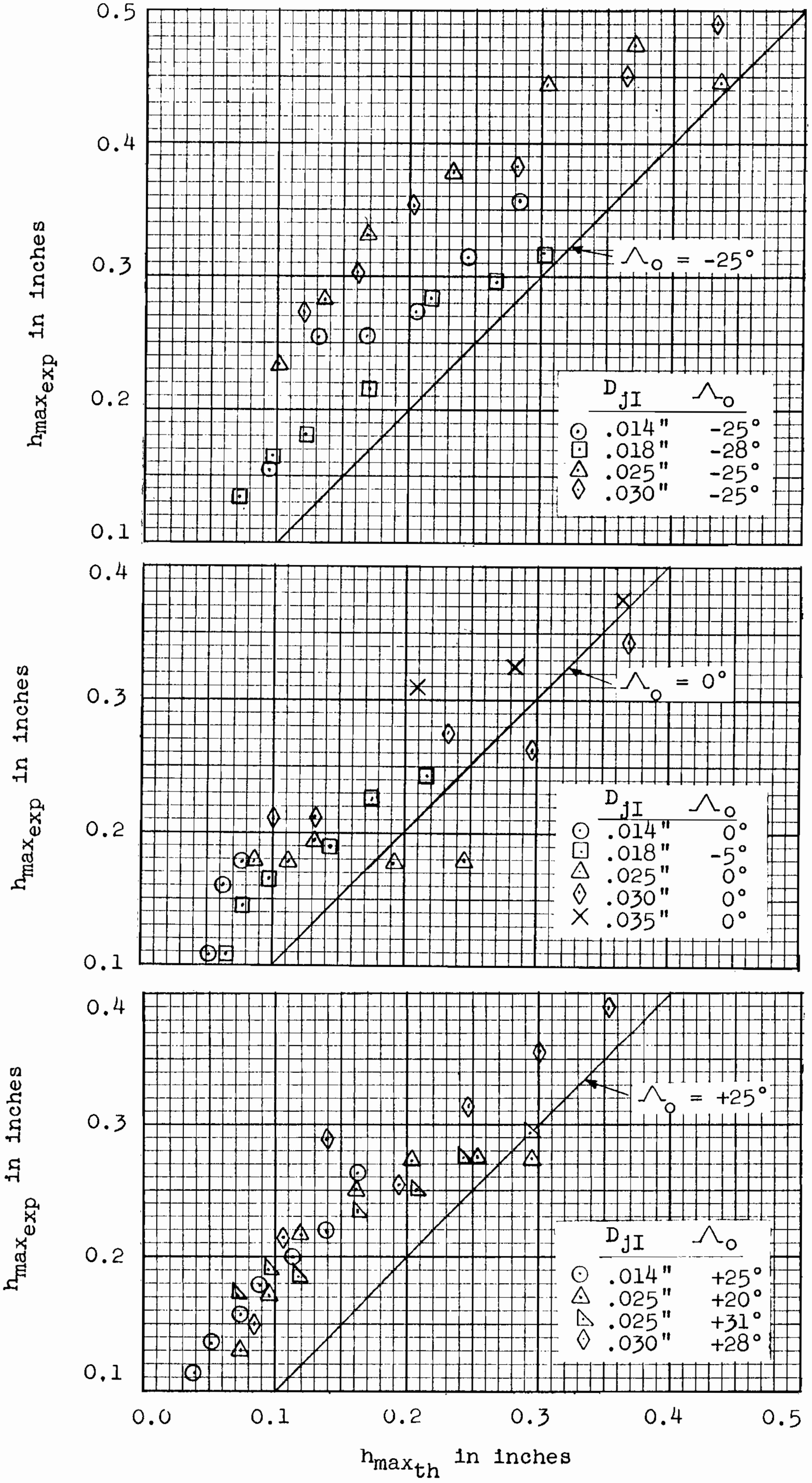

FIGURE 33 THEORETICAL MAXIMUM PENETRATION VERSUS EXPERIMENTAL MAXIMUM PENETRATION

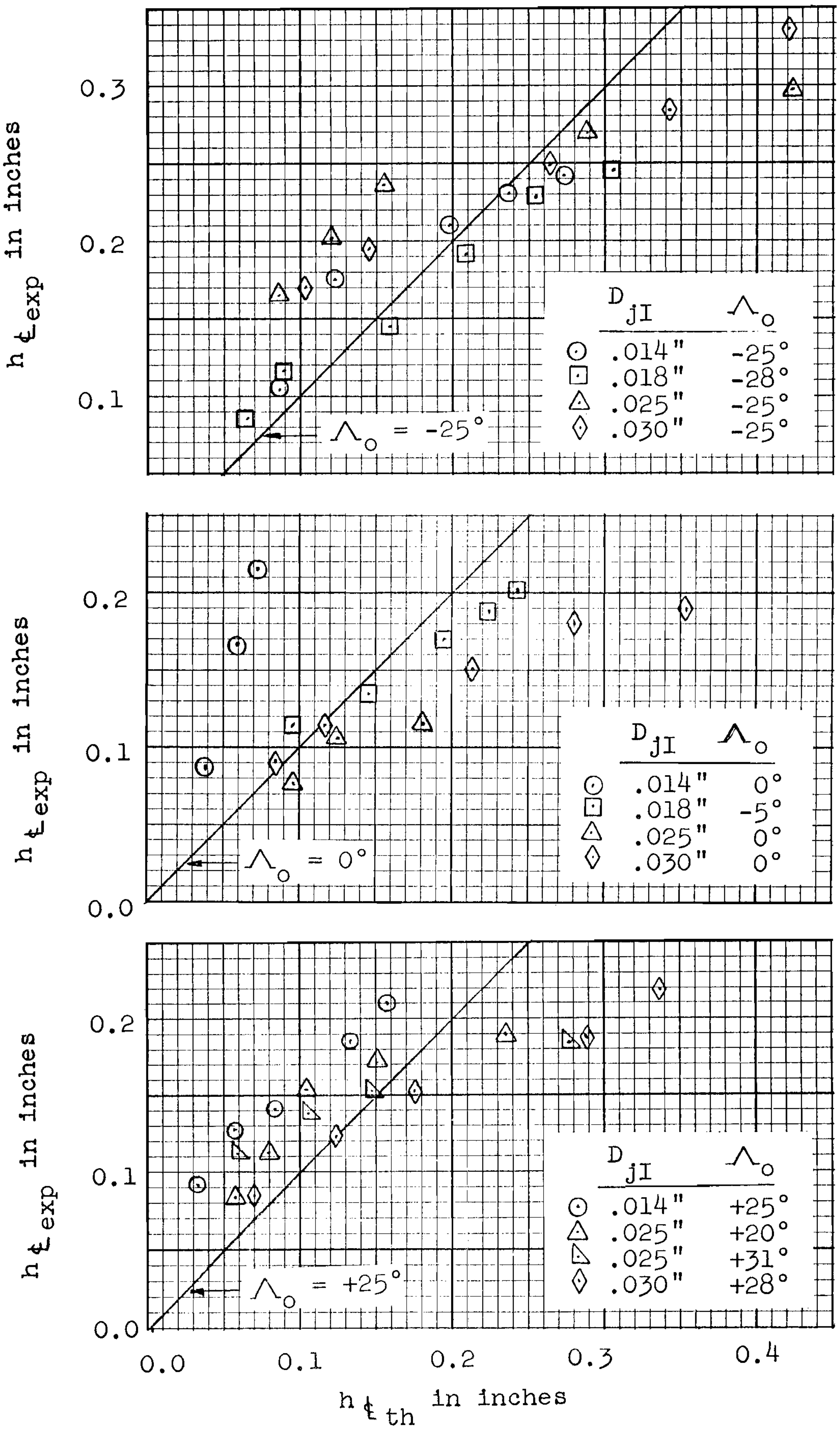

FIGURE 34 THEORETICAL CENTRELINE PENETRATION VERSUS EXPERIMENTAL CENTRELINE PENETRATION

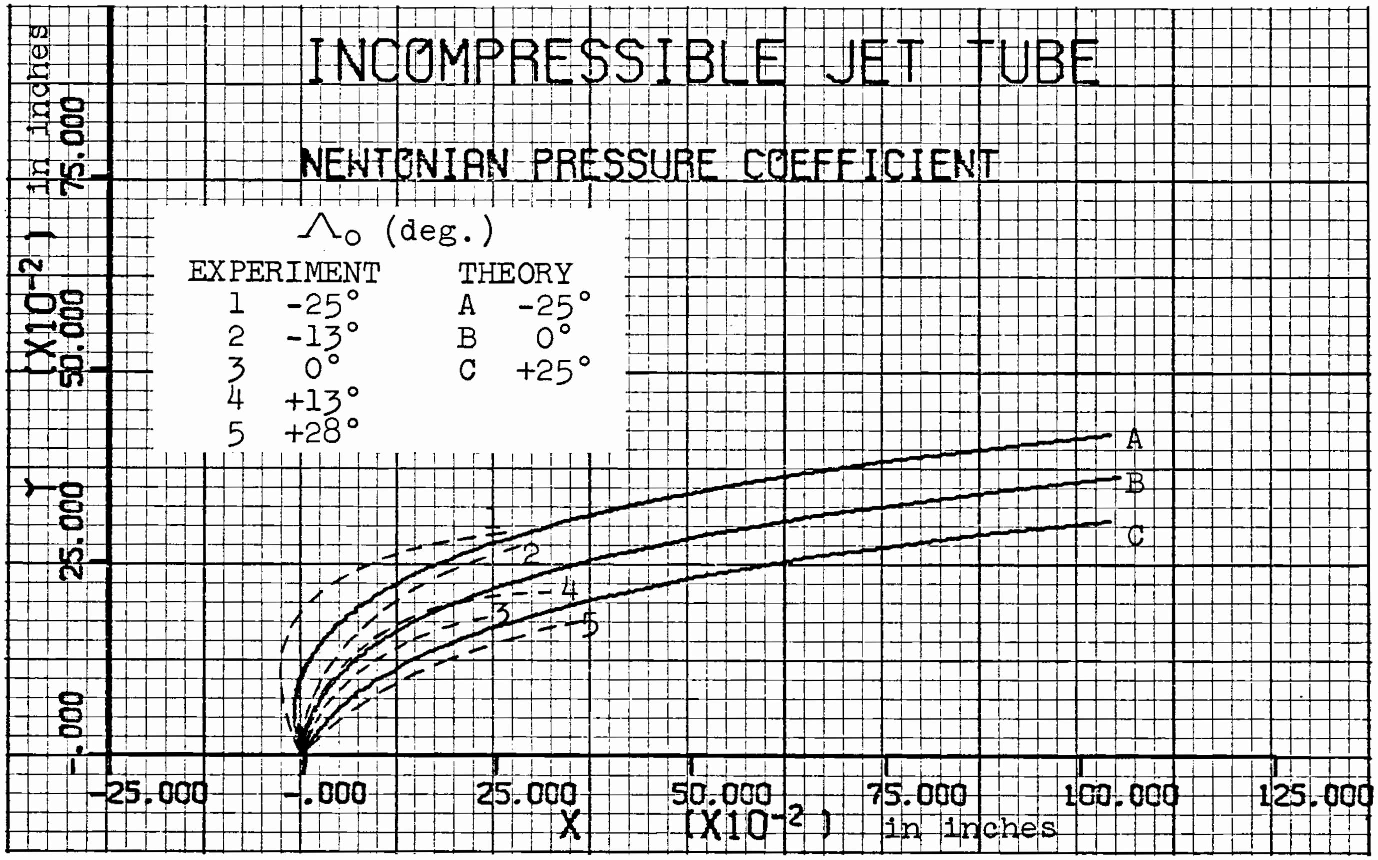

FIGURE 35a JET CENTRELINE PATH COMPARISON OF EXPERIMENT AND THEORY FOR A RANGE OF Λ_o'S (D_{jI} = 0.030 in., P_{tj} = 215 psia)

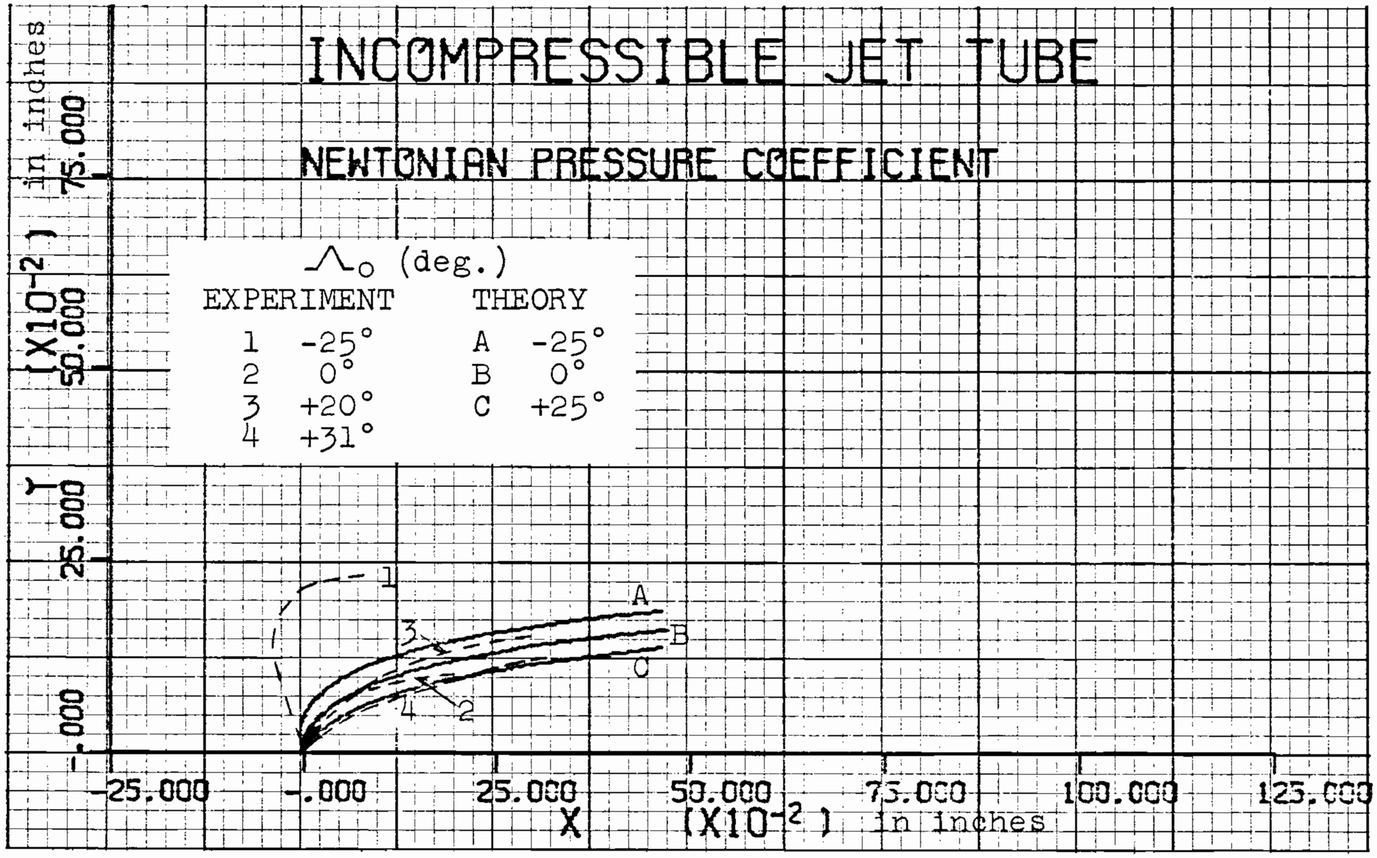

FIGURE 35b JET CENTRELINE PATH COMPARISON OF EXPERIMENT AND THEORY FOR A RANGE OF Λ_o'S ($D_{jI} = 0.025$ in., $P_{tj} = 115$ psia)

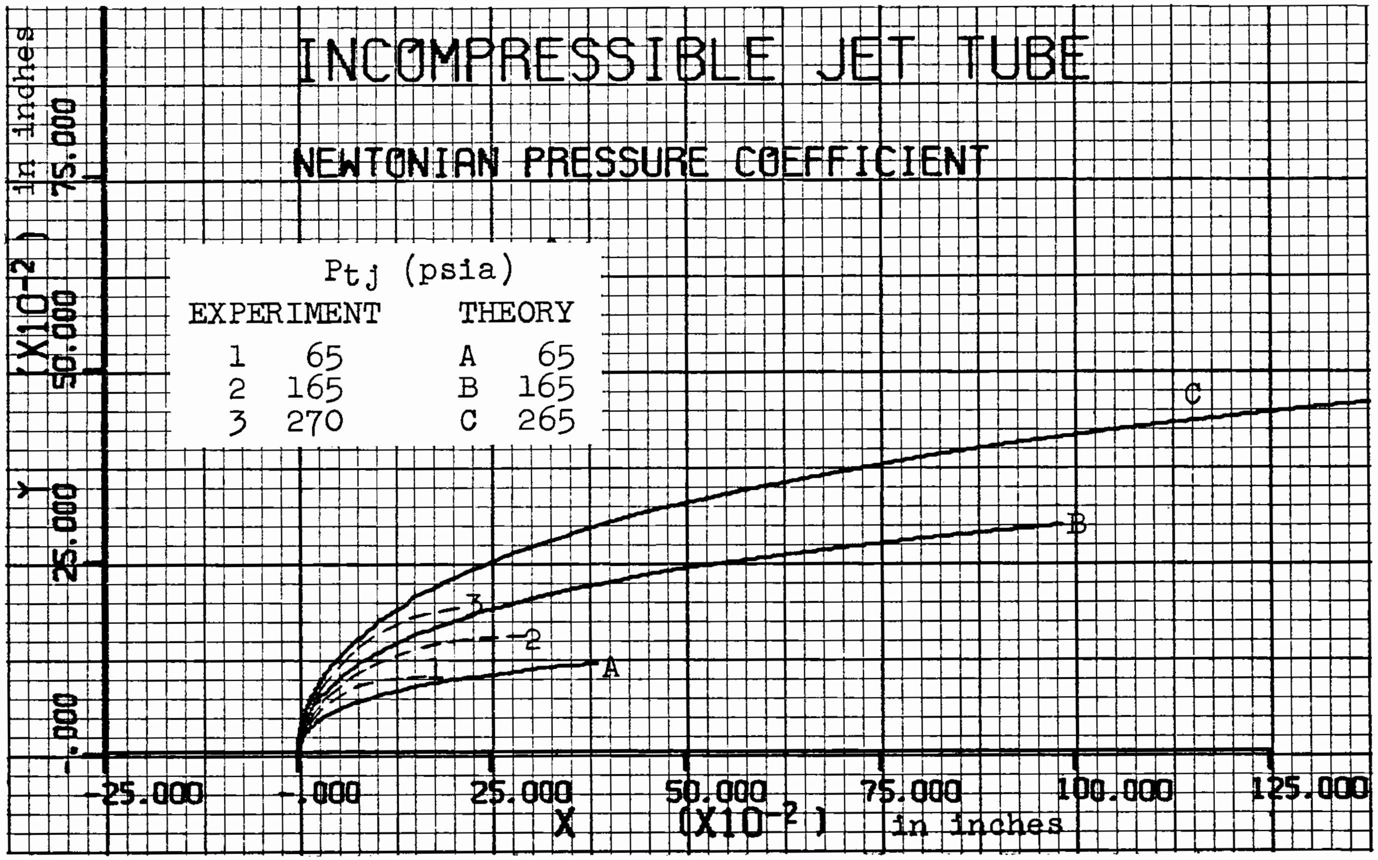

FIGURE 36a JET CENTRELINE PATH COMPARISON OF EXPERIMENT AND THEORY FOR A RANGE OF P_{tj}'S (D_{jI} = 0.030 in., Λ_o = 0°)

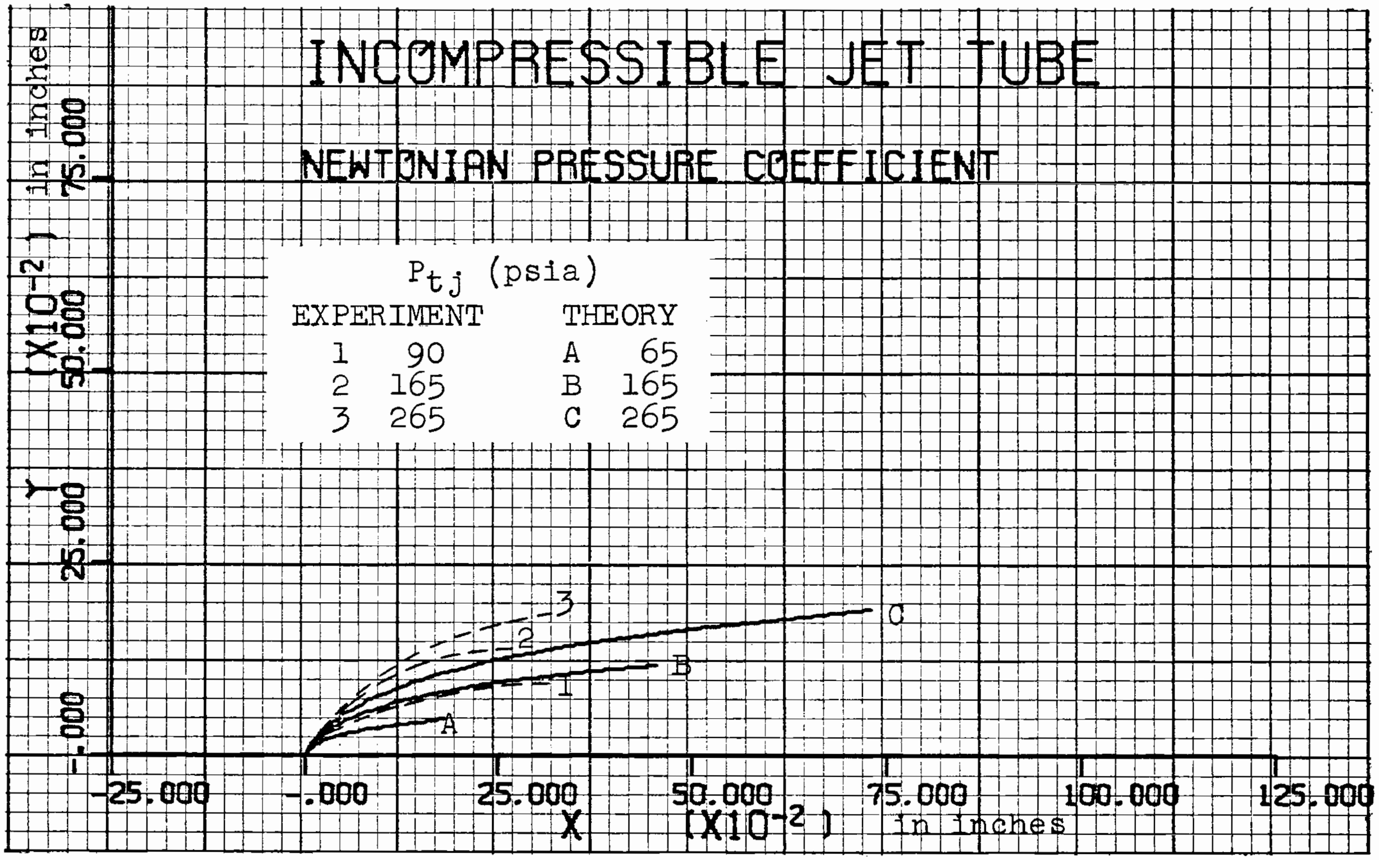

FIGURE 36b JET CENTRELINE PATH COMPARISON OF EXPERIMENT AND THEORY FOR A RANGE OF P_{tj}'S (D_{jI} = 0.014 in., Λ_o = +25°)

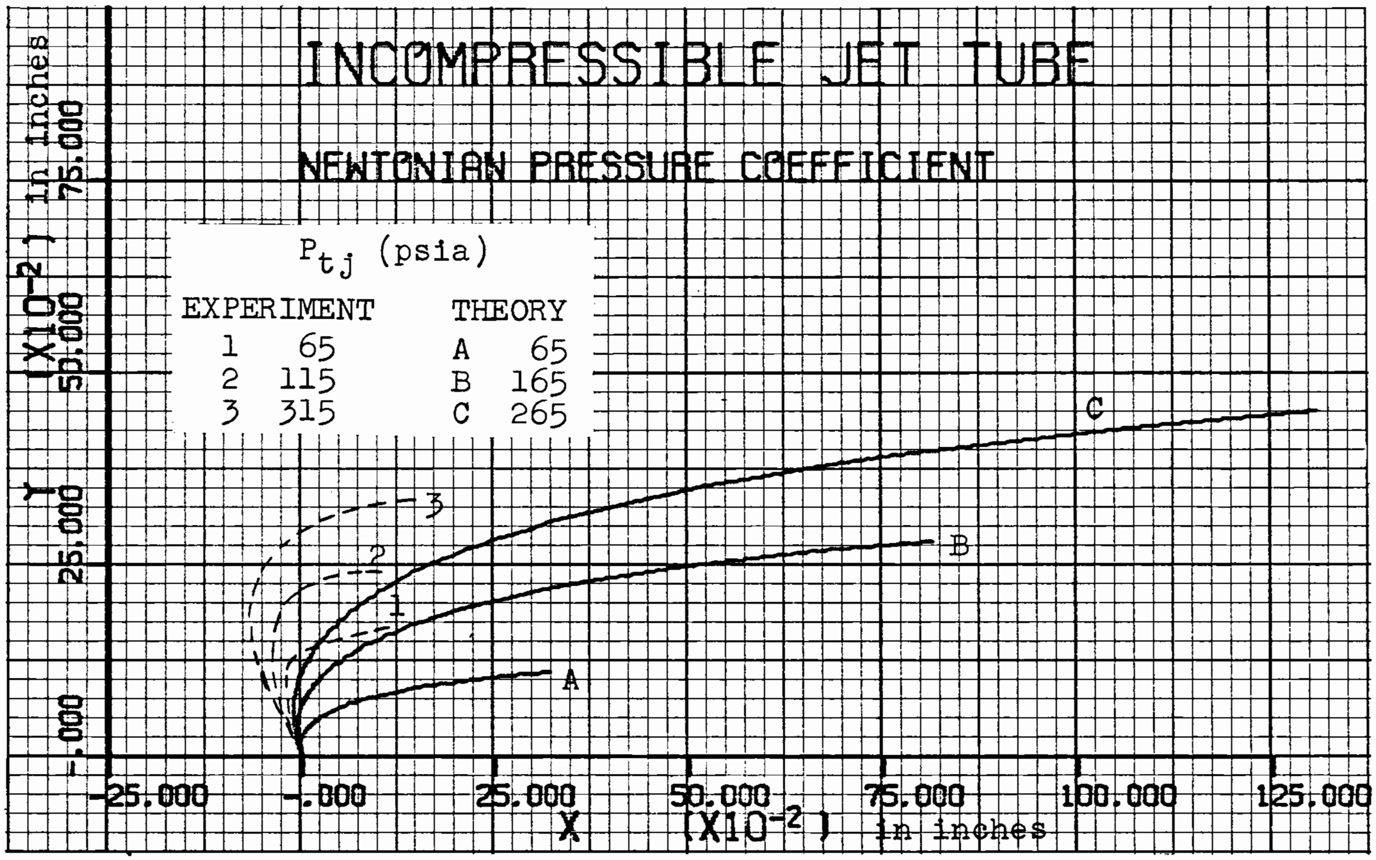

FIGURE 36c JET CENTRELINE PATH COMPARISON OF EXPERIMENT AND THEORY FOR A RANGE OF P_{tj}'S (D_{jI} = 0.025 in., Λ_o= -25°)

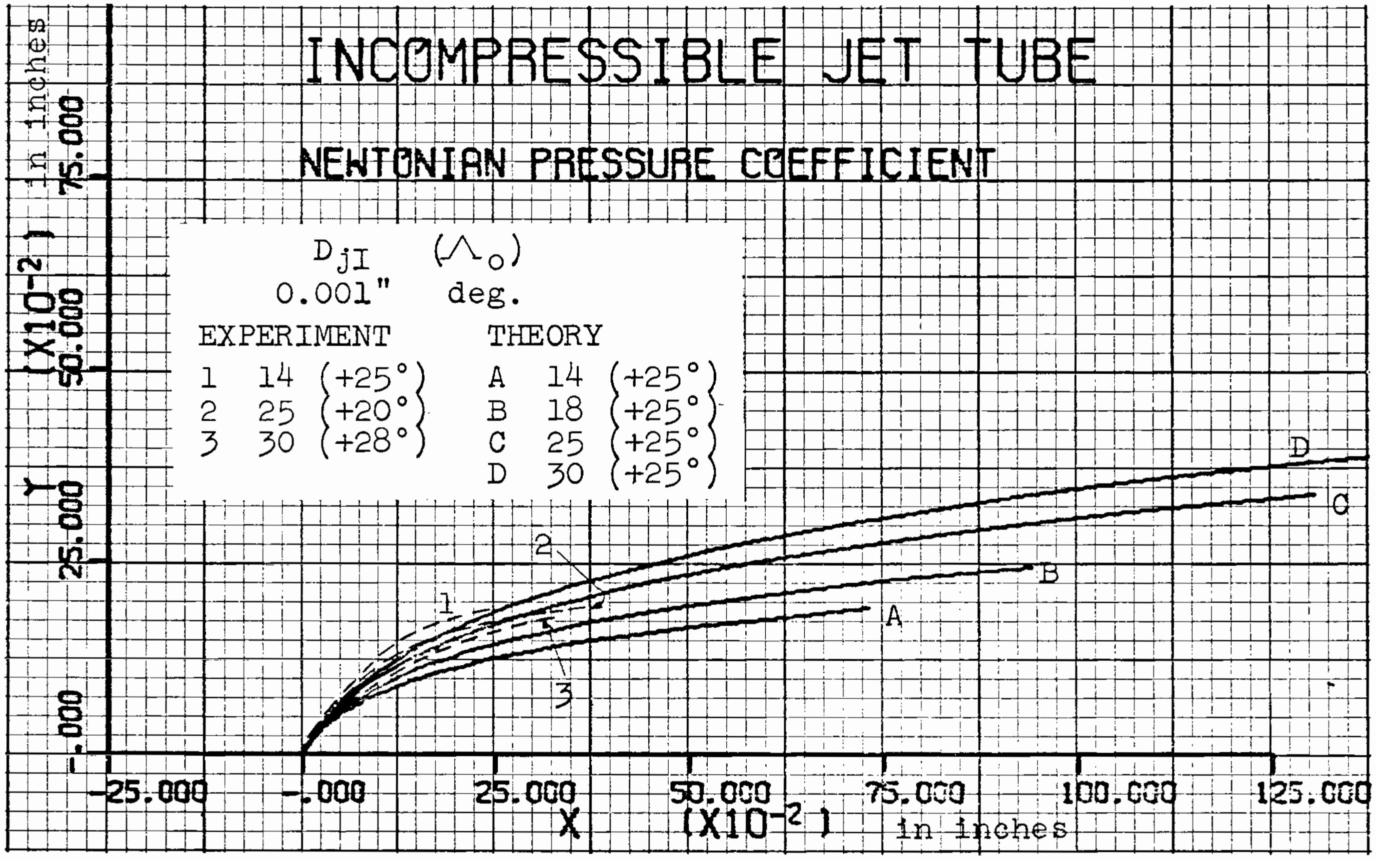

FIGURE 37a JET CENTRELINE PATH COMPARISON OF EXPERIMENT AND THEORY FOR A RANGE OF D_{jI}'S (P_{tj} = 265 psia)

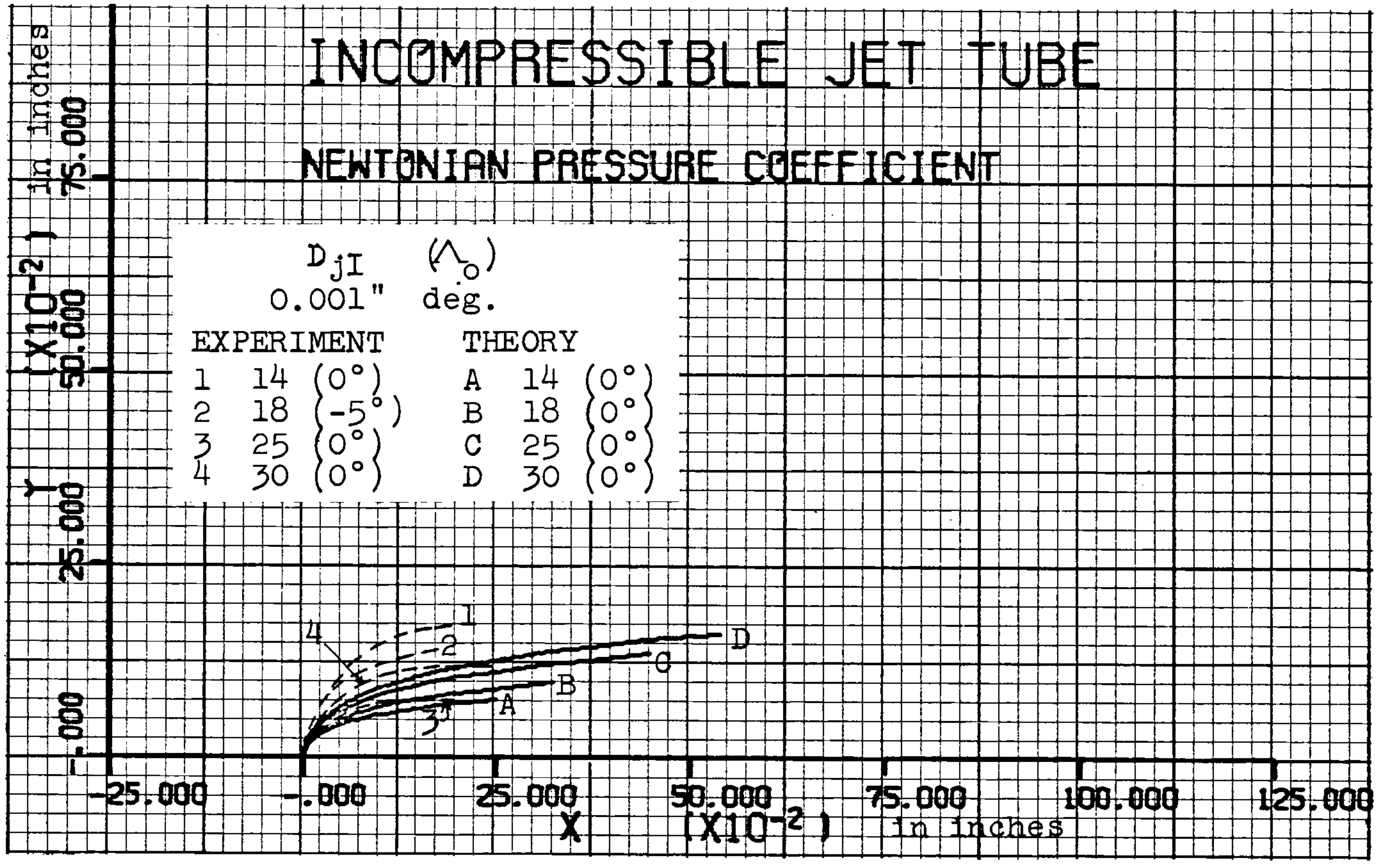

FIGURE 37b JET CENTRELINE PATH COMPARISON OF EXPERIMENT AND THEORY FOR A RANGE OF D_{jI}'S (P_{tj} = 90 psia)

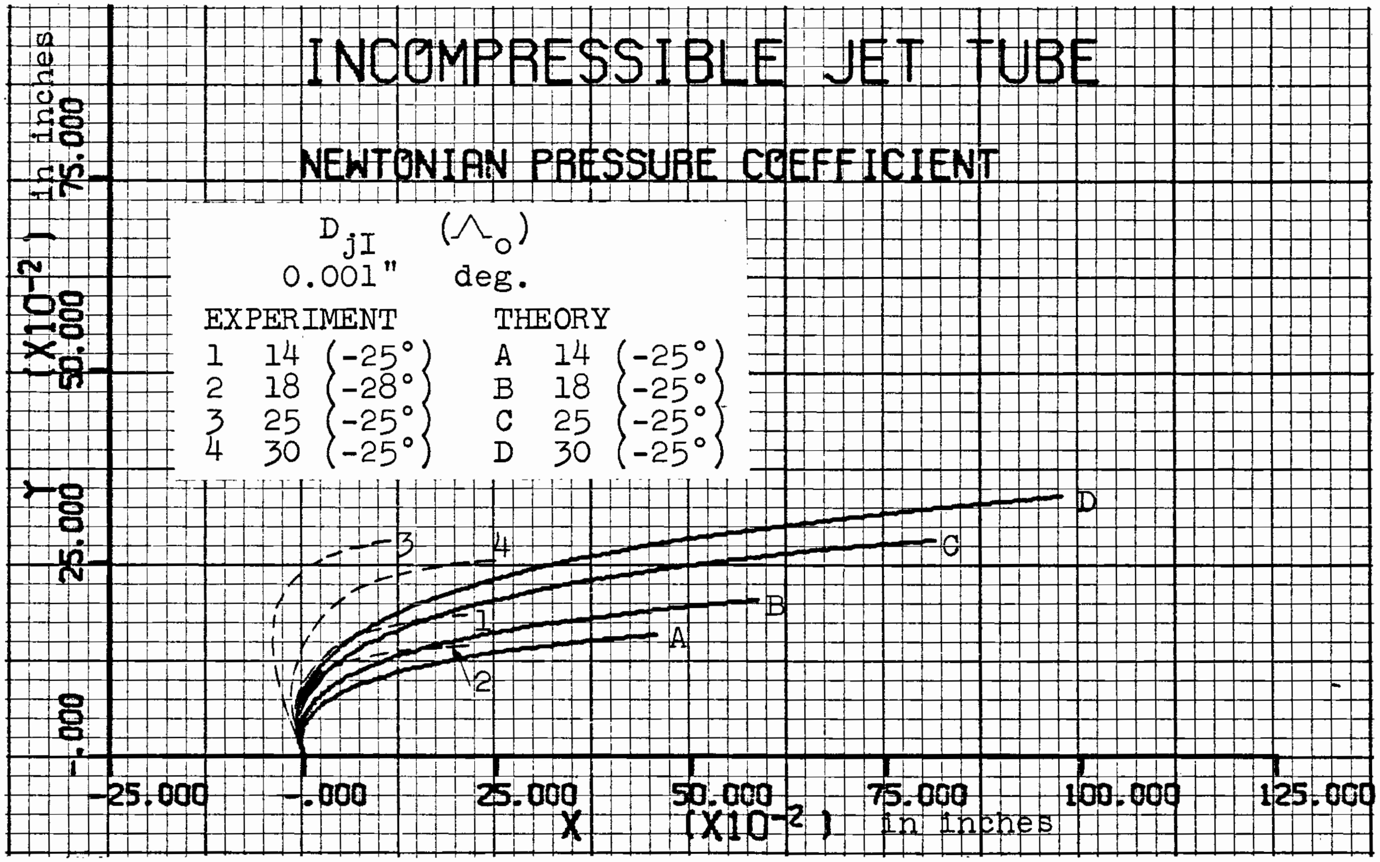

FIGURE 37c JET CENTRELINE PATH COMPARISON OF EXPERIMENT AND THEORY FOR A RANGE OF D_{jI}'S (P_{tj} = 165 psia)